Review Article

Multifunctional 3D-printed bioceramic scaffolds: Recent strategies for osteosarcoma treatment

Journal of Tissue Engineering
Volume 14: 1–40

DOI: 10.1177/20417314231170371
journals.sagepub.com/home/tej
Sage

Xingran Liu[1,2*], Yihao Liu[1,2*], Lei Qiang[3*], Ya Ren[3], Yixuan Lin[1], Han Li[2], Qiuhan Chen[2], Shuxin Gao[2], Xue Yang[3], Changru Zhang[1,2], Minjie Fan[4], Pengfei Zheng[4], Shuai Li[5] and Jinwu Wang[1,2,3,6,7]

Abstract

Osteosarcoma is the most prevalent bone malignant tumor in children and teenagers. The bone defect, recurrence, and metastasis after surgery severely affect the life quality of patients. Clinically, bone grafts are implanted. Primary bioceramic scaffolds show a monomodal osteogenesis function. With the advances in three-dimensional printing technology and materials science, while maintaining the osteogenesis ability, scaffolds become more patient-specific and obtain additional anti-tumor ability with functional agents being loaded. Anti-tumor therapies include photothermal, magnetothermal, old and novel chemo-, gas, and photodynamic therapy. These strategies kill tumors through novel mechanisms to treat refractory osteosarcoma due to drug resistance, and some have shown the potential to reverse drug resistance and inhibit metastasis. Therefore, multifunctional three-dimensional printed bioceramic scaffolds hold excellent promise for osteosarcoma treatments. To better understand, we review the background of osteosarcoma, primary 3D-printed bioceramic scaffolds, and different therapies and have a prospect for the future.

Keywords

Osteosarcoma treatment, anti-tumor, osteogenesis, functional agents, multifunctional 3D-printed bioceramic scaffolds

Date received: 11 January 2023; accepted: 31 March 2023

[1]Shanghai Key Laboratory of Orthopedic Implant, Department of Orthopedic Surgery, Shanghai Ninth People's Hospital, Shanghai Jiao Tong University School of Medicine, Shanghai, China
[2]Shanghai Jiao Tong University School of Medicine, Shanghai, China
[3]Southwest Jiaotong University, Chengdu, China
[4]Department of Orthopaedic Surgery, Children's Hospital of Nanjing Medical University, Nanjing, China
[5]Department of Orthopedics, The First Affiliated Hospital, Zhejiang University School of Medicine, Hangzhou, China
[6]Shanghai Jiao Tong University, Shanghai, China
[7]Weifang Medical University School of Rehabilitation Medicine, Weifang, Shandong Province, China

*These authors contributed equally to this work.

Corresponding authors:
Jinwu Wang, Shanghai Key Laboratory of Orthopedic Implant, Department of Orthopedic Surgery, Shanghai Ninth People's Hospital, Shanghai Jiao Tong University School of Medicine, No. 639 Zhizaoju Road, Shanghai 200011, China.
Email: wangjw-team@shsmu.edu.cn

Shuai Li, Department of Orthopedics, The First Affiliated Hospital, Zhejiang University School of Medicine, 79 Qingchun Road, Hangzhou, Zhejiang 310003, China.
Email: allenle1991@sina.com

Pengfei Zheng, Department of Orthopaedic Surgery, Children's Hospital of Nanjing Medical University, No. 72 Guangzhou Road, Nanjing, Jiangsu 210008, China.
Email: zhengpengfei@njmu.edu.cn

Introduction

Osteosarcoma (OS) is a primary bone malignant tumor most common in children and teenagers. The annual incidence of OS is 4.7 cases per million in children (0–19 years), which accounts for 8.9% of pediatric cancer-related deaths.[1] Nowadays, limb-salvage surgery, along with neoadjuvant chemotherapy, is the main osteosarcoma clinical treatment. However, due to drug resistance, this treatment is sometimes not efficient. After surgery, there are still a small number of residual osteosarcoma cells (OCs) around the bone defect that can proliferate within a few days, resulting in bone tumor recurrence or even metastasis.[2] Furthermore, surgery may cause large-scale bone defects, which can impair tissue or organ function and reduce the life quality of patients.[3]

The traditional method for post-surgery bone defects is to implant bone substitute materials, which can induce bone regeneration.[4] However, many problems have arisen in clinical applications, such as bleeding, tissue necrosis, tumor recurrence, and infection.[5] Researchers have been attempting to construct an ideal bioactive scaffold with adequate mechanical strength and the ability to kill OCs, induce angiogenesis, and promote bone regeneration.[6]

Three-dimensional (3D) bioceramic scaffolds with good biocompatibility, biodegradability, and bioactivity are increasingly popular as ideal multifunctional implants for osteosarcoma treatment. Due to advances in 3D printing technology, 3D-printed bioceramic scaffolds are becoming more patient-specific with pre-customized and personalized architecture.[7,8] In addition to filling post-surgery defects as traditional bone substitutes with bone-like mechanical strength, the scaffold exhibit enhanced physical, chemical, and biological capabilities for bone regeneration. 3D-printed bioceramic scaffolds offer a 3D microenvironment and hierarchical structure for bone cell attachment, proliferation, and differentiation. The scaffolds also offer inner channels for transporting nutrients and waste. Commonly used primary 3D bioceramic scaffolds for osteosarcoma treatment include hydroxyapatite (HA), akermanite ($Ca_2MgSi_2O_7$, AKT), β-tricalcium phosphate (β-TCP), and bioactive glass (BAG).[9–12] Furthermore, numerous studies have shown that after being modified with several anti-tumor functional agents, bioceramic scaffolds like HA,[13] BG,[14] β-TCP,[15] and AKT[10] still show excellent osteogenesis ability. Nanosheets,[16] nanoparticles,[17] nano-coatings,[18] and even engineered microbes[19] can be added to these primary scaffolds to construct scaffolds with the primary osteogenic ability and new functions. These new functions include photothermal property, magnetothermal property, radical oxygen species generation, or anti-tumor gas generation for tumor therapy. Some agents can also promote the adhesion, growth, and differentiation of bone mesenchymal stem cells (BMSCs) and vascularization.[20,21] Thus, 3D-printed bioceramic scaffolds with high anti-tumor efficiency, less tumor recurrence, and better bone regeneration meet the dilemma of clinical treatment of osteosarcoma.

For the treatment of osteosarcoma, anti-tumor agents cause OCs death, while bioactive agents and 3D bioceramic scaffolds could induce osteogenesis, as shown in Figure 1. In this review, we first briefly introduce osteosarcoma and its microenvironment and describe how its characteristics, such as heat sensitivity and acidity, relate to the following therapies. After that, we introduce the primary 3D-printed bioceramic scaffolds. We first discuss the importance of 3D printing for obtaining patient-specific scaffolds. After that, we discuss the chemical, biological, and physical properties of HA, AKT, TCP, and BG separately for a deeper understanding of the osteogenic ability of bioceramic scaffolds. To illustrate how each multifunctional scaffold addresses the two main problems after osteosarcoma surgery: residual OCs and bone defects, we discuss in detail the composition, pore and mechanical properties, production and loading methods, and the anti-tumor and osteogenic ability of various multifunctional scaffolds.

We introduce in the order of photothermal therapy (PTT), magnetothermal therapy (MTT), chemotherapy, photodynamic therapy (PDT), and gas therapy. For PPT, we introduce its three mechanisms of killing OCs and discuss each scaffold in the order of organic materials, carbon-based materials, transition metal-based materials, and plasmonic materials. Next, we introduce another hyperthermia therapy MTT, in the order of Fe alloy, Fe_3O_4, and other Fe-based materials. After that, we discuss chemotherapy. We focus on the loading and the controlled and TME-responsive release for conventional and novel chemotherapy drugs. In addition, we discuss the potential of traditional drugs to be combined with other therapies, such as PPT, to achieve better anti-tumor effects. We also discuss the turn-over and tailor-made effect of novel drugs. For PDT, we discuss fabricating and loading strategies for penetration limitation and oxygen deficiency, respectively. Finally, we discuss the potential of gas therapies to kill OCs. Finally, we discuss the potential of combining different therapies to obtain "all-in-one" scaffolds for better OS treatment. We highlight the importance of similarity principles of bioceramics for bone and soft tissue engineering. Considering other clinical dilemmas in addition to bone defect and residual OCs, we then discuss in detail how various strategies address drug resistance, metastasis, and the low diagnosis rate of conventional imaging. Finally, we prospect the future of 3D-printed multifunctional bioceramic scaffolds for osteosarcoma treatment, and we believe that clinical translation of OS is within reach if existing problems are noticed and addressed.

Osteosarcoma and its tumor microenvironment

Osteosarcoma is a common primary bone malignancy affecting more men than women.[22,23] There are two incidence peaks: in adolescents and adults older than 60 years of age.[24] The former is due to hormonal changes in puberty.[25]

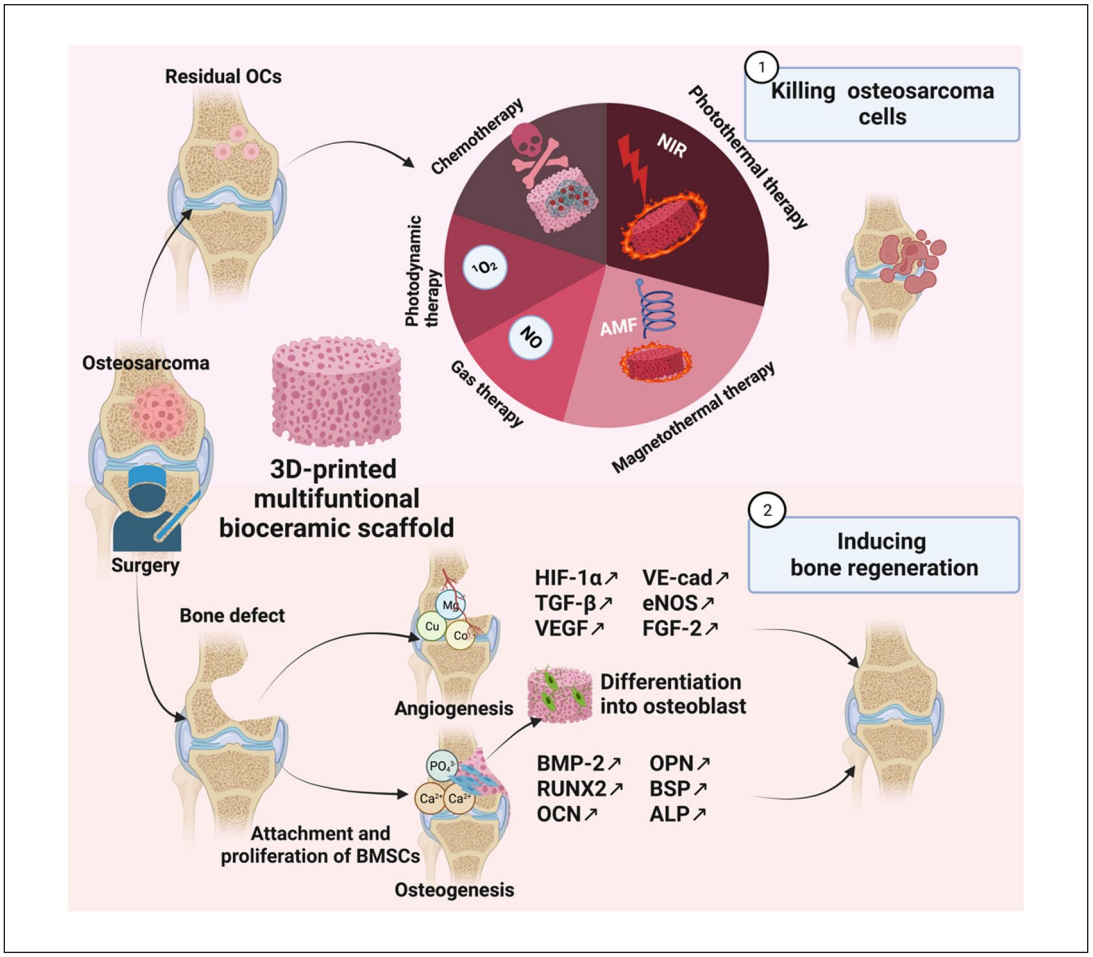

Figure 1. The process of using multifunctional 3D-printed bioceramic scaffolds to kill osteosarcoma cells and promote bone regeneration. Created with BioRender.com.

The latter is usually secondary to other diseases, transformed from benign bone diseases, or as a later effect of radiation.[26] Osteosarcoma can occur in any bone, and the distal femur (43%), proximal tibia (23%), and proximal humerus (10%) are the three locations where it occurs most frequently.[27] The most typical symptom is pain, especially with activity, and may lead to claudication.[28] Pathological fractures are not very common, except for the telangiectatic type. Additionally, systemic symptoms are rare.[29]

Osteosarcoma often presents as a spindle cell, and its histological hallmark is the production of malignant osteoid. It is frequently assumed to arise from the malignant transformation of mesenchymal lineage cells at an indeterminate differentiation stage into osteoblasts.[30] Chondrocytes, fibroblasts, osteoblasts, and telangiectatic tumors are the four subtypes of osteosarcoma that can be distinguished based on the primary matrix produced.[31] Osteosarcomas can also be classified into three groups, low, intermediate, and high grade, as relative indicators of the danger of developing metastases.[32] Low-grade OS is typically inert and can only be removed surgically. High-grade OS requires additional adjuvant chemotherapy for treatment because they have a high probability of metastasizing to the lungs, lymph nodes, and other bones. Pulmonary metastasis is a prognosis-defining complication that reduces 5-year event-free survival.[27,33]

Osteoblasts, osteoclasts, and osteoclasts form bone tissue. Bone homeostasis and the replacement of the old bone matrix depend on the proper interaction of these cells with one another and their microenvironment.[34] When genetic mutations (TP53, RB1, RECQL4) occur in BMSCs or BMSC-derived pro-osteoblasts, these mutations accumulate to a subpopulation of cancer stem cells (CSCs) that may lead to incompletely differentiated osteoblasts or osteoclasts.[35,36] Through interactions with the tumor microenvironment (TME), CSCs can self-renew and maintain osteosarcoma progression.[36] The proliferation of OCs intensifies osteoclast activity and bone resorption and disrupts the balance between osteoblasts and osteoclasts. Moreover, OCs secrete RANKL, interleukin (IL)-6, IL-11, and tumor necrosis factor-α in soluble factors and extracellular vesicles. They increase the release of factors

entrapped in the bone matrix, such as insulin-like growth factor (IGF) and tumor growth factor (TGF), which aid in the survival and growth of OCs.[37]

Interestingly, tumor tissues in the specific TME are more sensitive to thermal stimulation than normal tissues because they have a lower capacity to dissipate heat. Consequently, rather than harming healthy tissues, photothermal and magnetothermal therapy can specifically kill OCs.[38] In addition, the weak acidity,[39] H_2O_2 overproduction,[40] low catalase activity,[41] and hypoxia[42] of the TME not only provide a favorable environment for proliferation and metastasis of OCs[43,44] but also offer a potential for the selective treatment of osteosarcoma. For example, for CDT, iron-based nanomaterials dissolve ferrous ions in the mildly acidic TME environment and start the Fenton reaction, which overproduces hydrogen peroxide (H_2O_2) and generates hydroxyl radical (•OH) to trigger apoptosis of OCs.[45] In addition, TME-responsive drug delivery nanocarriers have been created. The local pH of tumor tissue and intracellular endosome/lysosome is 1–2.5, lower than that of blood and healthy tissues (pH = 7.4).[46] Therefore, the pH-sensitive scaffold polydopamine (PDA)-modified curcumin (CM)-loaded silk fibroin (SF) composite (SF/CM-PDA) can achieve controlled release of curcumin (CM) with excellent CM permeability at tumor sites.[47,48] Besides, doxorubicin (DOX) in the fluorescent mesoporous bioglass nanoparticles (fBGn) can also release in a PH-dependent way.[49]

TME also imposes limitations on some treatments. Overproliferation of OCs and inadequate blood supply leads to severe hypoxia (oxygen pressure <5 mm Hg) in TME.[50] Hypoxic TME is a significant barrier for PDT. Additionally, PDT further increases tumor hypoxia, potentially leading to tumor invasion and metastasis.[51] So far, reactive oxygen supply materials and oxygen carriers have been developed to overcome the restriction of PDT caused by hypoxic TME.[52] In addition, drug resistance events such as elevated expression of drug efflux systems, such as P-glycoprotein (P-gp), increased DNA repair activity, altered epigenetic factors, and regulation of anti-apoptotic genes have been linked to CSC niches. Besides, traditional chemotherapy can induce the selection of stem cells and activate the proliferation signaling pathway like WNT/β-catenin.[53] Therefore, targeted therapies have been developed to address this problem, including blocking signaling pathways such as Hedgehog, WNT, IGF, and TGF-β.[54–56]

Primary 3D-printed bioceramic scaffolds

The scaffold in bone tissue engineering creates a 3D environment for cell adhesion and proliferation. The optimal scaffold for bone regeneration should mimic healthy bone tissue's structure and biological function in terms of chemical compositions, hierarchical structures, and mechanical properties. 3D bioceramic scaffold is increasingly interested in bone tissue regeneration owing to its bone-like composition, biocompatibility, osteoconductivity, osteoinductivity, and bioactivity.[57] However, traditional fabrication techniques, like freeze-drying, emulsification, and phase separation/inversion, cannot manage the pore size, porosity, or interconnectivity or specifically adapt to the geometry of the bone defect.[58,59]

As shown in Figure 2, scaffolds with controlled chemical composition, pore shape, porosity, and interconnectivity are fabricated using computer-aided design (CAD) and computer-aided manufacturing (CAM) 3D printing technology.[60] 3D-printed bioceramic scaffolds obtain extremely complex growth-orientated structures that promote cell migration and proliferation for better bone regeneration. Additionally, it offers a precise model of the patient-specific bone defects, allowing for the patient-specific 3D porous scaffolds with pre-designed and personalized structures.[61] The 3D printing techniques include stereolithography (SLA), selective laser sintering (SLS), micro extrusion with/without post-sintering, fused deposition molding (FDM), and binder-based 3DP. SLA and SLS both have good accuracy with high cost, while FDM and binder-based 3DP are less costly with less accuracy. Both SLA and SLS require post-curing. SLA-fabricated scaffolds are hardened under ultraviolet (UV) laser light, while SLS uses a laser to sinter the powder granules. Like SLS, FDM demands high temperatures so that the filament can melt and be extruded from a hot nozzle.[62,63] For micro-extrusion with post-sintering, a high temperature is not necessary for the extrusion of the printable ink but for post-sintering. Sometimes, a cryogenic environment is also available for post-sintering.[11] Besides, pluronic F-127 and poly (vinyl alcohol) (PVA) are commonly used binders.[10,14,15]

Hydroxyapatite (HA) is one of the most frequently utilized 3D bioceramics, with biocompatibility, osteoinductivity, and osteoconductivity.[9] HA can induce osteogenesis by stimulating endogenous bone morphogenetic protein (BMP) expression and enhancing alkaline phosphatase (ALP) activity.[64,65] However, compared with other bioceramics, HA is brittle, has a load-bearing limitation, and has a low degradation rate.[66] To overcome these limitations, several natural or synthetic polymers can be combined with HA to create composite scaffolds, such as poly (lactide-co-glycolide) (PLGA),[67] polycaprolactone (PCL),[68] poly (l-lactic acid) (PLLA),[69] polydopamine (PDA),[38] and carboxymethyl chitosan (CMCS).[13] Besides, nano-hydroxyapatite (nHA) has become increasingly popular. Primarily, nHA up-regulates the expression of ALP, osteocalcin (OCN), bone sialoprotein (BSP), and Runt-related transcription factor-2 (RUNX-2). Among them, ALP is the marker of early-stage differentiation, and OCN is the marker of later-stage differentiation for controlling mineral growth. nHA provides crystal nuclei for calcification and

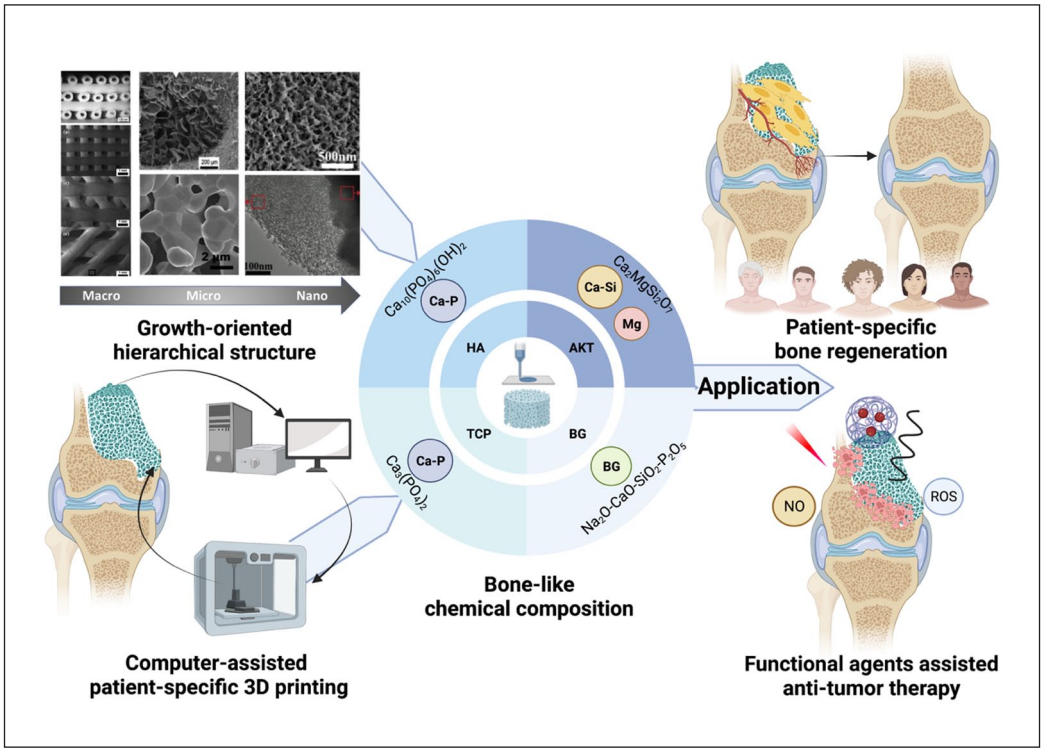

Figure 2. The growth-oriented hierarchical structure, the computer-assisted patient-specific 3D printing, and the bone-like chemical composition lead to the application of patient-specific bone regeneration. Cited with permission.[61] Copyright 2018, *Acta Biomaterialia*. Created with BioRender.com.

osteogenesis,[81] exhibiting a more vital osteoinductive ability. Moreover, due to its large specific surface area,[70] nHA is more likely to crosslink with other materials, load drugs, and facilitate cell adhesion and proliferation.[70,71] The nHA also has better plasticity, brittleness, and degradation than conventional HA.[72] The nHA surface layer can be easily obtained using ethanol as the liquid bridge by immersing. The nHA coating could effectively slow the degradation rate of 3D magnesium-doped wollastonite (CSi-Mg) scaffolds and sustain high mechanical strength (over 90 MPa) for over 3 weeks. In addition, nHA could inhibit the expression of Ki-67 and B-cell lymphoma-2 (Bcl-2) and promote the expression of Caspase-3, thus promoting OCs apoptosis. After 7 days of culture, the CSi-Mg/nHA scaffold killed approximately 50% of the OCs. In addition, the thicker the nHA surface layer, the higher the mechanical strength and the apoptosis rate of OCs.[18]

Akermanite (AKT, $Ca_2MgSi_2O_7$) is another bioceramic containing Ca, Mg, and Si, which is more controllable in terms of mechanical properties[73] and degradation rate.[74] Its first application was to synthesize pure polycrystalline AKT particles with a size of 5–40 μm by the sol-gel method. AKT showed the ability to form apatite and thus gradually began to be used as a bone tissue engineering scaffold.[75] AKT promotes the adhesion, proliferation, and differentiation of BMSCs.[76] Besides, AKT could promote angiogenesis.[77,78] AKT bioceramic scaffolds are often made of AKT powder by 3D printing technology. The superb interconnected porous structure and the large number of micropores on its surface are advantageous for the permeation and encapsulation of nanoparticles (NPs).[52] On this basis, nanosheets or nanoparticles are loaded into the scaffolds or directly doped into the powder for 3D printing to provide the scaffolds with additional functions.[10,52]

Tricalcium phosphate (TCP, $Ca_3(PO_4)_2$) has two forms: high-temperature α-phase and low-temperature β-phase, and the β-phase is used as bioceramics. β-TCP is the stable form at low temperatures and is economical to prepare.[79,80] Since the first attempt to implant β-TCP into rabbit bones to repair defects caused by surgery, β-TCP has received increasing attention.[81] The bioactivity of β-TCP is related to the containing calcium and phosphorus ions. Through partial dissolution and release, these ions could form biological apatite deposition. The biodegradability and resorption rate of β-TCP was better than HA, but the degradation rate still cannot meet the generation rate of new bone.[82] Combining with polymers such as PLGA can improve its biodegradability.[11] Besides, the β-TCP bioceramic scaffold also has better flexural strength and fracture toughness than HA. The mechanical strength (12 MPa) is still less than that of human cortical bone (90–170 MPa)[83] but is comparable to human cancelous bone (16.3 ± 7.2 MPa).[11,84] The compressive strength of

TCP scaffolds can reach about 24–38 MPa with poly (d, l-lactide) (PDLLA)[84] coating.

Bioactive glass (BG) was invented by Larry Hench, and since then, it has been known as 45S5 Bioglass®.[82] The main components of BGs are Na_2O, SiO_2, CaO, and P_2O_5,[85] and the melt-quenching and the sol-gel approach are the two main manufacturing methods. Recently, 3D printing has also been widely used, and some functional agents can be directly doped into the bio-ink to fabricate the multifunctional scaffold. BGs hold great potential in bone tissue engineering. The macroporous structure facilitates the transport of nutrients and bone formation. Besides, its component elements (Ca, P, and Si) also promote the proliferation and differentiation of BMSCs and the production of bone matrix.[86,87] Additionally, BG becomes more competitive due to its angiogenesis ability through vascular endothelial growth factor (VEGF).[88] Besides, BG is also conducive to forming the carbonation of HA and HA bioactive surface layer to achieve interface bonding with surroundings.[89] However, like HA, the inherent brittle nature is the major limitation in its potential application. Metals, such as Ti and Ag, can serve as reinforcement to overcome this limitation.[90] We have summarized the 3D printing method, binder, parameter, chemical composition, metal ions, possible improvement methods, and application of the primary 3D-printed bioceramic scaffolds, as shown in Table 1.

Anti-tumor therapy of 3D scaffolds

3D-printed bioceramic scaffolds obtain anti-tumor effects by loading various functional agents for photothermal, magnetothermal, chemo-, photodynamic, or gas therapy. Both PTT and MTT take advantage of TME. Tumor tissue is more susceptible to thermal stimulation and has poorer heat dissipation than normal tissues.[38] Through various photothermal conversion agents and Fe-based magnetothermal agents, under near-infrared (NIR) and alternating magnetic field (AMF), increased tumor microenvironment temperature induces apoptosis and necrosis of OCs.[38] Chemotherapy takes advantage of the fact that tumor cells proliferate more rapidly and have more immature cells, which makes them more sensitive to chemotherapy drugs than normal cells.[105,106] In photodynamic therapy, the photosensitizer undergoes inter-systemic crossing (ISC) to an excited triplet state (T1), forming $^3PS^*$. $^3PS^*$ is mainly dependent on oxygen to generate type II reactive oxygen species (ROS) (single linear state oxygen ($^1O_2$)) through energy transfer.[107] For the type I process, superoxide anion radicals ($O_2^{\bullet-}$) and H_2O_2 are generated through electron transfer and sequentially producing •OH. •OH is highly destructive to almost all biological molecules, allowing full use of the limited oxygen in hypoxic tumors.[108,109] ROS targets nucleic acids and proteins and causes tumor cell apoptosis and necrosis. Gas therapy like nitric oxide (NO) can damage DNA and enzymes to kill OCs.[110] Simultaneously, besides 3D-printed bioceramic scaffold, the loaded osteogenic agents or some therapeutic agents with a turnover effect (curcumin,[97] metformin,[69] and NO[101]) can further promote bone regeneration. They can up-regulate the osteogenic genes, induce the adhesion, proliferation, and differentiation of BMSCs, and promote calcification. Therefore, tumor destruction and osteogenesis can be achieved simultaneously for osteosarcoma treatment and prognosis. The following illustrates and discusses different treatment methods in detail.

Photothermal therapy

Recently, killing tumor cells using PTT has become an intense interest. The critical principle of PTT is to convert light energy to thermal energy. Typical light sources include UV, visible, and NIR light. There are concerns about using UV light-mediated therapy in clinics because UV light's short wavelength (about 400 nm) can generate significant energy that may harm normal tissues. Moreover, the widespread visible light with longer wavelengths lacks controllability and energy. NIR light, which has wavelengths between 700 and 1000 nm, is thought to have deeper tissue penetration and less photodamage and is particularly useful for light-mediated therapy.[46,111,112] The selection of NIR light is mainly based on the transparency window of the biological tissue in the NIR region,[113] so a wavelength of 808 nm NIR is usually used. In TME, tumor tissues with reduced heat dissipation capacity are more susceptible to thermal stimulation than normal tissues.[38] Heat stimuli severely and irreversibly denature proteins and damage tumor cell DNA. When tumor cells reach 41°C, the protein starts to denature; in the meantime, the cells become inactive for several hours. Thus, temperatures between 41°C and 45°C mainly lead to tumor cell death by apoptosis.[114] Between 45°C and 48°C, tumor cells can quickly necrotize, and many cells will die above 48°C.[115,116] It is worth mentioning that when the temperature is reached to induce tumor cell necrosis instead of apoptosis, the tumor can be killed more quickly, and subsequent tumor recurrence can be inhibited. After initial thermal stimulation, necrotic tumor tissue can further lead to apoptosis, vascular injury, ischemia-reperfusion injury, altered cytokine expression, Kupffer cell activation, and altered immune responses.[38] Therefore, when photothermal agents raise the tumor site temperature to more than 50°C, there is often a satisfactory tumor mortality rate.[15,117] The efficiency of PTT is mainly dependent on the use of high-quality photothermal conversion agents, such as organic materials (polydopamine (PDA),[117] DTC co-crystals,[14] carbon-based nanomaterials (CBN) (graphene oxide (GO),[118] borocarbonitride (BCN)[10], Cu and other transition metals (hemin,[12] $CuFeSe_2$,[99] single-atomic iron catalysts (FeSAC),[102] MXene[104])), and plasmonic nanomaterials (LaB_6[98]). Table 2 illustrates the specific photothermal agents added to the 3D-printed bioceramic scaffold.

Table 1. Commonly used primary 3D-printed bioceramic scaffold.

Bioceramic scaffolds	Method	Binder	Printing parameter	Chemical composition	Metal ions	Pore	Mechanical property	Improvement	Application
Hydroxyapatite (HA)	3DP[38]; SLS[69]	$CaCl_2$ & genepin[38]	Pressure: 0.12–0.30 MPa; Speed: 12–18 mm/s[38]; Laser power: 2.1 W; Speed: 120 mm/min; Spot diameter: 0.3 mm; Scanning line interval: 0.8 mm[69]	$Ca_{10}(PO_4)_6(OH)_2$		Pore size (100–300 μm[69]) & Porosity (81.46 ± 4.65% for PLLA/nHA/MET, and 51.56 ± 4.48% for PLLA/nHA)[69]	Compressive strength (5.34 MPa[38]) & Young's modulus (16.86 MPa[38]); Young's modulus (33.42 ± 0.81 MPa for PLLA/nHA, and 10.84 ± 0.73 MPa for PLLA/nHA/MET[69])	(1) Slow degradation rate (combine with polymers like PLLA and CS)	HA ± PDA ± CMCS[38]
								(2) Poor mechanical strength and fracture toughness (in the form of nHA, crosslink with genepin, and combined with polymers like PLLA)	nHA ± PLLA ± MET[69]
Akemanite(AKT)	Micro-extrusion with post-sintering[10,52,91–93]	F127[10,91,92]	Needle: 22G[10]/20G[91]; Nozzle outer diameter: 450 mm[52]; Nozzle inner diameter: 0.60 mm[93]; Pressure: 3.0 bar[93]	$Ca_2MgSi_2O_7$	Mg: angiogenesis and osteogenesis	300 μm[10]	Compressive strength (5.91–14.48 MPa, with the lower sintering temperature after adding Fe)[92]	(1) To improve the rheological and mechanical qualities of ink, 3–5 wt% sodium alginate was added	AKT + BCN[10]
		PVA[52,93]				450 μm[92]		(2) The mechanical strength increases with lower sintering temperature by adding Fe[92]	AKT + MoS_2[91] AKT + Fe[92] AKT + Fe_3O_4 + CaO_2[52] AKT + Fe_3S_4[93]
β-Tricalcium phosphate (β-TCP)	Micro-extrusion with post-sintering[15,94–97]	F127[84,94,98]	Needle: 21G[15]/22G[94,98]; Speed: 5,[84,94,98] 6,[95] and 1 mm/s[96]; Nozzle inner diameter: 0.4 mm,[11]	$Ca_3(PO_4)_2$		500 μm[15]	Compressive strength (24.04–38.76 MPa, dependent on PDLLA coating time)[98]	(1) Slow degradation rate (combine with polymers like PLGA)	β-TCP + GO[15]
	Micro extrusion in a cryogenic environment[11]	PVA[15,95]	0.52 mm[95]; Pressure: 1.8–3.0 bar,[95] 0.5–1.5 bar[84]; 550–600 kPa[96]; Stepping distance: 1.11 mm[95]			400 μm[97]	Compressive strength (12.2–14.6 MPa comparable to human cancelous bone (16.3 ± 7.2 MPa) & Elastic modulus (4–4.5 MPa)[11]	(2) Enhanced osteogenesis and angiogenesis ability (add Cu element)	β-TCP + Cu-TCPP[94]
						300–500 μm[95]	Compressive strength (20 MPa for hallow TCP and 24 MPa for gelatin/TCP core/shell)[96]	(3) Low mechanical strength(PDLLA coating, applying gelatin core in the form of core/shell)[84,96,98]	β-TCP + DOX + P24 + BP + PLGA[11] β-TCP + LaB_6 NP + PDLLA[98] β-TCP + Fe_3O_4 + GO[95] TCP + PDLLA + TiN + DOX[84] DOX-gelatin + $SrCuSi_4O_{10}$-β-TCP[96] β-TCP + Liposome-encapsulated curcumin[97]

(continued)

Table 1. (continued)

Bioceramic scaffolds	Method	Binder	Printing parameter	Chemical composition	Metal ions	Pore	Mechanical property	Improvement	Application
Bioglass (BG)	Micro-extrusion with post-sintering[12,14,16,99–101]	F127[12,99,100]	Needle: 22G[99,100]; Nozzle inner diameter: 0.4 mm[14,16]; Pressure: 2.8–4.4[14,16,102] and 0.5–2.0 bar[12]; Speed: 8–18[14,16,102] and 5 mm/s[12]; Layer thickness: 0.32 mm[14,16]	25CaO-70SiO_2-2.5P_2O_5[99]	Na	350 μm[14,16]		(1) Enhanced osteogenesis and angiogenesis ability (add metal ions like Cu, Fe, Mn, and Co)	BG + DTC[14]
		Polyvinyl alcohol solution[101]		SiO_2 (45%)-Na_2O (24.5%)-CaO (24.5%)-P_2O_5(6%) [103]				(2) Poor mechanical strength (add metal like Ag and Ti)	BG + DOX + Hemin[12] BG + $CuFeSe_2$[99] BG + Cu, Fe, Mn, or Co[100] BG + Ti_3C_2 Mxene[16] BG + Nb_2C Mxene[104] BG + Nb_2C Mxene-SNO[101] BG + FeSAC[102]

Table 2. Specific photothermal agents added to the 3D-printed bioceramic scaffold.

Materials	Photothermal agents	Effect	Production methods	Coating methods	Pore size and porosity	Mechanical strength	Ref.
Organic materials							
$Ca_7Si_2P_2O_{16}$ BC + PDA	PDA (organic materials)	Photothermal therapy (80%–99% mortality rate, over 50°C, irradiated with an 808 nm laser (~0.38 W/cm^2) for 10 min) & Bone regeneration (the new bone area around 15% after implantation for 8 weeks)	3D Printing (Extrusion with post-sintering)	Self-assembly by soaking			Ma et al.[117]
HA/PDA/CMCS	PDA	Photothermal therapy (OCs necrosis rate reached 73.3%, maintained at 58°C, irradiated with an 808 nm laser (~1 W/cm^2) for 10 min) Bone regeneration (up-regulation of ALP, COL-1, and COL-1)	3D Printing (3DP)	Stirring		Compressive strength (5.34 MPa) & Young's modulus (16.86 MPa)	Yao et al.[38]
DTC + BG	DTC (Organic co-crystals)	Photothermal therapy (mortality rate around 80%, maintained at 55°C, irradiated with an 808 nm laser (~1.5 W/cm^2) for 10 min) & Bone regeneration (up-regulation of ALP, OCN, BMP-2 and RUNX-2, 43.5 ± 2.7% BV/TV and 4.8 g·m^3 BMD after implantation for 8 weeks)	3D Printing (Extrusion with post-sintering)	Self-assembly & In situ growth through evaporation	350 μm		Xiang et al.[14]
Carbon-based nanomaterials							
β-TCP + GO	Graphene oxide (carbon-based nanosystems)	Photothermal therapy (mortality rate around 92.6% in vitro and 83.28% in vivo, the center area over 50°C and the tumor edge over 45°C, irradiated with an 808 nm laser (~0.36 W/cm^2) for 10 min) & Bone regeneration (up-regulation of OCN, RUNX-2, and BSP, the new bone area around 33% after implantation for 8 weeks)	3D Printing (Extrusion with post-sintering)	Soaking	500 μm		Ma et al.[15]
AKT + BCN	2D Borocarbonitrides (BCN) nanosheets (carbon-based nanosystems)	Photothermal therapy (mortality rate of OCs over 89%, over 50°C, irradiated with an 808 nm laser (0.30 W/cm^2) for 10 min) & Bone regeneration (up-regulation of ALP, OCN, OPN, BMP-2, RUNX-2, BSP, and COL1, activation of BMP/SMAD1/5 pathway, 58.2% BV/TV after implantation for 8 weeks)	3D Printing (Extrusion with post-sintering)	Soaking	300 μm		Zhao et al.[10]
Cu and other transition metals							
Metal-organic frameworks							
Cu-TCPP + TCP	Cu-TCPP (porphyrin metal-organic frameworks)	Photothermal therapy (mortality rate of OCs over 90%, maintained at 55°C, irradiated with NIR laser (1.0 W/cm^2) for 10 min) & Bone regeneration (up-regulation of ALP, OCN, BMP-2, and RUNX-2, new bone area around 40% after implantation for 8 weeks) & Angiogenesis (up-regulation of VEGF, VE-cad, eNOS, and KDR)	3D Printing (Extrusion with post-sintering)	In situ growth through solvothermal			Dang et al.[94]
Hemin + DOX + BG	Hemin	Photothermal therapy & Chemotherapy (mortality rate around 85%, maintained at 48°C, irradiated with an 808 nm laser (0.70 W/cm^2) for 10 min)	3D Printing (Extrusion with post-sintering)	Immersing			Dang et al.[12]
Transition metal chalcogenides							
$CuFeSe_2$ nanocrystals + BG	$CuFeSe_2$ nanocrystals (I-III-VI$_2$ ternary chalcogenides & semiconductor)	Photothermal therapy (mortality rate of OCs over 74% in vitro and 96% in vivo, over 48°C, irradiated with 808 nm laser (0.55 W/cm^2) for 10 min) & Bone regeneration (up-regulation of OCN and OPN, 23.2% BV/TV and 8.22% new bone area after implantation for 8 weeks)	3D Printing (Extrusion with post-sintering)	In situ growth through solvothermal			Dang et al.[99]
AKT + MoS_2	MoS_2 nanosheets (chalcogenides)	Photothermal therapy (mortality rate of OCs over 95% in vitro, 89% in vivo, over 50°C, irradiated with an 808 nm laser (0.60 W/cm^2) for 10 min) & Bone regeneration(up-regulation of ALP, OCN, OPN, and RUNX-2, around 32% BV/TV after implantation for 8 weeks)	3D Printing (Extrusion with post-sintering)	In situ growth through hydrothermal			Wang et al.[91]

(continued)

Table 2. (continued)

Materials	Photothermal agents	Effect	Production methods	Coating methods	Pore size and porosity	Mechanical strength	Ref.
Transition metal in the non-compound form							
Cu, Fe, Mn, or Co + BG	Cu, Fe, Mn, or Co (transition metal)	Photothermal therapy (tumor tissue necrosis rate and temperature: Cu (94.9%, 53.4°C) > Fe (90%, 51.3°C) > Mn (72%, 46.7°C) > Co (low, 43.3°C), irradiated with an 808 nm laser (0.75 W/cm^2) for 15 min) & Bone regeneration (Fe & Mn: up-regulation of ALP, OCN, OPN, BMP-2, and BSP) & Angiogenesis (Co: up-regulation of VEGF)	3D Printing (Extrusion with post-sintering)	Sol-gel method			Liu et al.[100]
Fe (70%) + $CaSiO_3$ (30%)	Fe	Photothermal therapy (tumor site reached over 50°C, irradiated with an 808 nm laser (0.80 W/cm^2) within 10 min) + Chemodynamic therapy (Fenton reaction catalyzed by released Fe ions) (NIR irradiation for 15 min, the mortality rate of OCs reached 91.4%, almost all OCs nuclei dissolved after treatment for 15 days) & Bone regeneration (up-regulation of OCN, BMP-2, RUNX-2, and COL1, 16% BV/TV and 17% new bone area after implantation for 8 weeks)	3D Printing (Extrusion with post-sintering)	Ball milling		Compressive strength (from 14.9 to 126 MPa by mixing with Fe)	Ma et al.[119]
FeSAC + BG	Single-atom iron catalysts (FeSAC)	Photothermal therapy mortality rate 89.27% and 95.34%for $FeSAC_{500}$-BG(500 μg/mL) and $FeSAC_{1000}$-BG, 53°C, irradiated with an 808 nm laser (1.50 W/cm^2) for 5 min) & Bone regeneration (up-regulation of COL1, BMP-2, OCN and RUNX-2, 94.3% recovery percentage, around 38% BV/TV and 4 g·m^3 BMD after implantation for 16 weeks)	3D Printing (Extrusion with post-sintering)	Impregnation (soaking and evaporation using ethanol)			Wang et al.[102]
Mxene							
2D Ti_3C_2-MXenes + BG	2D Ti_3C_2 (MXenes)	Photothermal therapy (mortality rate of OCs 75%, 63°C, irradiated with an 808 nm laser (1.0 W/cm^2) for 10 min) & Bone regeneration (up-regulation of RUNX-2, COL-1, OPN, and OCN, around 50% BV/TV and 60 g·m^3 after implantation for 8 weeks)	3D Printing (Extrusion with post-sintering)	Soaking	350 μm		Pan et al.[16]
2D-Nb_2C-MXene-NSs + BG	2D-Nb_2C (MXene)	Photothermal therapy (mortality rate of OCs 62%, 56°C, irradiated with a 1064 nm laser (1.0 W/cm^2) for 10 min) & Bone regeneration (up-regulation of RUNX-2, COL-1, OPN, and OCN, around 45% BV/TV and 65 g·m^3 after implantation for 24 weeks) & Angiogenesis (up-regulation of VEGF-B and FGF-2, around 38% newborn vessel area after implantation for 3 weeks)	3D Printing (Extrusion with post-sintering)	Soaking			Yin et al.[104]
Plasmonic nanomaterials							
β-TCP + LaB_6 NP + PDLLA	LaB_6 micro-nano particles (plasmonic nanomaterials)	Photothermal therapy (mortality rate of OCs 76%, maintained at 53°C, irradiated with an 808 nm laser (0.70 W/cm^2) for 10 min) & Bone regeneration (up-regulation of RUNX-2, COL-1, and BMP-2, the new bone area 36% after implantation for 8 weeks)	3D Printing (Extrusion with post-sintering)	Soaking		Compressive strength (24.04–38.76 MPa, dependent on coating time)	Dang et al.[98]
Other 2D nanomaterials							
DOX/P24/BP/TCP/PLGA (BDPTP scaffold)	2D BP nanosheets (semiconductor)	Photothermal therapy (tumor volume decreased from 200 to 0 mm^3 on day 4, 60°C, after 808 nm irradiation (0.5–2.0 W/cm^2) for 10 min) & Bone regeneration (up-regulation of RUNX-2, COL-1, ALP, and OCN, 38 ± 5% BV/TV and 38.5 ± 5 g·m^3 BMD after implantation for 3 months)	3D Printing (Extrusion in a cryogenic environment)	Water-in-oil composite emulsion bio-ink preparation		Compressive strength (4–4.5 MPa) & Elastic modulus (12.2–14.6 MPa) comparable to human cancelous bone	Wang et al.[11]

Mechanism of photothermal conversion. The photothermal conversion mechanisms of these materials are different and related to their innate bandgap or electronic structure.[120] Generally, they can be divided into the conjugation or hyperconjugation effect, electron-hole generation and relaxation, and the localized surface plasmon resonance (LSPR) effect.

Numerous carbon nanomaterials and polymers with conjugated structures show photothermal effects through conjugation or hyperconjugation, such as graphene[118] and polydopamine.[121] Conjugation effects caused by the overlap of adjacent π electrons or the interaction between π bonds with *p* orbital electrons redistribute the electron density. Interactions between electrons of σ bonds and adjacent vacant or partially filled *p* orbitals lead to hyperconjugation effects.[122] Both conjugation and hyperconjugation effects allow for substantial absorption in the near-infrared region and speed up electron mobility, where electrons in orbitals are excited and jump to π* orbitals, releasing heat when they return to the ground state.[123] Some co-crystals also have photothermal properties. The excited electrons are released from the lowest unoccupied molecular orbital (LUMO) to the highest occupied molecular orbital (HOMO) by electron-phonon coupling. The temperature rises as a result of this process.[124]

Electron-hole pairs are generated and relaxed in various narrow-bandgap semiconductors, such as $CuFeS_2$[124] and MoS_2.[91] When transition metal ions absorb incoming light with an energy higher than the material's bandgap, electrons in the valence band are excited and subsequently transit to the conduction band, and electron-hole pairs are formed in the valence band. An electron-hole pair releases phonons when it relaxes to the band edge, which are then converted into heat by non-radiative decay.[125]

Metal nanomaterials with high free electron mobility, such as Au, Ag, Cu, Al, and Fe nanoparticles, frequently exhibit a unique LSPR effect.[119,126] MXene[16,79] and LaB_6[98] also show the LSPR effect. The LSPR effect is defined as resonant photon-induced charge-coherent oscillations at the metal-dielectric interface if the photon frequency coincides with the natural frequency of electrons on the metal surface of the nanomaterials.[127] There are two competing pathways for surface plasmon decay: a radiative decay process that leads to light scattering by re-emitting photons and a non-radiative decay process.

Organic materials

Natural organic materials. Polydopamine is a synthetic polymer with satisfactory biodegradability and biocompatibility that mimics melanin.[128] Its absorption spectra can be extended to the NIR region, and it has a high photothermal conversion efficiency of 40%, which endows polydopamine with the anti-tumor function.[129] As a biomimetic material, polydopamine is simple to prepare and readily adsorbed on solid material's surface to form a film. It can further introduce other functional groups by reacting with reagents containing nucleophilic groups.[130] Furthermore, polydopamine can effectively increase the hydrophilicity and roughness of the surface of materials. Its chemical functional groups (NH_2^- and OH^-) can induce specific cellular responses to promote the attachment and proliferation of BMSCs. Besides, the nucleation and mineralization of apatite on the nanostructured surface can be improved owing to catechol groups in polydopamine.[117]

Ma et al.[117] soaked 3D-printed bioceramic scaffolds in Tris-dopamine solution to prepare the surface Ca-P/polydopamine nanolayers by self-assembly. For this polydopamine-modified bioceramic scaffold (DOPA-BC), under 808 nm NIR laser irradiation (0.38 W/cm^2) for 10 min, the mortality rate for OCs was 80.4%–99.2% in vitro and the tumor site temperature rapidly reached above 50°C, leading to a significant anti-tumor efficiency in vivo. Additionally, the trabecular bone volume fraction (BV/TV) achieved approximately 15% after being implanted for 8 weeks, showing the bifunctional potential of DOPA-BC. Yao et al.[38] prepared the slurry mixture by stirring and used 3D printing technology to fabricate HA/PDA/CMCS bioceramic scaffolds. The temperature could maintain at 58°C under 808 nm NIR laser irradiation (1 W/cm^2) for 10 min, and the OCs necrosis rate reached 73.3% in vivo. Additionally, the photothermal effect might further cause apoptosis and fewer blood vessels, inhibiting tumor cells (Figure 3(a)).

Notably, the low toxicity and high degradation capacity of the natural substances (hemin) or biomimetic materials (PDA)[12] exhibit significant advantages compared to other photothermal agents, such as metal elements and carbon-based nanomaterials. Metal materials are difficult to biodegrade and may be hazardous in the long term.[131] Carbon-based nanomaterials are potentially toxic and may lead to pulmonary inflammation.[132] Furthermore, regarding PDA's osteogenic function, some modified scaffolds have already shown excellent performance in bone regeneration.[117] Therefore, organic PCAs with simple synthetic and loading routes and high biosafety and bioactivity have gradually gained popularity for further applications in bone tissue engineering.

Synthetic organic materials. The HOMO-LUMO energy gap (HLG), defined as the energy separation between the HOMO and the LUMO, determines the optical characteristics of organic materials.[133] Therefore, PDA performs good absorbance in NIR due to its small and appropriate HLG.[134] In addition to natural substances like PDA, researchers also developed synthetic organic photothermal conversion agents (PCA), such as indocyanine green,[135] polyaniline,[136] and polypyrrole.[137] Intricate excogitation, laborious synthetic protocols, and the technical problems of loading such organic PCAs into bone bioceramic scaffolds inhibit the development of organic PCAs to some

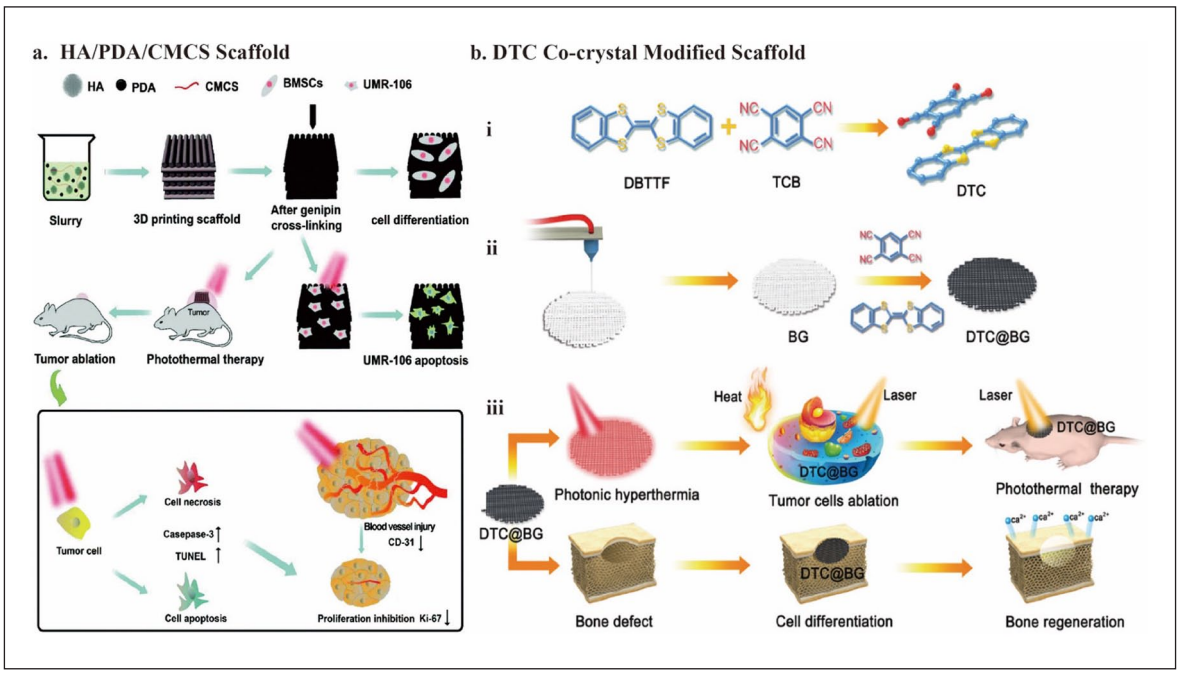

Figure 3. Schematic illustration of the fabrication of the organic nanomaterials modified 3D bioceramic scaffolds: (a) fabrication of HA/PDA/CMCS composite scaffolds by stirring and 3D printing technology and their bioapplication for osteogenesis and anti-tumor activity, (b) schematic illustration for the formation and application of bifunctional DTC@BG scaffolds. The co-crystal of DTC with a facile fabrication process exhibits potential for both photothermal conversion and osteogenesis. Cited with permission.[38] Copyright 2021, *Biomater. Sci.*[14] Copyright 2020, *Adv. Funct. Materials*.

extent.[14] Therefore, designing organic PCAs with simple synthetic and loading routes is essential.

Recently, organic charge-transfer crystals have been used for PTT. Because of the noncovalent interactions between donor and acceptor units, the co-crystals were self-assembled. Therefore, these organic PCAs are simple and economical to fabricate. They also exhibit modulated photophysical and physicochemical properties.[14] Its narrow HLG realizes the absorption in the NIR region.[138,139] Using dibenzotetrathiafulvalene (DBTTF) as the electron donor and tetracyanobenzene (TCB) as the electron acceptor, Xiang et al.[14] developed a DTC co-crystal with excellent photothermal conversion capabilities. By evaporating the DBTTF/TCB solution, numerous black DTC co-crystals grew in situ on the 3D-printed BG. It showed excellent tumor-killing ability with apparent cell death (80%) under 808-nm NIR laser irradiation (1.5 W/cm^2) for 10 min. Moreover, in addition to BG, the DTC co-crystal itself also accelerates the promotion of new bone formation through the up-regulation of gene expression of ALP, BMP-2, OCN, and RUNX-2. The percentage of bone volume (BV/TV $\times$ 100%) was 43.5 $\pm$ 2.7%, and bone mineral density (BMD) was 4.8 g·m^3 after implantation for 8 weeks (Figure 3(b)). For the osteogenesis ability of the DTC co-crystals, the increase in scaffold surface roughness could facilitate the attachment and proliferation of hBMSC.[15,99] Furthermore, the sulfur (S) element in DTC can promote protein uptake by interaction with proteins to promote osteoblast proliferation and differentiation.[140,141]

This study is notable for being the first to include organic charge-transfer co-crystals in scaffolds for osteosarcoma treatment. Electron-acceptor and electron-donor compounds self-assemble through noncovalent interactions to synthesize organic co-crystals. The co-crystals realize the in situ growth only by evaporation.[14] Usually, the in situ growth of nano agents, such as MoS_2 nanosheets,[91] Cu-TCPP nanosheets,[12] and $CuFeS_2$ nanocrystals,[99] is achieved by a hydro- or solvothermal process. The reaction system requires high temperature (180°C–240°C) and high pressure, while the reaction system of DTC@BG scaffolds requires only room temperature.[14]

Carbon-based nanomaterials. Besides organic PCAs, carbon-based nanomaterials also show excellent photothermal conversion ability. Indeed, carbon-based nanomaterials such as graphene oxides (GOs), carbon nanotubes (CNTs), and carbon dots (CDs) often possess PTT and PDT properties. In this section, we mainly illustrate GO's PTT property. Other CBNs will be discussed in detail later. In 2004, Novoselov and Geim obtained graphene by mechanical separation. Graphene is a two-dimensional (2D) material with a hexagonal honeycomb shape formed by the sp2 hybridization of carbon protons. It possesses outstanding

thermal and electrical conductivities. It has excellent electrical and thermal conductivities.[142] Graphene and its derivatives exhibit substantial NIR absorption and a high photothermal conversion efficiency owing to the conjugation effects. Additionally, graphene is cytocompatible and exhibits no significant toxicity in vivo. Furthermore, because of its unique nanostructure, it can promote bone regeneration. Therefore, graphene is considered the most representative and promising carbon-based nano PCAs.[143–145]

Graphene oxide. Graphene oxide is the first reported photothermal tissue engineering scaffold material. Using the solvent soaking approach, Lee et al.[146] and Zhang et al.[147] introduced GO to change the surface of the 3D-printed β-TCP scaffolds. COO^- in GO forms a valence bond with Ca^{2+} in β-TCP. Adjusting the GO concentration, surface modification time, and NIR power density can successfully control the temperature of the GO-TCP scaffold between 40°C and 90°C. The GO-TCP scaffold's unique photothermal action kills 92.6% of OCs in vitro and 83.28% in vivo under 808 nm NIR (0.36 W/cm^2) irradiation for 10 min (Figure 4(a)).[15] Furthermore, GO-modified β-TCP scaffolds could up-regulate OCN, RUNX-2, and BSP gene expression for osteogenesis. The new bone area reached around 33% after implantation for 8 weeks.[118] Furthermore, a study reported that GO could relieve IL-4-induced macrophage M_2 polarization and weaken the invasion and migration of OCs.[118] Therefore, these studies further confirm the effectiveness and significance of GO applied to anti-OCs bone tissue engineering.

Derivates of graphene oxide. With the in-depth study of GO, some articles have revealed several out-of-control abilities of GO. Previous studies showed that GO exhibits severe cytotoxicity in various biological systems due to its abundant surface functional groups, which can induce apoptosis by increasing intracellular ROS.[148–150] Unlike photothermal therapy, such ROS is like a sword without a sheath and cannot selectively kill tumor cells. While killing tumor cells, ROS also damages normal tissues and inhibits bone regeneration. In this regard, researchers tried to modify GO to scabbard the ROS sword. In particular, a study showed that reduced graphene oxide (rGO) has good photothermal conversion ability.[151,152] Furthermore, by removing abundant toxic functional groups on the GO surface, rGO showed more potential for osteogenesis. Several other studies reported that rGO could significantly induce directional differentiation of BMSCs into osteoblasts and promote bone regeneration.[153,154] Li et al.[155] fabricated the nHA-rGO scaffolds by heating the nHA-GO scaffolds at 300°C under the nitrogen flow to reduce the oxygen groups on the surface of the GO. After 808 nm NIR laser irradiation for 20 min (W/cm^2), only 8% of the OCs survived on the nHA-rGO scaffolds, while the rate for nHA-GO was 34%.[153] After implantation for 8 weeks, the new bone area reached 65%.[155] The successful application of rGO suggests that valuable innovation does not necessarily have to be built on empty ground. Extracting the essence and removing the dross to modify existing functional materials is also very meaningful.

In addition to modifying GO, other components can be introduced to obtain GO derivatives. The 2D-borocarbonitride (BCN) nanosheets contain graphene and boron nitride (BN) domains.[156] The B element is critical for mineralization and osteogenesis.[157] Therefore, BCN preserves the photothermal therapeutic efficacy and improves its osteogenesis ability. Zhao et al.[10] manufactured ultrathin BCN nanosheets at 900°C under nitrogen flow. In addition, they deposited BCN nanosheets onto 3D-printed AKT scaffolds by the facile dip-coating method. After implantation of BCN@AKT scaffolds, the tumor region temperature in vivo could rapidly increase to 52°C under 808 nm NIR laser irradiation (0.30 W/cm^2), and few OCs could survive. Furthermore, BCN nanosheets' numerous hydroxyl functional groups (–OH) and boron (B) components promote bone regeneration.[10] In detail, the B element activates the BMP-2 signaling pathway. Unlike some cytotoxic groups on the surface of GO, -OH groups up-regulate the expression of the fibronectin protein in the extracellular matrix (ECM), which promotes the adhesion of BMSCs and accelerates mineralization (Figure 4(b)).[10] Notably, whether it is by the direct reduction of GO[153] or the synthesis of nanosheets containing a graphene structure,[10] both maintain or even improve the photothermal therapeutic efficacy of GO. In addition, both methods reduce the cytotoxic effect of GO and improve osteogenesis. Both are treated at high temperatures during synthesis under nitrogen gas flow.[10,153] This raises the question of whether treating photothermal agents with nitrogen gas flow at high temperatures is a helpful method in reducing cytotoxic groups on the surface of PCAs and improving their osteogenic ability.

Cu and other transition metals. Similar to introducing the osteogenic element B in BCN, Cu-based scaffolds are also favored in anti-osteosarcoma scaffolds due to their osteogenic property and photothermal efficiency.[158] Cu ions can also stimulate endothelial cell proliferation and differentiation by mimicking hypoxia. They stabilize the hypoxia-inducible factor-1α (HIF-1α) expression, which can induce angiogenesis by up-regulating the expression of TGF-β and VEGF.[94,159] Therefore, the Cu-based scaffold can simultaneously induce osteogenesis and angiogenesis by up-regulating the expression of osteogenic genes (ALP, OCN, BMP-2, and RUNX-2) and angiogenic genes (VE-cadherin (VE-cad), VEGF, and endothelial nitric oxide synthase (eNOS)).[94]

As a transition metal, Cu also shows excellent potential for photothermal therapy due to electronic transitions.[160] Furthermore, transition metals have toxic effects on tumor

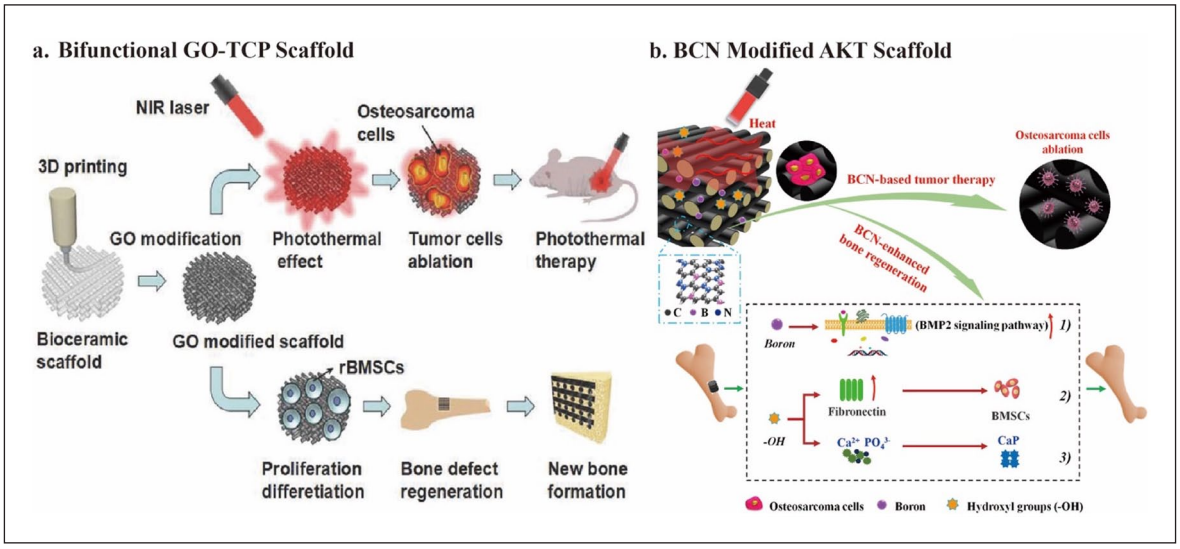

Figure 4. Schematic illustration of carbon-based nanomaterials modified 3D bioceramic scaffold fabrication: (a) formation of bifunctional GO-TCP scaffolds and their bio-application, (b) fabrication of bifunctional BCN@AKT scaffolds and their bio-application. Containing graphene and BN domains, 2D BCN nanosheets preserve photothermal therapeutic efficacy and improve osteogenesis capacity. Cited with permission.[15] Copyright 2016, *Adv. Funct. Materials*.[10] Copyright 2020, *Chemical Engineering Journal*.

cells.[161] Specifically, the fabrication of Cu-based scaffolds mainly includes the fabrication of Cu-containing 2D nanosheets,[94] Cu-containing mesoporous silica nanospheres,[17] or the direct incorporation of Cu into bioceramic powders.[100] All the above agents can be easily loaded onto the scaffold using facile in situ growth or spin-coating technology. Naturally, other transition elements, such as Fe,[12] Mo,[91] Mn,[100] and Co,[100] also show good therapeutic potential for bone tumors. And the manufacturing protocols are very similar to Cu-based scaffolds. We describe them along with Cu and make comparisons.

Metal-organic frameworks. Copper-coordinated tetrakis (4-carboxyphenyl) porphyrin (Cu-TCPP) is a porphyrin metal-organic framework (MOF) that can be produced as 2D nanosheets and has an outstanding photothermal response to NIR irradiation.[162] MOFs are ordered crystalline materials with permanent pores,[163] often manufactured by covalently linking metal ions to clusters of polytopic organic ligands.[164,165] Their high surface area and tunable pore structure enable central metal ions to play a more stable and efficient photothermal effect. Dang et al.[94] successfully realized the in situ growth of a novel 2D Cu-TCPP nanosheet on the β- TCP scaffold by 3D printing and the solvothermal method. Cu-TCPP in the form of 2D nanosheets shows superior photothermal characteristics compared to bulk materials. The low thickness of the nanosheets enables rapid response to NIR light, and the coexistence of Cu^{+} and $Cu^{2}+$ lays the foundation for high NIR absorption through the transition of the d–d energy band.[162] Therefore, the Cu-TCPP-TCP scaffold performed great tumor-killing ability, with a 90% OCs mortality rate under NIR irradiation (1.0 W/cm^2) for 10 min. Besides, it showed osteogenic ability with around 40% new bone area after implantation for 8 weeks by up-regulating ALP, OCN, RUNX-2, and BMP-2 expression. It also showed angiogenic ability with up-regulation of VE-cad, VEGF, and eNOS expression.[94]

After successfully fabricating the Cu-TCPP-TCP scaffold, Liu et al.[100] set out to discover more promising 2D MOF nanosheets. As previously mentioned, hemin is another low-toxicity and degradable potential photothermal agent naturally distributed in the human body. This avoids the tedious steps of artificially synthesizing MOFs. Furthermore, as a transition element, Fe endows hemin with the potential for PTT. However, the high hydrophobicity owing to the large macrocycle of tetrapyrrole and the low solubility in the neutral aqueous phase hinders the biomedical use of hemin.[166] Specifically, for bone tissue engineering, how to load hemin onto the scaffold with high biological activity and utilization rate is an urgent problem to solve.[167] Using PDLLA as a medium, Dang et al.[12] successfully integrated hemin particles and DOX into 3D-printed bioglass scaffolds. PDLLA is a biocompatible and biodegradable polymer that has attracted significant interest as a medium for scaffold modification. Combining chemotherapy and photothermal therapy significantly improves tumor-killing efficiency and reduces therapeutic side effects. Under an 808-nm NIR laser irradiation (0.7 W/cm^2) for 10 min, the tumor site achieved a controlled temperature of 48°C, with around 85% tumor cell mortality rate (Figure 5(a)).

Notably, the tumor-killing effect of hemin loading is not as good as that of Cu-TCPP loading, which may relate

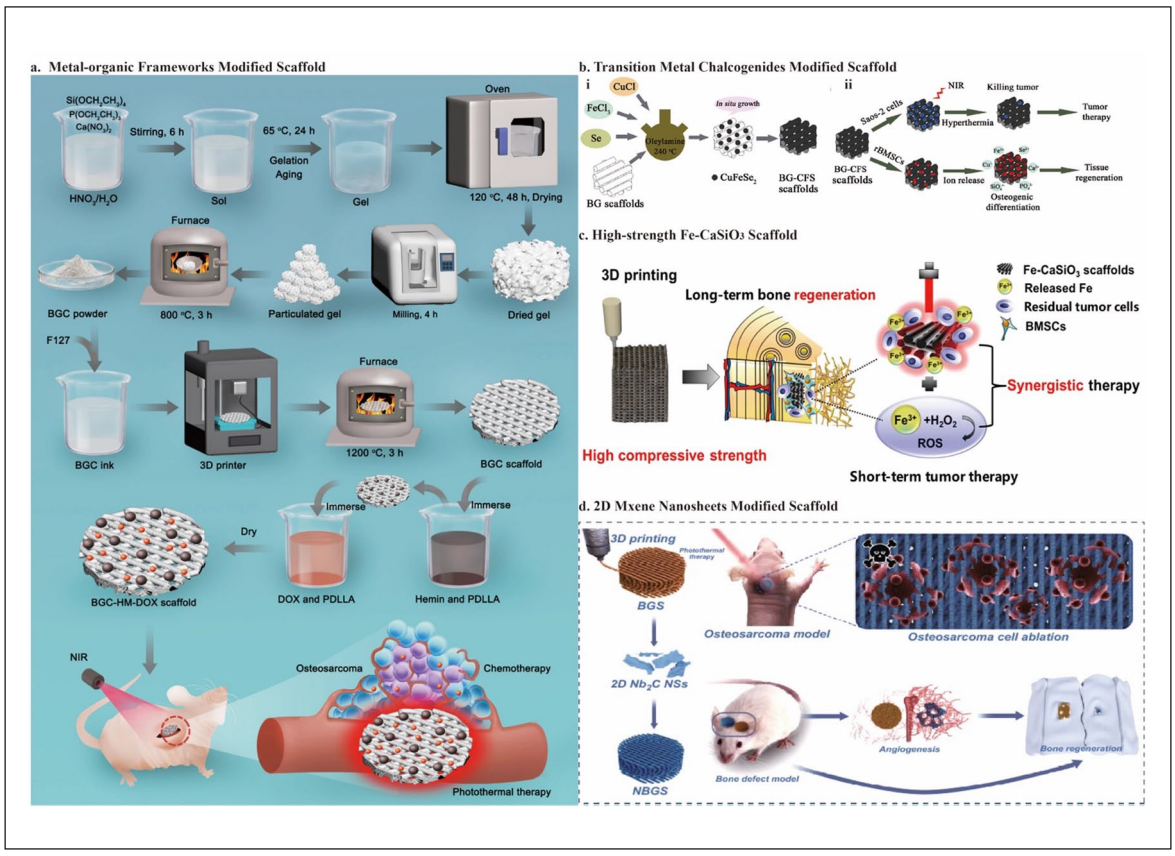

Figure 5. Schematic illustration of the fabrication of 3D bioceramic scaffolds modified with transition metal-based nanomaterials: (a) fabrication of the BGC-HM-DOX scaffold and its use in the treatment of osteosarcoma by combining photothermal therapy and chemotherapy. Hemin particles and DOX are inserted into 3D-printed BGC scaffolds using the polymer PDLLA as a medium, (b) schematic illustration of $CuFeSe_2$ nanocrystals growing in situ on the surface of BG scaffolds and their dual function of anti-tumor treatment and tissue regeneration, (c) fabrication of high-strength Fe-$CaSiO_3$ scaffold and their potential use in synergetic photothermal-chemodynamic anti-tumor therapy and concurrent osteogenesis promotion, (d) the photothermal osteosarcoma ablation process and bone regeneration of NBGS are shown schematically. Vascularization can also be promoted to facilitate osseous reconstruction. Cited with permission.[12] Copyright 2021, *Chemical Engineering Journal*.[99] Copyright 2018, *Biomaterials*.[119] Copyright 2018, *NPG Asia Materials*.[104] Copyright 2021, *Nano-Micro Lett.*

to the transition elements. It was demonstrated that Cu has a better photothermal conversion efficiency than Fe under NIR irradiation.[100] Further, by integrating plasmonic metal nanoparticles with MOFs, the absorption in the NIR region of MOF can be enhanced due to the wide tunable LSPR band of the plasmonic metal. Therefore, this is a worthwhile attempt to improve the photothermal efficacy of MOFs.[168] Moreover, unlike Cu's excellent osteogenic and angiogenic ability, hemin did not show its potential for bone regeneration. For this issue, Pan et al.[169] have obtained a mesoporous MOF using a pore-forming template to achieve controlled release of a BMP pathway activator. Therefore, the osteogenic properties of the scaffold can be improved.

Transition-metal chalcogenides. Besides coordination with organic materials, Cu-based chalcogenides, such as CuS,[170] $CuCo_2S_4$, and $CuFeSe_2$,[99] are also promising PCAs due to their ease of fabrication, controllable size, decent photostability, variable composition, and low-cost.[171,172] For example, $CuFeSe_2$ has good photothermal ability due to its narrow energy band (0.16 eV) in the solid state. $CuFeSe_2$ nanocrystals may develop in situ on the supporting surface of the 3D-printed BG scaffold through the solvothermal method. The results have shown that the tumor site temperature can be elevated beyond 48°C with more than 74% death of OCs in vitro and 96% in vivo, under an 808-nm NIR laser irradiation (0.55 W/cm^2) for 10 min. Besides, the released Cu, Fe, Si, Ca, P, and Se ions can synergistically stimulate BMSCs and increase the expression of osteogenic genes (OCN, osteopontin (OPN)), as well as ultimately promote new bone formation (23.2% BV/TV and 8.22% new bone area after implantation for 8 weeks) (Figure 5(b)).[99]

In addition to Cu-based chalcogenides, other transition metal chalcogenides (TMD) also show excellent photothermal conversion ability. MoS_2 nanomaterial exhibits 7.8 times higher absorbance than GO in the NIR region,

and its mass extinction coefficient ($\lambda = 800$ nm, 29.2 L/g) is similar to that of rGO (24.6 L/g/cm).[173] Therefore, it possesses remarkable photothermal therapeutic efficacy on OCs. Similar to the fabrication of Cu-based chalcogenides scaffolds, Wang et al.[91] successfully realized the in situ growth of 2D MoS_2 nanosheets on the surface of the 3D-printed AKT scaffold through a hydrothermal reaction. The viability of OCs in the MS-AKT decreased to roughly 5% after three treatments with an 808 nm NIR laser (0.60 W/cm^2) for 10 min. The necrosis rate reached 89% in vivo. After loading this MoS_2 nanosheet, the ability of the AKT scaffolds to enable sound diffusion, attachment, and proliferation of BMSCs was also preserved, and enhanced bone-related gene expressions, such as ALP, RUNX-2, OCN, and OPN, were observed.[91] 2D nanosheets containing transition metal elements exhibit excellent application prospects. Whether it is coordinating with organic materials[94] or in the form of transition metal chalcogenides,[91,99] the manufacturing idea is to find some biocompatible transition-fast elements as photothermal agents. Besides, a simple hydrothermal or solvothermal method can always realize the in situ growth of 2D nanosheets.[91,99]

Transition metal in the non-compound form. Sometimes, nanoparticles and nanosheets metabolize poorly and might induce long-term biological toxicity.[100] Therefore, transition metals in non-compound forms draw attention. Liu et al.[100] used transition metals' osteogenic and photothermal abilities, directly doped them into the bioceramic powder, and obtained the scaffold by 3D printing. The method is facile and economical. More importantly, it is the first research to compare the osteogenic ability and photothermal efficacy of various transition metal elements. Regarding the photothermal order, it was demonstrated that Cu-BGC > Fe-BGC > Mn-BGC > Co-BGC. By irradiating with 808 nm laser (0.75 W/cm^2) for 15 min, the tumor tissue necrosis rate of Cu-BGC, Fe-BGC, and Mn-BGC achieved 94.9%, 90%, and 72%, respectively. There is no significant difference between Co-BGC and the control group. Notably, the released ionic products have osteogenic and angiogenic abilities. Fe and Mn-BGC scaffolds stimulated the expression of osteogenic genes (ALP, OCN, OPN, BMP-2, and BSP) and promoted the adhesion and proliferation of BMSCs. Co-BCG up-regulated the VEGF expression and favored cell adhesion, while the number of BMSCs was significantly low. In fact, low Co^2+ concentrations can promote the adhesion and proliferation of BMSCs, whereas high concentrations can induce cytotoxicity and lower cell viability.[174] Therefore, the burst release of Co^2+ ions on the first day decreased the number of BMSCs. Furthermore, although Cu-BGC scaffolds contained many BMSCs, the cells were spherical with fewer pseudopodia. This is also due to the toxicity of the burst release of Cu^2+ on the first day. This does-dependent turnover effect is significant and incites us to explore trace elements' appropriate concentration and release curve when designing multifunctional scaffolds.[100]

Furthermore, researchers can obtain new excellent functional materials by changing the non-compound transition metal's dispersion. By changing the dispersion form of the elements, significant heterogeneous Fenton reactions can occur on dispersed single-atomic iron sites within highly active single-atomic iron catalysts (FeSACs), leading to excellent anti-tumor therapy with integrated PPT and CDT. Wang et al.[102] prepared FeSACs using a template-sacrifice method using MgO nanoparticles as templates. The pyrolysis of the iron-phenanthroline complexes (Fe(phen)x) allows iron to be dispersed at the atomic level. Then, the FeSACs were effectively impregnated and distributed in the interconnected structure of 3D-printed BG. At increased laser power density (1.5 W/cm^2), the local temperature reached 53°C in 5 min when $FeSAC_{500}$-BG was irradiated by an 808 nm laser, showing outstanding photothermal properties. Meanwhile, significant heterogeneous Fenton reactions can occur at the dispersed single-atomic iron sites in response to H_2O_2 in the TME to generate highly reactive·OH, leading to lethal damage to OCs. Through the combination of PPT and CDT, 89.27% and 95.34% OCs mortality was achieved at FeSAC concentrations of 500 and 1000 μg/mL, respectively. FeSAC-BG also up-regulated the expression of osteogenic genes collagen type I (COL-1), BMP-2, OCN, and RUNX-2. After implantation for 16 weeks, the average recovery percentages of bone defects for BG and FeSAC-BG achieved 87.3% and 94.3%, respectively.[102]

In addition to achieving the combination of PPT and CDT, Fe also has superior fatigue resistance and high mechanical strength, making it fit for repairing load-bearing bone defects. However, its low biodegradability and bioactivity hinder its further application for bone tissue engineering. On the contrary, bioceramic scaffolds, as previously described, have better biodegradability and can stimulate vascularization and new bone formation. Compared to cancelous bone defect regeneration, cortical one requires harder bone replacement implants, and no bioceramic scaffold can achieve the mechanical strength required for cortical bone. Ma et al.[119] used a simple ball milling and 3D printing technique to fabricate a Fe-$CaSiO_3$ composite scaffold (mass percentage: 30% $CaSiO_3$ and 70% Fe) scaffold called 30 CS. Complementing the advantages of Fe and bioceramic scaffolds, the 30 CS has high compressive strength, exhibits synergistic effects of PPT and CDT, and can promote bone regeneration. Under an 808 nm laser (0.80 W/cm^2) irradiation for 10 min, the temperature of the tumor site reached over 50°C, and the released Fe ions catalyzed the Fenton reaction. Therefore, the mortality rate of OCs reached 91.4%, and almost all OCs nuclei dissolved after treatment for 15 days in vivo. After implantation for 8 weeks, BV/TV and new bone area achieved around 16% and 17%, respectively (Figure 5(c)).[119]

2D MXene nanosheets. We have previously introduced some 2D nanosheets (NSs), such as BCN graphene derivatives and transition metal dichalcogenides. For ultrathin NSs, almost all atoms are exposed on the surface and have an enhanced surface area ratio. These features significantly improve their chemical and biological reactivity, enabling NSs to exhibit excellent photothermal properties. In addition to the above, nitrides and carbonitrides (MXenes), as a combination of graphene derivatives and transition metals, are becoming increasingly popular. In 2D MXenes, "M" stands for a transition metal atom (Ti, Zr, Nb, Sc, Ta, and Mo), "X" denotes C and/or N, and the "ene" suffix, which is derived from "graphene," indicates a material with an ultrathin 2D structure. MXenes have a large surface area and multiple terminal functional groups (–OH, –O). They are generally manufactured by selective etching of the Al layer (Al, Zn, Si, and Ga) with hydrofluoric acid (HF) and then exfoliating the original bulk MAX-phase MAlX ceramics with tetrapropylammonium hydroxide (TPAOH). The exposed terminal metal sites on the surface of MXenes enables them to form strong interface connection to bioceramics and to react actively. MXenes also have excellent electroconductibility, ensuring rapid migration and efficient separation of photogenerated electrons.[16,104,175,176]

After etching bulk Ti_3AlC_2 ceramics with HF and intercalating with TPAOH, Pan et al.[16,177] prepared delaminated ultrathin Ti_3C_2 NSs. These Ti_3C_2 NSs were modified onto a 3D-printed BG scaffold using the facile soaking method. Once the scaffold was implanted, under an 808 nm NIR laser irradiation (1.0 W/cm^2) for 10 min, the tumor site temperature climbed to 63°C. This resulted in OCs survival rates lower than 25% in vitro and complete ablation in vivo without recurrence. Simultaneously, by interacting with water and oxygen, Ti_3C_2-MXenes may degrade and release titanium-based species, which significantly up-regulates osteogenic gene (RUNX-2, COL-1, OPN, and OCN) expression and promotes BMSCs differentiation. After implantation for 8 weeks, the BV/TV and BMD achieved 50% and 60 g·m^3, respectively, which showed good bone regeneration in vivo.[76]

2D Nb_2C MXene NSs, like Ti_3C_2, are highly biocompatible and biodegradable, showing excellent photothermal conversion efficiency in NIR-II.[178,179] Under NIR-II laser irradiation (1064-nm laser irradiation) at a power density of 1.0 W/cm^2, the integrated Nb_2C NSs have a specific photon response, with deeper tissue penetration, and inhibit over 62% OCs. In addition, the biodegradation of Nb_2C provides enough space for bone reconstruction. Furthermore, the released Nb-based species may greatly enhance blood vessel repair and migration at the defect region by up-regulating VEGF and fibroblast growth factors (FGF)-2 expression. The newborn vessel area reached 38% after implantation for 3 weeks.[104] The new vessels can deliver more oxygen, energy, and vitamins for bone regeneration and recruit more immune cells, thus accelerating the degradation of the scaffold and killing OCs. The Nb-based species also significantly up-regulated osteogenic gene (RUNX-2, COL-1, OPN, and OCN) expression for bone regeneration. After implantation for 24 weeks, the BV/TV and the BMD achieved 45% and 65 g·m^3, respectively (Figure 5(d)).[104]

LSPR accounts for the light-to-heat conversion of MXenes.[122] The osteosarcoma inhibition rate of MXenes is approximately 50%–75%,[76,104] whereas some classical photothermal agents, such as GO, PDA, and Au, can often reach approximately 90%.[15,117] MXenes mainly rely on LSPR for their photothermal effects, and M is a transition metal element (Ti or Nb) rather than a classical plasmonic metal (Au or Ag). Although the photothermal effect is not ideal, combining other anti-tumor methods improves tumor-killing ability.[101] Concurrently, Ti and Nb release after MXene degradation promotes bone regeneration.[76,104] Therefore, considering the long-term prognosis of osteosarcoma, MXenes are a promising choice for osteosarcoma treatment.

Plasmonic nanomaterials. MXene's photothermal effect mainly depend on LSPR, but because M (Ti or Nb) is often not a classical plasmonic metal (Au or Ag), the tumor inhibition rate is usually only about 50%–75%.[16,104] The traditional plasmonic metal has good efficacy in tumor PTT, with an inhibition rate of over 90%.[180] However, the high cost and complex preparation procedure are not conducive to large-scale clinical applications and drive researchers to seek an alternative. As a compound containing the elements La and B, LaB_6 has free electrons on its surface and shows strong NIR absorption via LSPR.[181] Furthermore, La has physicochemical properties similar to Ca and can trigger a bone regeneration response.[182] At the same time, Boron (B) can stimulate the expression of osteoinductive growth factors and improve the renewal of the ECM.[140] Therefore, LaB_6 can effectively promote bone regeneration. Dang et al.[98] successfully prepared LaB_6 micro-nano particle/poly (D,L-lactide)-modified 3D-printed β-TCP scaffolds (TCP-PDLLA-LB) by soaking. This LaB_6-surface chemically-enhanced TCP-PDLLA-LB scaffold has improved mechanical strength on par with human cancelous bone. It also shows remarkable photothermal and osteogenesis abilities. By irradiating with an 808 nm laser (0.70 W/cm^2) for 10 min, the bone tumor temperature immediately reached over 50°C. It eventually maintained at 53°C, with the viability of the OCs decreasing below 24%. Additionally, the new bone area reached 36% after implantation for 8 weeks with up-regulation of osteogenic gene expression (RUNX-2, COL-1, BMP-2).[98] As a plasmonic metal, La has a better LSPR effect than Ti and Nb and a lower cost than Au and Ag. It also shows good biocompatibility and osteogenic ability.[98,182] Therefore, La deserves further in-depth studies for developing multifunctional scaffolds against osteosarcoma.

Other 2D nanomaterials. We have introduced many 2D photothermal nanomaterials above, but in-depth studies have gradually exposed their deficiencies. For example, as application domains have expanded, graphene's zero bandgaps have increasingly become its fatal flaw. In addition, due to its wide bandgap, hexagonal boron nitride (h-BN) has insulator characteristics, whereas transition metal dichalcogenides (TMDs) have low carrier mobility.[183,184] Moreover, due to the narrow bandgap, metal-like MXenes exhibit a weaker LSPR effect than classical plasmonic metals.[185,186] Therefore, 2D materials with well-balanced properties are currently being explored. 2D black phosphate (BP) breaks the properties of the bound energy bands of graphene, h-BN, and MXenes, presenting a thickness-dependent band gap ranging from 0.3 eV (bulk size) to 2.0 eV (monolayer).[187] The material also shows higher carrier mobility than TMD[188] and significant near-infrared absorption and photothermal conversion capability. BP NSs also have excellent biocompatibility with non-toxic and osteogenic degradation products. Moreover, the photothermal materials' degradation rate, such as GO and MoS2, is too slow. In contrast, the degradation rate of PDA is too fast (40% weight loss in phosphate-buffered saline within 24 h). Therefore, controlled degradable BP NSs are superior to those materials.

The high surface-to-volume ratio and agent-loading function of BP NSs also allow them to load chemotherapy drugs or antibodies for improved OCs clearance.[189–191] Wang et al.[11] prepared water-in-oil phase emulsions bioinks and then cryogenically 3D-printed to generate the DOX/P24/BP/TCP/PLGA (BDPTP) scaffold. The temperature of the BDPTP scaffolds can exceed 60°C under an 808 nm NIR laser irradiation (0.5–2.0 W/cm^2) for 10 min. This accelerates the release of DOX, and the synergistic effect of chemotherapy and PTT can achieve rapid and complete tumor eradication without recurrence. Besides, the sustained release of peptides (P24) up-regulates the osteogenic gene (RUNX-2, COL-1, OCN, and ALP) expression and promotes new bone formation. The BV/TV reached 38 ± 5%, and the BMD achieved 38.5 ± 5 g·mm^3 after implantation for 3 months. In this study, the BPTP scaffold (without DOX) could achieve the same anti-tumor therapeutic efficacy as the BDPTP scaffold on day 4 (both tumor volumes decreased from 200 to 0 mm^3). However, after 16 days of implantation, tumor recurrence occured in the BPTP group, and the volume increased to approximately 200 mm^3, while the BDPTP group remained at 0.[11] This is due to the sustained release of low concentrations of DOX in BDPTP scaffolds, which also kill difficult-to-observe residual microtumors, thus inhibiting tumor recurrence. Furthermore, this article also suggests that evaluating treatment efficiency requires delaying the observation time after implantation to monitor tumor recurrence better, thus improving the prognosis.

Magnetothermal therapy (MTT)

As mentioned, photothermal agents show great potential in hyperthermia tumor ablation but may damage normal tissues under high-power irradiation.[113] Besides, NIR penetration into deep tumors is relatively insufficient because superficial tissues interfere with photons.[192] These hinder the further clinical application of PTT for deep solid tumors like OS. Conversely, MTT uses radiofrequency electromagnetic waves and has no penetration depth limitations. As such, MTT is a viable option for treating deep in situ OS.[193] However, the product of frequency and magnetic field amplitude should be limited to less than 5×10^9 mA/s for safety.[194] Therefore, the MTT temperature range is constrained. Moreover, there are specific temperature requirements for killing tumors. Temperatures between 41°C and 46°C induce cell apoptosis,[114] whereas temperatures beyond 46°C induce necrosis.[195] Therefore, the temperature limitation of MTT hinders its efficiency in anti-tumor therapy.

Magnetic alloy and magnetic metal oxide nanomaterials are two groups of magnetic agents that are categorized depending on their structural characteristics. If Cu (Cu, Cu-TCPP, CuS, $CuFeS_2$)[17,94,99,100] shines in metal-containing photothermal agents, then Fe is likely the core and soul of magnetothermal agents. Fe obtains excellent magnetic properties. However, Fe alloys lose their magnetism due to low stability and strong oxidation reactivity. The magnetic metal oxide nanoagents, including Fe_3O_4, γ-Fe_2O_3, and ferrites ($M(Fe_xO_y)$), exhibit advantageous magnetic and dielectric properties.[196] Table 3 outlines the magnetothermal agents loaded into 3D-printed bioceramic scaffolds for osteosarcoma treatment.

Fe alloy. Fe alloy is unstable and may even lose magnetization. However, when combined with other materials, its stability enhances, and the added diamagnetic particles become ferromagnetic after doping with Fe ions.[197] As previously indicated, adding transition metal elements into bioceramic scaffolds may provide the materials with outstanding photothermal characteristics. In addition, an appropriate concentration of iron ions can promote the proliferation of BMSCs.[100] Zhuang et al.[92] developed Fe-doped 3D-printed AKT scaffolds using the sol-gel method and 3D printing technology. Combining PTT and MTT reduces the excitation dose, allowing both the penetration depth and the adequate temperature to be achieved for better tumor hyperthermia therapy. Fe alone does not have an excellent LSPR effect as Au and Ag, so the photothermal efficiency is not high. In addition, Fe alloy is highly unstable, which significantly reduces its magnetothermal effect.[92] However, when Fe-AKT scaffolds were irradiated under NIR and AMF simultaneously, a combination of imperfections led to perfection. Overall, this combination

Table 3. Magnetothermal agents added to the 3D-printed bioceramic scaffolds for osteosarcoma treatment.

Materials	Magnetothermal agents	Effect	Production Methods	Coating methods	Pore	Mechanical strength	Ref.
Fe + AKT	Fe	Photothermal therapy (808 nm,0.70 W/cm^2, 10 min, reached 47°C, 40.8% OCs mortality rate) + Magnetothermal therapy (896.8 A/m^2, 10 min, reached 43°C, 18.4% OCs mortality rate) (PTT/MTT, reached 53°C, 98% OCs mortality rate & Bone regeneration (up-regulation of RUNX-2, OPN, OCN, BMP-2) (latest advances, but lack of in vivo trials)	3D Printing (Extrusion with post-sintering)	Directly doped into the powder by sol-gel method	Pore size (450 μm)	Compressive strength (5.91–14.48 MPa, with the lower sintering temperature after adding Fe)	Zhuang et al.[92]
Fe_3O_4 + GO + β-TCP	Fe_3O_4	Magnetothermal therapy (magnetic field intensity of 180 Gs and 409 kHz, 20 min, tumor site temperature reached 42°C and kept for 20 min, mortality rate over 75%) & Bone regeneration (increased Alp activity, up-regulation of RUNX-2, OCN, OPN, and BSP) (latest advances, but lack of in vivo trials)	3D Printing (Extrusion with post-sintering)	Repeated soaking-drying	Pore size (300–500 μm)		Zhang et al.[95]
AKT-Fe_3O_4-CaO_2	Fe_3O_4	Magnetothermal therapy(500 kHz; output current, 22 A; coil diameter, 10 cm, tumor site temperature reached 55°C and kept for 1 min) + Chemodynamic therapy (mortality rate from 63.2% to 91.4% by adding CaO_2) & Bone regeneration (increased ALP activity, up-regulation of BMP-2, RUNX-2, OCN, and COL-1, 13% BV/TV and 25% new bone area after implantation for 8 weeks)	3D Printing (Extrusion with post-sintering)	Soaking			Dong et al.[52]
Fe_3S_4 + AKT	Fe_3S_4	Magnetothermal therapy (frequency: 560 kHz, coil radius: 3 cm, output current: 7.5 A, reached 50°C, 10 min) + Chemodynamic therapy (mortality rate 98.46%) & Bone regeneration (up-regulation of OCN, BSP, and RUNX-2 expression and enhanced COL-1 protein expression, 14% BV/TV after implantation for 12 weeks)	3D Printing (Extrusion with post-sintering)	In situ growth through hydrothermal method			Zhuang et al.[93]

enhanced the mobility of the surface electrons and facilitated the generation of both energy band transitions and collisions and frictions with atoms.[126] In fact, after 10 min, PTT (808 nm, 0.70 W/cm^2) and MTT (896.8 A/m^2) increased the scaffold temperature to 47°C and 43°C, respectively. Moreover, the viability of OCs decreased to 59.2% and 81.6% after irradiation. By combining the two therapy, the temperature reached 53°C, and the viability of OCs was less than 2%. Thus, the Fe-AKT scaffold can achieve ideal hyperthermia treatment at a low radiation dose, thus avoiding unexpected damage to normal tissues. Moreover, in addition to 3D bioceramic scaffolds, Fe can further up-regulate the expression of RUNX-2 and OPN for bone regeneration. Interestingly, Fe up-regulates BMP-2 expression with low Fe doping content (1%) while showing the turnover effect when the content increases (3%) (Figure 6(b)).[92]

Fe_3O_4. Considering the instability of Fe alloy, Fe_3O_4 is another hotspot of magnetothermal agents for bone tissue engineering. However, the magnetothermal efficiency of Fe_3O_4 may be hampered by the shielding effect of the bulk bioceramic and the weak heat conductivity of the bioceramics after incorporation.[198] Nevertheless, in addition to combining PTT with MTT to enhance hyperthermia antitumor efficacy, a thermal conductor is also a viable approach. For example, combining the magnetothermal agent (Fe_3O_4 nanoparticles) with a thermal conductor (GO) improved the hyperthermia anti-tumor efficacy. Zhang et al.[95] prepared a GO-Fe_3O_4-GO sandwich layer GO-Fe_3O_4-GO on the supporting surface of the 3D-printed β-TCP scaffold by soaking. Under AMF (intensity of 180 Gs, 409 kHz), after 20 min, when the temperature reached 42°C, the mortality rate of OCs achieved more than 75%. Furthermore, the sustained released Fe ions further increase the activity of ALP and up-regulate the expression of RUNX-2, OCN, OPN, and BSP (Figure 6(a)).[95] Considering the success of the combination of PTT and MTT[92] in vitro, additional in vivo trials are needed to validate further the effectiveness of placing such a Fe-based scaffold under both NIR and AMF irradiation.

Besides the combination of PPT and MTT, another strategy for compensating for temperature limitations is to combine MTT with chemodynamic therapy (CDT). CDT is an emerging anti-tumor strategy that uses CDT agents to convert H_2O_2 into the •OH, the most harzardous ROS through the Fenton/Fenton-like reactions, which causes cell apoptosis and necrosis.[199] The Fe_3O_4 nanoparticles can catalyze the Fenton-like reaction in the acidic TME. However, the low concentration of intratumoral H_2O_2, typically below 50 μM, is insufficient to generate large amounts of ROS to inhibit tumor growth effectively. Dong et al.[52] coloaded calcium peroxide (CaO_2), as H_2O_2 sources, with Fe_3O_4 nanoparticles in 3D-printed AKT scaffolds by soaking to construct a multifunctional "all in one" bioceramic scaffold. Under AMF (500 KHz; coil diameter, 10 cm; output current, 22 A), the temperature of the AKT-Fe_3O_4-CaO_2 scaffold in pH 7.4 and 6.0 reached 75°C and 63°C, respectively. The ROS generation ability test showed that mild acidity and raised temperature could accelerate the Fenton-like reaction and enhance the generation efficiency of •OH. After the temperature reached 55°C and kept the AMF irradiation for 1 min, the mortality rate of OCs reached 63.2% and 91.4% for the AKT-Fe_3O_4 scaffold and AKT-Fe_3O_4-CaO_2 scaffold, respectively. Ca^{2+} ions released from CaO_2 enhance the osteogenic ability of the 3D bioceramic scaffold with increased ALP activity and up-regulation of osteogenic genes (BMP-2, RUNX-2, OCN, and COL-1). After implantation for 8 weeks, the BV/TV reached 13%, and the new bone area reached 25% (Figure 6(c)).

Other Fe-containing magnetothermal materials. Along with Fe_3O_4, Fe_3S_4 has garnered considerable interest for its magnetothermal property. By integrating Fe_3S_4 microflowers with 3D-printed AKT scaffolds using a hydrothermal method, Zhuang et al.[93] designed a multifunctional platform for the postoperative treatment of osteosarcoma. To mimic acidic and redox TME, diluted HCl and 200 μmol H_2O_2 were added to the culture media (pH = 6.5). The normal culture meida (pH = 7.4) without H_2O_2 was used to mimic the normal tissue microenvironment. When the temperature reached 50°C under AMF (frequency: 560 kHz; coil radius: 3 cm; output current: around 7 A) and was kept for 10 min, the mortality rate of OCs reached 98.46% in the former group (MTT/CDT) and 85% in the latter group (MTT). After treatment for 3 days, hematoxylin and eosin (H&E) staining showed no identifiable OCs remaining in the Fe_3S_4 AKT + AMF group (MTT/CDT), while in the blank and Fe_3S_4 AKT groups (CDT), OCs were still visible. These showed that MTT and CDT could kill OCs effectively in a synergetic way. Fe_3S_4 microflowers further up-regulated osteogenic gene expression (RUNX-2, OCN, and BSP) and COL-1 protein expression. BV/TV reached 13% after implantation for 12 weeks. Notably, Fe_3S_4 also shows a turnover effect on osteogenesis as Fe in Fe-AKT. The osteogenic ability increased with increasing Fe content, reaching a maximum when the precursor concentration reached about 0.02 M, after which it started to decrease.[93] Unlike the AKT-Fe_3O_4-CaO_2 scaffold, Fe_3S_4-AKT did not have an additional source of H_2O_2, but the tumor inhibition rate was even higher (98.46% for Fe_3S_4-AKT, 91.4% for AKT-Fe_3O_4-CaO_2, and 63.2% for AKT-Fe_3O_4).[92,93] Therefore, Fe_3S_4 probably has a better magnetothermal property than Fe_3O_4, and further verification is needed. Furthermore, considering the effect of the electron-hole pair of TMD, Fe_3S_4 may also have good photothermal properties. The effect of synergetic PPT/MTT/CTT treatment on OS and the osteogenesis ability can be further explored by adding NIR irradiation

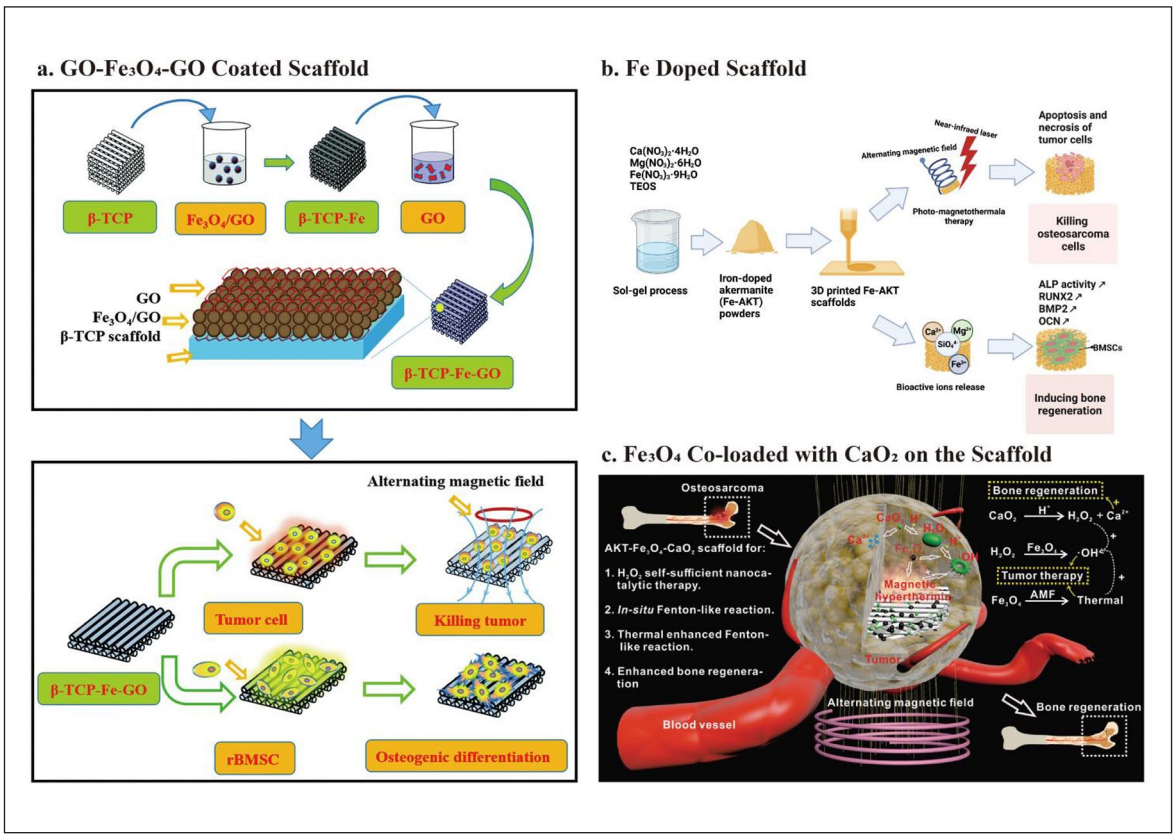

Figure 6. Schematic illustration of the fabrication of the Fe-based nanomaterials modified 3D bioceramic scaffolds for MTT: (a) fabrication of the β-TCP scaffolds coated with a GO-Fe_3O_4-GO layer and its use in the treatment of osteosarcoma by combining PTT with MTT, (b) schematic diagram of the fabrication of Fe-doped AKT scaffolds and dual function of Fe in PTT and MTT, (c) schematic representation of the anti-tumor and bone-regeneration ability of 3D-printed AKT scaffolds loaded with Fe_3O_4 and CaO_2 nanoparticles. CaO_2 nanoparticles generated ample H_2O_2 in an acidic tumor microenvironment. Fe_3O_4 nanoparticles catalyze a Fenton-like reaction to convert H_2O_2 to •OH. This reaction shows the potential of Fe_3O_4 in combining chemodynamical properties with magnetotherapy against osteosarcoma. Cited with permission.[95] Copyright 2016, *J. Mater. Chem. B*.[92] Copyright 2019, *American Chemical Society*.[52] Copyright 2019, *Adv. Funct. Materials*.

to explore the optimal balance of death and regeneration. In short, Fe exhibits photothermal, magnetothermal, osteogenic, and chemodynamic potential for osteosarcoma treatment.[52,92,95] Moreover, when two or more therapies are combined, the OCs mortality rate is often over 90%.

In addition to the Fe, Fe_3O_4, and Fe_3S_4, other Fe-containing nanomaterials have also shown potential for MTT. Superparamagnetic iron oxide NPs (SPIONs) are small synthetic γ-Fe_2O_3 (magnetic hematite) or Fe_3O_4 (magnetite) particles with core diameters between 10 and 100 nm.[200] It is currently the preferred thermoseed for MH with excellent heating efficiency, nontoxicity, and biodegradability. It was the first therapeutic/adjuvant that was commercially available in Europe.[199] γ-Fe_2O_3 is more stable than Fe_3O_4 in the presence of oxygen, compensating for its lower volume saturation magnetization.[196] Kesse et al.[201] synthesized core (γ-Fe_2O_3)-shell (SiO_2-CaO) nanoparticles using the co-precipitation and sol-gel method. The heating efficiency of these NPs was comparable to that of commercialized magnetic NPs (the intrinsic loss power is in the range of 0.15–3.1 $nH \cdot m^2 \cdot kg$), thus demonstrating that the shielding effect of the bioactive shell did not exclude the NPs from being a promising candidate for MTT. Furthermore, the bioactive shell promotes the precipitation of HAp, which shows its potential for bone regeneration after tumor ablation. $CuFe_2O_4$ is a spinel ferrite-based magnetic material with excellent magnetothermal capacity. Bigham et al.[202] synthesized a multifunctional bioactive core ($CuFe_2O_4$)-shell (Mg_2SiO_4) disk for bone tumor treatment using the sol-gel combustion method. The Mg_2SiO_4-$CuFe_2O_4$ disks reached the intended temperature for tumor ablation (41°C–46°C) in exposure to the 200 Oe magnetic field. Moreover, the disks also showed excellent apatite-formation performance. Therefore, this Mg_2SiO_4-$CuFe_2O_4$ disk is also a viable option for concurrent bone tumor ablation and new bone formation. However, neither of these studies conducted in vitro or in vivo trials to further validate its anti-tumor and osteogenesis abilities. In addition, how to effectively load them into 3D-printed bioceramic scaffolds and efficiently combine nanomaterials' anti-tumor and osteogenesis

abilities with the mechanical strength, patient-specific geometry, and hierarchical structure of the scaffolds are also needed for their further application in bone tissue engineering.

A new use of an old approach: Chemotherapy

If hyperthermia therapy is now the most common strategy of multifunctional scaffold for OS treatment, chemotherapy is the treatment that has been thought of and is still valued today. Since the anti-tumor mechanisms of conventional drugs are well-defined, researchers are more concerned with achieving their controlled and TME-responsive release for better anti-tumor performance. In addition, a number of drugs used in other areas have been newly tried for OS. Chemotherapy is crucial in treating osteosarcoma, especially unresectable high-grade metastatic OS. Since the introduction of chemotherapy, long-term survival rates have climbed from 20% to 70%.[56] Surgery with postoperative chemotherapy is the standard clinical treatment for osteosarcoma. The neoadjuvant chemotherapy strategy has also been developed.[203] The first-line medications are MAP: methotrexate, doxorubicin, and cisplatin. These drugs prevent OS by activating TP53, destroying DNA, and raising intracellular ROS levels.[204] However, some chemotherapy drugs have a "double-edged" effect that simultaneously damages both OCs and normal cells. This is known as targeted toxicity. Cisplatin and doxorubicin are hazardous to several organs, including the kidney and heart.[205] To minimize the side effects of drugs on healthy tissues and organs, drug delivery systems with controlled release modalities and high efficiency of target therapy are receiving increasing attention. In particular, scaffold-mediated local chemotherapy with precise targeting minimizes drug distribution and side effects. It is a promising strategy for treating residual tumors and recurrence after surgery.[96] In addition, some drugs used to treat other diseases, such as curcumin and metformin, are helpful in the treatment of osteosarcoma and in promoting bone regeneration after controlled release and concentration and have even shown the potential to reverse drug resistance. Table 4 outlines the chemotherapy drugs loaded into 3D-printed bioceramic scaffolds for osteosarcoma treatment.

Classical anti-osteosarcoma drugs. Recently, researchers have attempted to load classical chemotherapeutic drugs into bioactive scaffolds with time- and space-controlled release to enhance chemotherapeutic efficiency and reduce side effects. Dang et al.[84] designed a multifunctional platform to realize synergistic effects of PTT and chemotherapy for osteosarcoma using PDLLA as a medium with TiN particles and DOX sequentially coated on the surface of a 3D TCP scaffold. PTT enhanced the tumor-killing performance and effectively reduced the severe side effects of high-dose chemotherapy. Additionally, DOX release overcame the spatial limitations of PTT. The TCP-TN-DOX scaffold was developed as a drug carrier for in situ implantation into osteosarcoma, which offers advantages over intravenous drug injection with reduced toxicity and damage. There were no significant changes in body weight and major organs in mice, suggesting that this in situ implantation strategy allowed for negligible side effects of DOX. The drug release showed an initial burst release, followed by sustained drug release of DOX in the scaffold, with DOX accumulation peaking at 60% at 48 h. This prolonged the action time and prevented excessive accumulation in a short period to avoid side effects. Under NIR irradiation (0.6 W/cm^2 for 10 min), TCP-DOX and TCP-TN resulted in 53.7% and 22.9% apoptotic cell death, respectively. For TCP-TN-DOX, the apoptosis and necrosis rates reached 63.94% and 14.2%, respectively, indicating the synergistic effect of PTT and chemotherapy on OS. After implantation for 18 days, mice in the TCP-TN-DOX + NIR group had completely controlled tumors without recurrence and had minimal relative tumor volume (1.39 ± 0.08) compared to the monomodal therapy group. Besides, both titanium and 3D-printed bioceramic scaffolds can promote bone regeneration. However, the researchers did not conduct bone-regeneration-related in vitro and in vivo tests to explore the bone-regeneration capability of this TCP-TN-DOX scaffold (Figure 7(a)).[84]

In addition to loading into porous scaffolds for sustained release, a responsive on-demand drug release in-situ drug delivery system has also been developed. Zhang et al.[96] developed a 3D-printed gelatin/shell scaffold using gelatin with DOX as the core part and $SrCuSi_4O_{10}$ (SC) nanosheets/β-TCP as the shell part of the printed filament. The SC nanosheets conferred photothermal function to the scaffold. Under NIR-II laser irradiation at 1064 nm laser (1 W/cm^2), the tumor temperature reached 52°C, and OCs died. At the same time, the increased temperature induced the gel-sol transition of gelatin, which initiated the on-demand release of DOX from the loosened gelatin. In vitro and in vivo trials showed that PTT and chemotherapy had a synergistic anti-tumor effect, causing essentially 100% OCs death, 98.53% of which in the form of apoptosis. There was no discernible change in the body weight of the mice and no significant harm to the major organs after treatment, indicating that this low-dose, on-demand, localized in situ drug delivery system is well suited to avoid side effects. In addition, this core/shell scaffold has a good osteogenic ability. The degradation of gelatin leads to hollow channels in the scaffold and provides a clear structural cue for new bone formation. Meanwhile, the degradation of SC nanosheets promoted the sustained release of active ions such as Sr, Cu, and Si. These bioactive ions further promoted vascularization (up-regulation of VEGE, HIF-1α) and bone regeneration (up-regulation of OCN, BMP-2, RUNX-2), reaching 20% BV/TV and 0.8 mg/cm^3 BMD after 8 weeks of implantation (Figure 7(b)).[96]

Both of the studies described the synergetic PTT/chemotherapy treatment against OCs. For single PTT, especially PTT in the NIR-I region, it is generally challenging to kill

Table 4. Agents loaded into 3D-printed bioceramic scaffolds for chemotherapy, photodynamic therapy, and gas therapy.

Materials	Therapeutic agents	Effect	Production Methods	Coating methods	Pore	Mechanical strength	Ref.
TCP + PDLLA + DOX + TiN	TiN & DOX	Photothermal therapy (NIR irradiation, 0.6 W/cm^2, the temperature of OCs reached 48°C, for 10 min) + Chemotherapy (63.94% apoptosis rate, and 14.2% death rate, no recurrence, with the minimal relative tumor volume of 1.39 ± 0.08)	3D Printing (extrusion with post-sintering)	Immersing (indichloromethane soluton)		Compression strength (from 12 to 28 MPa by PDLLA coating)	Dang et al.[84]
DOX-gelatin (core)/$SrCuSi_4O_{10}$-β-TCP (shell)	$SrCuSi_4O_{10}$ + DOX	Photothermal therapy(under 1064 nm laser irradiation, 1 W/cm^2 for 5 min, temperature of OCs reached over 52°C) + Chemotherapy (almost 100% OCs mortality rate) & Bone regeneration (up-regulation of OCN, BMP-2, RUNX-2, 20% BV/TV and 0.8 mg/cm^3 BMD after implantation for 8 weeks) & angiogenesis (up-regulation of VEGE, HIF-1α, CD31, and TGFβ1)	3D Printing (extrusion with post-sintering)	Immersing (applying vacuum)	Porosity(from 79.4 ± 2.7% to 65.3 ± 2.5% after gelatin filling)	Young's modulus (from 20 to 24 MPa with the addition of gelatin core)	Zhang et al.[96]
Liposome-encapsulated curcumin + β-TCP	Curcumin	Chemotherapy (96.44% OCs mortality rate at day 11) & Bone regeneration (increased ALP activity) (Recent advances, but in vivo trials still lacking)	3D Printing (extrusion with post-sintering)	Immersing	Pore size (400 μm)		Sarkar and Bose[97]
PLLA + nHA + MET	MET	Chemotherapy (apoptosis rate of OCs from 12.87% to 15.86%, up-regulation of BAX, Cas-3, and Cas-9) & Bone regeneration (increased ALP activity, up-regulation of BMP-2, RUNX-2, COL-1a1, and OCN, increased OCN3 and COL-1a1 protein expression) (Recent advances, but in vivo trials still lacking)	3D Printing (SLS)	Directly mixing when preparing powder	Pore size (100–300 μm[69]) & Porosity(81.46 ± 4.65% for PLLA/nHA/MET, and 51.56 ± 4.48% for PLLA/nHA)[69]	Young's modulus (33.42 ± 0.81 MPa for PLLA/nHA, and 10.84 ± 0.73 MPa[69])	Tan et al.[69]
Cyanobacteria + Ce_6 + $CaCO_3$-PCL	Ce6	Photodynamic therapy (over 90% OCs were killed, under 660 nm laser irradiation (0.2 W/cm^2, 10 min)) & Bone regeneration (up-regulation of OCN, OPN, and BMP-2 expression, enhanced ALP activity, around 40% BV/TV after implantation for 12 weeks)	3D Printing (3DP)	Polylysine and collagen assisted cell (CeCyano) attachment		Compressive strength (10.40 ± 0.20 MPa), comparable to trabecular bone (2–12 MPa)	He et al.[19]
2D Nb_2C-MXene-SNO + BG	NO & MXene	Gas therapy (10^{-6} to 10^{-3} M) & Photothermal therapy (under 1064 nm laser irradiation, 1.0 W/cm^2, 10 min, reached 52°C) (mortality rate of OCs reached 75%) & Bone regeneration (up-regulation of RUNX-2, BMP-2, COL-1, and OCN, 60% BV/TV and 0.6 g/cm^3 BMD after implantation for 16 weeks)	3D Printing (extrusion with post-sintering)	Soaking		Compressive strength (around 6–8 MPa)	Yang et al.[101]

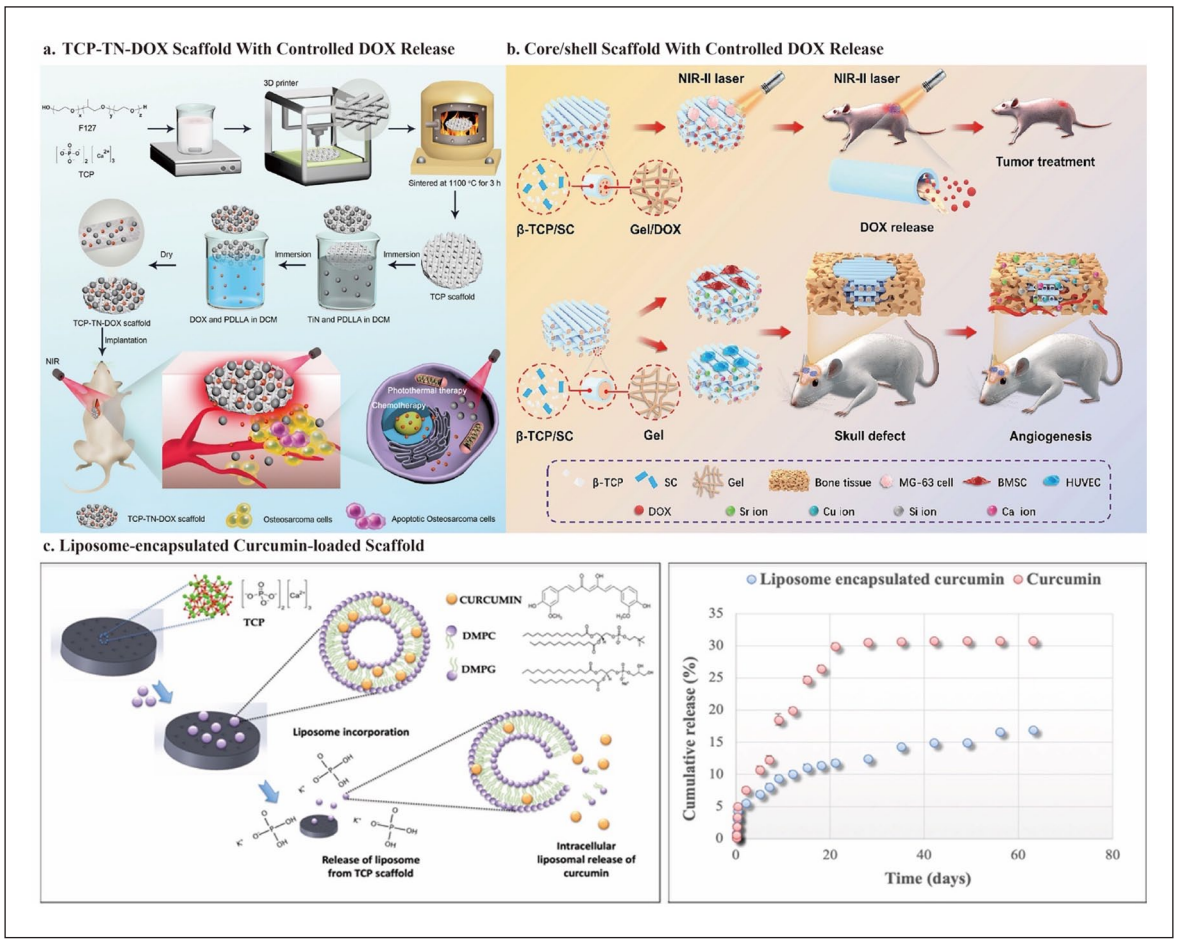

Figure 7. Schematic illustration of the fabrication of 3D bioceramic scaffolds with controlled drug release: (a) schematic diagram of the construction and application of the TCP-TN-DOX scaffold for treating osteosarcoma. The scaffold enables controlled release of DOX triggered by NIR irradiation and achieves synergistic effects of chemotherapy and photothermal therapy, (b) schematic depiction of the fabrication of DOX-gelatin/$SrCuSi_4O_{10}$-β-TCP core/shell scaffold. NIR-II irradiation triggers the on-demand release of DOX for precision chemotherapy. The hollow shell channels generated by core degradation and the released bioactive ions promote vascularized bone regeneration, (c) fabrication of liposome-encapsulated curcumin-loaded 3D-printed bioceramic scaffold to realize curcumin's controlled and prolonged release. Cited with permission.[84] Copyright 2021, *ACS Appl. Mater. Interfaces*.[96] Copyright 2023, *Chemical Engineering Journal*.[97] Copyright 2019, ACS *Appl. Mater. Interfaces*.

OCs effectively due to the presence of soft tissues like skin and muscle. Therefore, it is still prone to tumor recurrence and metastasis. For chemotherapy, conventional chemotherapy often leads to dose-related systematic side effects while killing tumors. After combination, chemotherapy compensates for the deficiency of photothermal therapy against deep and residual OCs. At the same time, PTT promotes drug diffusion in the tumor sites through the increased temperature and compensates for the lack of tumor-killing ability after reducing the drug dose to avoid side effects.[206–208]

Researchers have also designed TME-responsive drug target delivery systems based on in situ release for better anti-tumor effects and less normal tissue damage. For the acidic TME, Zakeri et al.[48] used an impregnation method to load Cis into the pores of Zeol nanoparticles and loaded NPs into 3D PCL scaffolds. The scaffold has a higher cumulative release amount and release rate of Cis in the acidic environment than in the neutral one, allowing for better OCs-targeted therapy. Due to the microscopic pore structure of Zeol, Cis showed controlled release in the scaffold with an initial 7-day burst release and sustained release after that. This controlled and targeted release leads to more than 75% OCs death by chemotherapy alone. Chu et al.[209] fabricated hollow copper ferrite (HCF) nanoparticles, coated them with polydopamine, and loaded them with doxorubicin (DOX). This NP also has well-controlled release and pH responsiveness. He et al.[210] developed a layer-by-layer assembled black phosphorus nanosheet/chitosan multifunctional composite coat and deposited it on 3D-printed polyetheretherketone bone scaffolds. Both BP and DOX have excellent pH-responsive controlled release.

This acidic-TME target Chem-PPT therapy achieved near complete tumor suppression with a 99% reduction in tumor volume at day 10.

Li et al.[211] further developed reduction/pH dual-responsive nanocarriers targeting the redox and acidic TME of OCs. They prepared amphiphilic poly(ethylene glycosylated poly(α-lipoic acid) micelles (mPEG-PαLA) for simultaneous delivery of the encapsulated paclitaxel (PTX) and DOX for osteosarcoma treatment. This PTX and DOX co-loaded nanoparticle exhibited better biodistribution and higher tumor inhibition in mice. However, no such TME-responsive drug delivery platform based on 3D-printed bioceramic scaffolds has been reported. Nanoparticles are commonly used as drug carriers with TME-responsive controlled release. If nanoparticles can be loaded into 3D-printed bioceramic scaffolds, scaffolds can achieve better targeted chemotherapeutic effects and induce bone regeneration that therapeutic nanoparticles cannot achieve. Nanoparticles are usually loaded into scaffolds by polymer coating or polyethyleneimine coating. However, this affects the scaffold's mechanical properties, bioactivity, and biocompatibility. Therefore, suitable and simple loading methods should be further investigated to maintain controlled and targeted chemotherapeutic drug release of NPs and the osteogenesis ability of 3D-printed bioceramic scaffolds.

Non-classical anti-osteosarcoma drugs. In addition to conventional chemotherapeutic drugs, some drugs with less toxic side effects used in other areas have been tried for OS treatment. Their safety has been well established in extensive past applications and therefore shows great potential for clinical translation. Turmeric's active ingredient, curcumin, is known for its anti-inflammatory, antioxidant, anti-tumor, and osteogenic activities. However, it shows extremely low bioavailability, fast metabolism, and quick systemic clearance. Sarkar and Bose[97] improved the bioavailability by encapsulating curcumin in liposomes via thin film hydrolysis and then incorporating it into a 3D-printed ß-TCP scaffold. Liposome-encapsulated curcumin showed a more controlled and sustained release than free curcumin over 60 days. Liposomal curcumin released from the 3D scaffold was cytotoxic to OCs, with OCs mortality reaching 54.59% on day 3 and 96.44% on day 11. Besides, the scaffolds also increased ALP activity and promoted osteoblast proliferation (Figure 7(c)). Chen et al.[47] fabricated SF/CM nanofibrous scaffolds using supercritical carbon dioxide technology. Through porogen leaching, they subsequently coated PDA on the scaffold. This SF/CM-PDA scaffold is also pH-responsive due to the accelerated breakdown of SF and the weaker interaction between SF and CM under acidic conditions. In the acidic TME, this pH-responsive scaffold achieves better release and penetration of CM at the tumor site. Under NIR irradiation, this scaffold exhibits an initial abrupt release of curcumin due to the low pH of TME and elevated temperature. This burst release results in high concentrations of CM, which can immediately eliminate residual OCs. As OCs die, the pH gradually increases. Moreover, the sustained release in a physiologically neutral environment results in low concentrations of CM that will further promote progressive healing and bone regeneration.

CM may prevent OCs proliferation and metastasis by downregulating Notch1 expression, NF-κB, and estrogen-related receptor α.[212,213] Interestingly, curcumin also plays an essential role in inducing osteoblast differentiation in BMSCs and alleviating RANKL-induced osteoclast resorption, which could promote bone regeneration.[214] Curcumin's promotion of normal osteoblasts and selective toxicity against osteosarcoma reflect the tailor-made philosophy and provide a more promising strategy for OS management. Vitamin K2 also exhibits similar tailor-made potential through the same pathway. Sarkar and Bose[214] used a plasma spraying technique to form a homogeneous HA coating on the Ti implant to enhance osseointegration. They loaded curcumin and vitamin K2 into the HA-coated scaffold using ethanol. On day 5, the percentage of new bone production reached 24%. On day 11, the mortality rate of OCs achieved 91.63%. In addition, curcumin demonstrated potential as a photosensitizer (PS) for PDT. Though the Ex of curcumin is only about 425 nm, fiber optic devices can allow it to pass through tissues such as skin for OS treatment. In addition, the hydrophobicity of curcumin also inhibits its PDT efficacy. PS can only be photoactive as a monomer, while curcumin aggregates in an aqueous environment with reduced excitability.[56] CM encapsulated in liposomes may be a potential solution.[56]

In addition to CM, metformin (MET), traditionally used for type 2 diabetes with minimal side effects and toxicity, has also shown potential in anti-tumor and osteogenisis.[215] Using SLS technology, Tan et al.[69] fabricated PLLA/nHA/MET scaffolds. MET release was pH-responsive, with prolonged drug release due to slowly degrading PLLA, and its drug release profile resembles the Higuchi model. The MET from the scaffold showed an initial burst release of 37.14% within the first 24 h, followed by a steady release for at least 1 month. More interestingly, MET had a turnover and tailor-made effect. A high dose of MET (above 10 mM) can cause OCs apoptosis or necrosis, whereas a low dose (under 1 mM) can promote BMSCs growth and differentiation. After MET addition, the apoptosis rate of OCs on the scaffold rose from 3.79% to 15.86% by activating the mitochondrial apoptosis pathway. Furthermore, MET increased ALP activity and increased osteogenic gene expression (BMP-2, RUNX-2, OCN, and COL-1) and protein expression (OCN3 and COL-1a1) for bone regeneration. Notably, although it also shows the tailor-made potential based on the turnover effect of concentration, the anti-tumor ability of MET is

not strong as CM. Therefore, it should be combined with hyperthermia therapy to promote the release of MET[216] and improve its anti-tumor therapeutic efficacy for further application. In a word, through loading new drugs like curcumin and metformin into 3D-printed bioceramic scaffolds, multifunctional scaffolds for OCs-killing and bone regeneration are achieved.

New method: Photodynamic therapy and gas therapy

Photodynamic therapy (PDT). In addition to hyperthermia therapy and chemotherapy, recently, PDT and gas therapy have been gradually showing potential for application in multifunctional scaffolds for OS treatment. PDT has recently gained popularity for its spatiotemporal controlled therapeutic efficacy, minimally invasive capabilities, and low systematic toxicity.[217] PDT involves three elements: photosensitizer, light, and oxygen. PS is activated by light and converts tissue oxygen into harmful ROS, which may lead to oxidative damage of cellular substrates, such as amino acids, proteins, and DNA. This effectively achieves anti-tumor effects through tumor cell death, vascular damage, and immunological responses.[218,219] PDT has been clinically applied to treat various diseases, such as lung and esophageal cancer, together with the approval of various PS, such as Photolon (chlorin e6, Ce6).[220] However, there are still two main problems in the clinical translation of PDT for anti-OC. First, the incompatibility requirement of high energy and deep tissue penetration limits the treatment of deep solid tumors. When light wavelength increases, the penetration depth of the tissue increases. However, the energy decreases at the same time. To meet the minimum energy required for ROS generation, the light wavelength usually does not exceed 850 nm.[221] This determines a tissue penetration depth of no more than 3 mm.[222] Second, oxygen-dependent PDT exacerbates oxygen deficiency.[223] HIF-1 is overexpressed in tumor cells under acute hypoxic circumstances, which induces OCs survival and ultimately results in resistance to PDT.[224] Worse still, tumor hypoxia could impair tumors' ability to respond to targeted and cytotoxic therapies, increasing genetic instability and contributing to metastasis.[225,226] This would eventually create a vicious loop in which incomplete PDT worsens tumor relapse and metastasis, like a domino effect.

For tissue penetration limitation, some PS, such as BP and C_{60}, are more photostable, less photobleaching, and less oxygen-dependent than traditional PS, such as tetrapyrrole. However, their poor absorption in the NIR limits their application.[227,228] This deficiency has recently been addressed by extending the absorption spectrum of PS to longer wavelengths through conjugating with light absorbers such as upconversion nanoparticles (UCNP) and GO. To increase the penetration depth, BP nanosheets are conjugated with UCNP to generate a significant amount of ROS and exert a potent anti-tumor effect under an 808 nm irradiation.[229] Besides, photoinduced electron transfer of GO-C_{60} systems can occur from the excited graphene to the ground state of C_{60}. Therefore, it can realize PPT and PDT simultaneously under an 808 nm irradiation.[230]

Carbon-based nanomaterials often have strong NIR optical absorption and high phototherapeutic efficiency. In addition, their low toxicity, adjustable surface structure, easy functionalization, high photostability, and tunable absorption-emission spectra allow them to show potential for integrated tumor treatment for multimodal imaging and PPT/PDT therapy.[46] Singh et al.[49] prepared multicolor fluorescent fBGn with 3-aminopropyltriethoxysilane as a surface functionalization agent through a direct and label-free method. Calcination at 400°C provided fBGn with high fluorescence intensity derived from carbon dot (CD), enabling trimodal emission (fluorescence, two-photon, and Raman imaging). The excellent photo properties of fBGn also enabled it to exhibit the ability of synergetic PDT/PTT therapy. 50% and 60% OCs mortality rate was achieved through monomodal PDT (660 nm) and PPT (808 nm), respectively, while the mortality rate of synergetic treatment was close to 100%. In addition, its mesoporous structure and $Ca^{2}+$ ions of BG allow the loading and controlled release of chemotherapeutic drugs such as DOX in a pH-responsive manner. Considering the bioactivity of BG, fBGn may also have an osteogenic ability, but this was not validated in article.[49] Overall, carbon-based nanomaterials enable a multifunctional integrated cancer treatment nanoplatform with trimodal real-time imaging and PDT/PPT/chemotherapy. Lu et al.[231] fabricated CS/nHA/CD scaffold by simple physical mixing and lyophilization. Out of the scaffold's biological activity and pore structure, the zero-dimensional carbon dot itself can also increase the ALP level in BMSC and up-regulate osteogenic genes like OCN and COL-1. After 4 weeks of implantation, it increased the bone density by an additional 21.65 mg/cm^3 based on CS/nHA scaffold and further promoted collagen and blood vessel formation.[231] Carbon nanotubes and graphene have also been reported to have osteogenic ability.[232] Suppose these carbon-based nanomaterials can be loaded into 3D bioceramic scaffolds while retaining their functionality. In that case, an integrated treatment and rehabilitation platform for patient-specific osteosarcoma management might finally be realized.

For another problem: vicious hypoxia loop, organic or inorganic catalysts, such as catalase,[225] manganese dioxide,[226] manganese ferrite nanoparticles,[233] and Mn (II) ions and pyropheophorbide engineered iron oxide nanoparticles[234] to catalyze O_2 production from endogenous H_2O_2 are used for more oxygen. Besides, the introduction of thylakoid membrane[235] and chlorella[236] to promote hydrolysis, the creation of artificial red blood cells to facilitate oxygen transport,[237] the reduction of the intratumoral

glutathione(GSH),[234] and the use of the HIF-1α inhibitor YC-1[238] are administrated through nanosystem for oxygen supplementation. However, oxygen is still insufficient due to the low in vivo H_2O_2 concentrations (<100 μM in tumor cells)[239] and the fact that only 0.7% of the nanosystem dose reaches the tumor site.[240] Therefore, it is a great choice to create inexhaustible oxygenation materials in situ with high controllability. The autotrophic light-triggered affording-oxygen green engine was developed using calcium alginate to shield Chlorella from phagocytosis. Then, it was minimally invasively inserted into the tumor tissue. Furthermore, PS (Ce6) was injected, resulting in simultaneous oxygen production and excellent PDT under 640 nm light irradiation. Based on this, excellent PDT and bone regeneration can be anticipated for osteosarcoma treatment if oxygen supplementation agents and PS can be loaded simultaneously into 3D bioceramic scaffolds.[223]

He et al. [19] modified Ce6 with bisamide-terminated polyethylene glycol polymer to enhance its hydrophilicity and positively charge it. They then co-cultured the resulting Ce6-NH_2 with cyanobacteria for internalization (denoting Ce6-NH_2 internalized cyanobacteria as CeCyano). They then soaked the 3D-printed $CaCO_3$-PCL (CaP) scaffolds in a solution containing polylysine and collagen to enhance the cell adhesion of CeCyano, thereby obtaining the CaPC scaffold. Under 660 nm irradiation (0.2 W/cm^2) for 10 min, CaPC scaffolds produced more $^1O_2$ than free Ce6, and these ROSs attacked the cell membranes of OCs and initiated lipid peroxidation chain reactions. Therefore, over 90% and approximately 80% OCs were killed in vitro and in vivo, respectively, with Ki67 expression down-regulation. Furthermore, due to its elevated O_2 content, the CaPC scaffold improved bone regeneration by up-regulating the expression of BMP-2, OPN, and OCN and enhancing the activity of ALP. The BV/TV achieved around 40% after implantation for 12 weeks (Figure 8(a)).[19] The subtlety of this design lies in the formation of CeCyano cells with integrated PS and oxygen sources by internalization of NH_2-modified PS (Ce6) and in the cell attachment of CeCyano to the 3D-printed bioceramics. Only by using polylysine and collagen to enhance cell attachment via protein adhesion, He et al. loaded the functional agent into the scaffold, which is simple and environmentally friendly.

Gas therapy. Besides PDT, NO-,[241] SO_2-,[242] H_2S-,[243] H_2-,[244] and CO-based[245] gas-generating nanoplatforms (GGN) have also been developed for cancer therapy. Effective gas therapy is performed by exogenous physical triggering like NIR irradiation or endogenous TME reactivity like acidity.[244,246] However, the in vivo application of these gases is exceptionally challenging due to their uncontrollable nature. For example, high NO concentrations in the blood (>1 mN) may lead to NO-toxicity risk, while low NO concentrations in tumor cells (10^{-12} to 10^{-9} M) unfortunately tend to promote cancer cell growth.[247,248] Therefore, controlled gas release and efficient gas delivery are essential for further clinical translation of gas therapy. Mesoporous SiO_2 ($mSiO_2$) shows excellent potential in GGN due to its high loading capacity due to the mesoporous structure and easy sulfation modification to conjugate with functional molecules like S-nitrosothiol (–SNO).[244,246]

Guo et al.[246] designed photo-triggered NO nanogenerators (PTNG) with a core-shell-shell structure (Fe_3O_4@polydopamine@mesoporous silica). The $mSiO_2$ shells were functionalized with sulfhydryl groups (–SH) to load PDA. The sulfated $mSiO_2$ was then conjugated with –SNO by a reaction of the -SH group with tert-butyl nitrite (TBN). They loaded DOX into the mesopores of PTNG. PTNG can absorb NIR photons at 808 nm and convert them into sufficient heat to induce NO release. The released NO successfully achieved multi-drug resistance reversal by inhibiting the P-glycol protein expression. As a result, intracellular accumulation of DOX could lead to high toxicity to drug-resistant tumor cells. Under 808 nm light irradiation for 5 min (1 W/cm^2), PTNG effectively inhibited drug-resistant tumor growth. However, PTNG did not show excellent photothermal efficiency, and the temperature in the tumor region only increased by 4°C after NIR irradiation. If other better photothermal agents like MXene were conjugated with $mSiO_2$, a better anti-tumor effect by synergetic chemotherapy-PPT might be achieved. Additionally, the researchers did not investigate the anti-tumor ability of NO itself.

In addition to NO, H_2 also shows potential in anti-OC. Yang et al.[244] constructed a mesoporous silica nanomedicine loaded with aminoborane (AB@MSN) to achieve high-load delivery and acid-controlled in-situ release of H_2 within the tumor. The fabricated AB@MSN nanomedicine has an ultrahigh H_2 loading capacity (130.6 mg/g, 1370-fold higher than conventional medicines (H_2@liposome nanodrug)). In addition, it is pH-responsive to target the acidic TME. Due to the stabilization of the interaction of hydrogen bonds between MSN and AB, the decomposition of AB is alleviated, resulting in sustained H_2 release (>2 days) that facilitates long-term hydrogen therapy and avoids the toxic effects of burst release. After AB@MSN injection for 20 days, the body weight was almost unchanged, the organs were not significantly damaged, and the tumor was inhibited. This high biosafety and anti-tumor potency open a new window for precise and efficient hydrogen therapy.[244]

The above MSN is meaningful for fabricating multi-functional 3D-printed bioceramic scaffolds for treating osteosarcoma. MSN can be loaded into 3D-printed bioceramics by a simple spin-coating method,[17] which does not require chemical modification, high temperature, or pressure conditions and can retain the properties of MSN well.[246] Therefore, the MSN conjugated with -SNO and photothermal agents by sulfidation or loaded with various functional agents through its mesoporous structure is

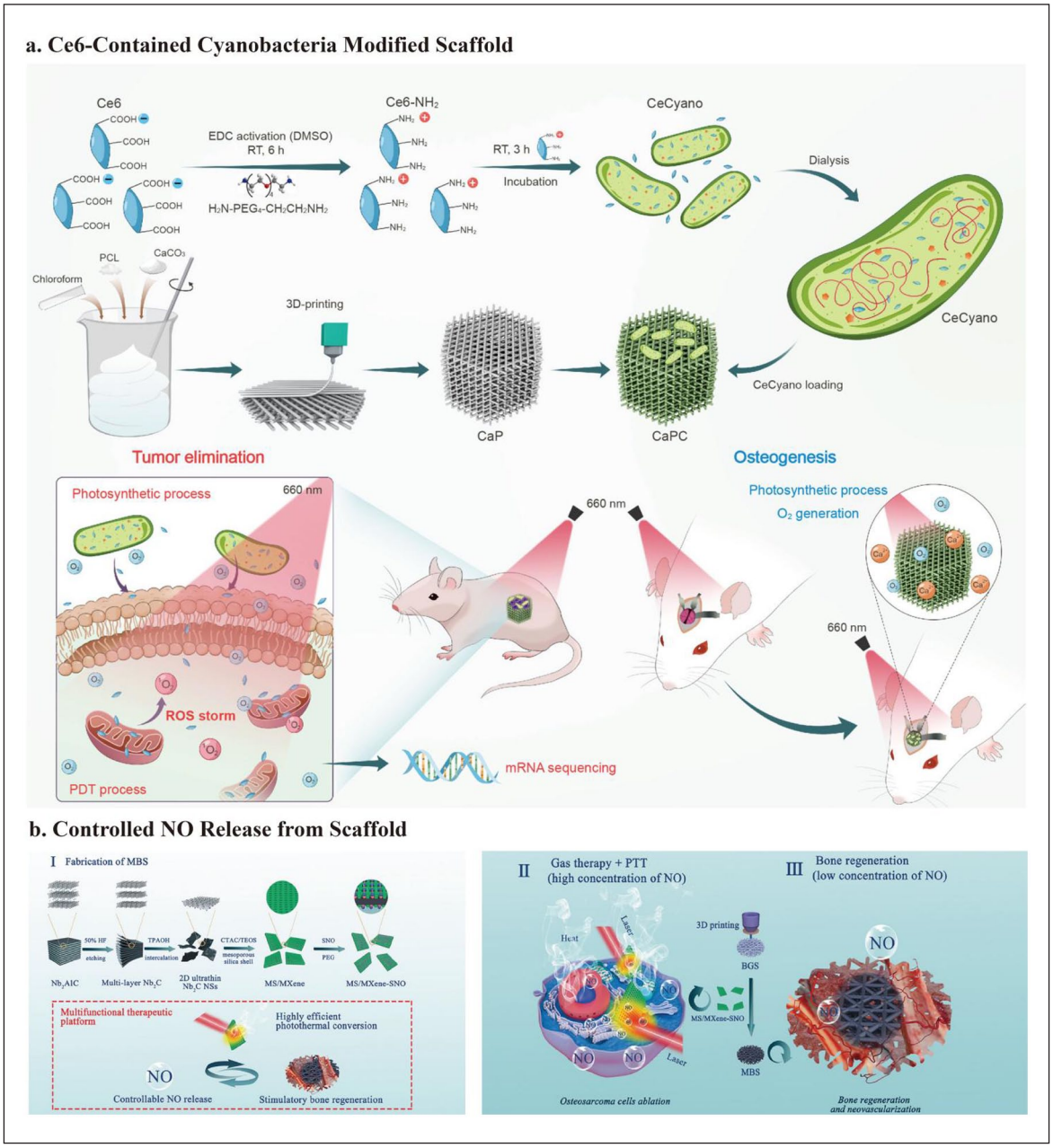

Figure 8. Schematic illustration of the fabrication of 3D bioceramic scaffolds for photodynamic therapy or gas therapy: (a) inspired by plant photosynthesis, photosensitive and photosynthetic Ce6-contained cyanobacteria were loaded onto the scaffold to overcome the hypoxia tumor environment for PDT. Local oxygenation also promoted bone regeneration, (b) construction of multifunctional scaffolds with controlled NO release, high photothermal conversion efficiency, and osteogenesis ability. NO has a turnover effect, which induces OCs apoptosis at high concentrations and promotes bone regeneration at low concentrations. Cited with permission.[19] Copyright 2021, *Nano Today*.[101] Copyright 2020, *Small*.

expected to realize multifunctional scaffolds integrating several therapies.

In fact, researchers have implemented the above idea to construct a multifunctional scaffold based on gas therapy. Yang et al.[101] fabricated a 3D MS/MXene-BG-SNO scaffold by incorporating a mesoporous silica-coated 2D Nb_2C MXene (photothermal agent) with the loaded S-nitrosothiol (NO donor) into the large holes of the 3D-printed BG scaffold by soaking. By using cetyltrimethylammonium chloride (CTAC) and ethyl orthosilicate (TEOS) as pore formers and silicon sources, respectively, they deposited a mesoporous SiO_2 shell layer on the surface of Nb_2C-NSs (MS/MXene). After modification with PEG silane, they mixed MS/MXene with mercaptopropyltriethoxysilane (MPTES) and tert-butyl nitrite (TBN) to prepare MS/MXene-SNO. Under 1064 nm laser irradiation (1.0 W/

cm^2) for 10 min, the temperature increased to 52°C and induced tumor cell apoptosis and necrosis. Simultaneously, as the temperature increased, S-NO bonds were activated and broke, thus accelerating NO release. The mortality rate of OCs reached 75% with the combination of gas therapy and PTT. Controlled NO release is essential for the sequential adjuvant killing of tumors, angiogenesis, and osteogenesis. The burst release of NO under NIR irradiation achieves a high NO concentration, and the slow and sustained release without irradiation achieves a low NO concentration. As curcumin and metformin, NO also has a dose-dependent turnover effect. High NO concentrations (1×10^{-6} to 1×10^{-3} M) induce cell dysfunction.[249,250] The oxidative and nitrosative stress induces DNA damage, and the enzyme nitrosylation inhibits DNA repair. Low NO concentrations ($\approx 10^{-9}$ M) typically improve endothelial cell proliferation and migration through cyclic guanosine 3′,5′-monophosphate (cGMP) signaling pathway.[251] The released low-concentration NO further up-regulates the osteogenic gene expression (OCN, RUNX-2, COL-1, and BMP-2). After implantation for 16 weeks, the BV/TV and BMD reached 60% and 0.6 g/cm^3, respectively (Figure 8(b)).[101] In a word, the MS/MXene-BG-SNO scaffold combines photothermal and gas therapies to kill OCs while promoting bone regeneration with low concentrations of NO and bioceramic scaffolds simultaneously.

Conclusions and perspectives

With an in-depth understanding of the functions of various nanomaterials and drugs, researchers began to apply these agents to 3D-printed bioceramic scaffolds. These modified multifunctional scaffolds could simultaneously kill residual OCs and promote bone regeneration in a patient-specific manner. Common modification methods include soaking, solvo/hydrothermal, spin coating, or directly doping the material into the powder. The common anti-tumor therapies used in multifunctional scaffolds include PTT, MTT, chemotherapy, CDT, photodynamic therapy, and gas therapy. Sometimes, just loading single functional agents into a 3D-printed bioceramic scaffold can successfully achieve a multifunctional scaffold with excellent anti-tumor and osteogenesis ability. Notably, combining two or more therapies can often achieve better anti-tumor effects and compensate for the deficiency of a single one. For example, the combination of PPT and MTT solves the problems of insufficient penetration depth of PPT and temperature limitation of MTT. The combination of PPT and chemotherapy solves the problems of insufficient killing against deep and residual OCs of PPT and the dose-dependent toxicity of chemotherapy. The combination of PPT and CDT compensates for the lack of immune response of PPT and deficiency of tumor-associated antigens of CDT and may inhibit metastasis better. Another example is the combination of gas therapy and chemotherapy, which solves the problem of drug resistance and enhance the anti-tumor ability. The combination of therapies is often achieved by simultaneously loading different functional agents into the scaffold to achieve an "all-in-one" scaffold. In addition, some agents themselves also show "all-in-one" potential. For example, Fe can realize the synergetic PTT/MTT or MTT/CDT, and fBGn can realize PTT/PDT/chemotherapy/multimodal imaging synergetic treatment. Therefore, researchers should have a broad understanding of nanomaterials with "all in one" potential in other fields, such as modified MSN and fBGn, and apply appropriate loading methods to load them into 3D-printed bioceramic scaffolds with their function preserved. Furthermore, the tailor-made and turnover effects exhibited by some agents such as Fe, curcumin, metformin, and NO also deserve further exploration to achieve better controlled release by physical excitation such as laser irradiation or responsiveness of TME to balance tumor killing and osteogenesis.

In addition, 3D-printed bioceramics are widely used in bone regeneration tissue engineering due to their osteogenic bioactivity, porous hierarchical structures, and bone-like physical-mechanical properties. However, the potential of this "hard" material continues beyond there. In recent years, bioceramics have also shown great potential in the regeneration of soft tissues that do not match their physicomechanical properties.[252] In fact, whether the application is in "hard "or "soft" tissues is fundamentally based on the similarity criterion. Bioceramics can be produced in a pliable and moldable manner, for example, the cotton-like 13-93B3 borate glass microfibers for wound healing.[253] They can also be incorporated into soft polymer matrices to obtain relatively flexible composites, as they are in bone tissue engineering incorporating PDLLA or doping with metallic materials such as Ag and Ti to enhance their mechanical strength.[254] Second, just like 3D-printed bioceramic scaffolds mimic the specific defect shape, internal structure, and composition of bone through 3D printing. This "hard" bioceramic should be carefully selected and designed according to the morphology, structure, and property of specific "soft" tissues, such as fibers for nerve regeneration, CBN with electrical conductivity for peripheral nerve conduits and cardiac patches, and doping with Cu and Si to promote angiogenesis.[255–258] Therefore, if the principle of similarity is deeply understood and applied, bioceramics will shine in bone and soft tissue engineering and achieve mutual translation.

In Section 4, we discussed in detail how each scaffold addressed the two main issues after OS surgery: residual OCs and bone defect. In addition, clinical OS treatment is currently facing problems of drug resistance, metastasis, and unideal diagnosis and evaluation of existing imaging systems.

As the drugs used to treat OS and in first-line chemotherapy regimens have mostly stayed the same in the last three decades, patients with unresponsive or refractory OS

due to intrinsic or acquired drug resistance usually have a poor prognosis. New treatment strategies are, therefore, urgently needed. PTT, MTT, novel chemotherapy, PDT, and gas therapy discussed in this review offer hope for these patients. It should be noted that drug resistance in osteosarcoma is usually due to mutations in drug transporter proteins, resulting in the inability of the drug to exert its anti-tumor effect. For example, drug efflux due to overexpression of efflux pumps, such as ABC transporters, leads to DOX resistance.[259] Besides, reduced drug uptake due to alteration in the expression of transporters such as SLCs prevents drug influx and leads to MTX resistance.[260] In response to the dilemma of treating unresponsive or refractory OS caused by the resistance of conventional chemotherapy, the new therapies mentioned above tear up the rulebook. These new strategies kill OCs by a mechanism completely different from conventional chemotherapy. Therefore, they do not need to enter OCs through transporters to exert anti-tumor effects. For example, PTT and MTT induce apoptosis and necrosis of OCs by increasing the temperature of the tumor site. New chemotherapeutic drugs can kill OCs through new pathways, such as Notch1 and NF-κB. The mechanism of tumor-killing of gas therapy such as NO is through the oxidative and nitrosative stress that induces DNA damage.

In addition to the improved anti-tumor efficacy of these therapies, some also showed potential in directly reversing multi-drug resistance. Curcumin reverses multi-drug resistance by down-regulating P-gp gene expression and inhibiting the P-gp efflux pump.[261] Metformin inhibits glucose uptake and ATP production in human OS CSCs by downregulating the expression of PKM2, weakening the resistance of CSCs to chemotherapy, and promoting drug-induced apoptosis.[262] NO depletes GSH, thereby reducing cisplatin inactivation and enhancing its anti-tumor efficacy. Besides, NO also reduces the expression level of P-gp and promotes intracellular accumulation of the drug at concentrations above the cell-killing threshold, ultimately reversing the drug resistance.[263] Furthermore, although ROS can activate specific chemoresistant genes like HIF-1α and P-gp, drug resistance in Cis has also been shown to be reversed after achieving control in the amount, area, and time of ROS release after combining with PDT.[264] Therefore, for multifunctional scaffolds, combining conventional chemotherapy with other therapies, such as novel chemotherapeutic agents, gas therapy, and PDT, is expected to reverse drug resistance and improve the prognosis of osteosarcoma. Therefore, based on the demonstrated ability of curcumin, metformin, NO, and ROS to reverse drug resistance, these functional agents could be considered for co-loading into 3D-printed bioceramic scaffolds along with conventional chemotherapeutic drugs. In fact, the preparation and loading of functional agents and the loading of conventional chemotherapeutic agents have been well established. It is only necessary to learn from the existing strategies and co-load them into the scaffolds to achieve a superposition of anti-tumor ability. For example, the above-mentioned CaPC scaffolds can kill about 80%–90% of OCs by a single PDT. If a chemotherapeutic drug is also loaded into CaPC scaffolds, the scaffolds may achieve a 100% mortality rate of OCs because the drug can function normally to kill OCs due to drug resistance reversal. Therefore, while retaining the bioactivity of multifunctional scaffolds to promote bone regeneration, the killing ability of residual OCs can be further enhanced for a better prognosis.

For OS metastasis, the process can be divided into three stages, including the escape of OCs from the primary tumor, transit in the circulatory system, and colonization and establishment of metastasis. Therefore, studies have tried to prevent metastasis by targeting circulating tumor cells.[265] For in situ scaffold implantation, instead of directly targeting circulating tumor cells, it is more realistic and suitable to induce long-term anti-tumor immune memory in situ or directly inhibit migration and invasion to prevent metastasis.[266] ROS has demonstrated superior ability in the induction of immunogenic cell death (ICD), a specific type of cell death that induces cell surface expression of pro-apoptotic calcium reticulum protein (CRT), extracellular release of high mobility histone 1 (HMGB1), and secretion of adenosine triphosphate (ATP).[267] Thus, ICD can promote DC maturation and antigen presentation to cytotoxic T cells (CTL) and intra-tumor CTL infiltration.[267,268] However, the "cold" osteosarcoma with immunosuppressive TME, typically characterized by poor immunogenicity and inadequate T cell infiltration, cannot provide sufficient tumor-associated antigens for the immune response of ROS to prevent metastasis effectively.[269] Fortunately, hyperthermia therapy-based tumor ablation frequently displays vaccine-like properties with sufficient tumor-associated antigen production that stimulates anti-tumor immune responses.[270,271] Therefore, combining ROS and photothermal or magnetothermal therapy realizes long-term and strong immune responses to prevent OS metastasis.[271,272] For example, by combing PPT and PDT, a novel H_2O_2 self-generating single-atom nanozyme (SAzyme) hydrogel was developed as a light-controlled oxidative stress amplifier for better synergistic treatment of the primary and metastatic "cold" cancer. The immunotherapeutic effect was improved by promoting DC maturation and CD8 + T cell differentiation and infiltration.[271] In addition, substantial production of ROS can directly inhibit migration and invasion of OCs by down-regulating vitronectin and thrombospondin-1.[266] Therefore, PEGylated carbon nitride nanosheet@copper-doped polyaniline (CNNS@CuPANI) generating massive ROS by combing PDT and CDT can effectively kill OCs and significantly inhibit metastasis.[266] Furthermore, fructose-coated Ångstrom-scale silver particles (f-AgÅPs) can produce substantial ROS, induce mitochondrial

ROS-dependent apoptotic death of OCs, and inhibit OS metastasis. However, the exact mechanism of metastasis inhibition is unclear.[273] Therefore, if these nanoparticles with ideal immune effects by combing ROS with hyperthermia therapy or anti-invasion ability through substantial ROS production can be loaded into a 3D-printed bioceramic scaffold, it may help achieve a better OS prognosis without metastasis.

In addition to drug resistance and metastasis, the low diagnosis rate of primary and metastatic OS lesions with traditional imaging techniques also hinders the prognosis of OS patients. Conventional magnetic resonance imaging (MRI) has high spatial resolution and deep tissue penetration but lacks sensitivity.[274] Some new imaging techniques, such as photoacoustic imaging (PAI), have deep penetration but still low sensitivity. Fluorescence imaging (FI) and Raman imaging have insufficient penetration depth, while FI has high sensitivity and Raman has high resolution. Based on this, multimodal imaging, which combines multiple imaging techniques to achieve complementary advantages, is gradually used for targeted diagnosis of OS and real-time monitoring of the anti-tumor effect.[46] For example, the combination of PAI and FI can clearly depict the edges of in situ OS with good penetration and show more details, including the blood vessels and delicate structures of tumors.[274] Carbon-based nanomaterials show great potential for multimodal imaging in addition to the optical properties for PPT/PDT, high loading capacity for chemotherapy, and osteogenic bioactivity discussed above.[231] CBN has emerged as a novel high-performance single- and two-photon fluorophore for imaging cells by FI, Raman, phosphorescence, and two-photon imaging. CBN was also developed for non-optical imaging modalities, including magnetic resonance, photoacoustic, and computed tomography imaging.[46] CBNs are formed in hybrid or nanocomposite form by incorporating other imaging agents, such as coupling the MR imaging agent $Gd^{3}+$ to carbon dots to form magnetic fluorescent carbon dots[275] or encapsulating $Gd^{3}+$ ions in fullerene cages.[276] This can offset or enhance the optical imaging capacity of the CBN for better theranostic performance. The major problem in the surgical treatment of osteosarcoma is the accurate determination of tumor margins. While over-expansion surgical resection can seriously harm the structure and function of bone tissue, conservative surgical resection can result in recurrence. Therefore, a multifunctional scaffold should be implanted to minimize the resected area and to achieve complete tumor ablation by synergistic anti-tumor therapy. Moreover, evaluating and monitoring the anti-tumor efficacy and determining whether a subsequent surgery is needed is also essential. However, evaluation in the animal model has often taken the form of executing mice after a particular time of treatment, harvesting the tumors, weighing and measuring them, and then producing sections for further observation. Obviously, a safe, non-invasive, accurate, and efficient method is needed to assess efficacy in the clinic. Therefore, 3D multifunctional scaffolds with simultaneous multimodal imaging capability is necessary for further research and clinical translation. Carbon-based nanomaterials' recent excellent multimodal imaging capabilities in various fields have made this vision possible.

In a word, the 3D multifunctional bioceramic scaffolds have shown good performance on anti-tumor and bone regeneration both in vitro and in vivo. However, there have been no reports of its clinical use. We can only say that this 3D multifunctional bioceramic scaffold is a promising therapeutic strategy for the clinical treatment of OS, but some issues should be realized and addressed before its practical application in clinical treatment. First, many studies have focused more on the scaffold's anti-tumor properties and neglected the bone regeneration capacity assessment. Bone defects are a non-negligible problem that seriously affects the life quality of patients. Secondly, lung metastasis is the leading cause of death in OS in the clinic. Existing studies have little awareness of setting OS metastatic model and evaluating OS metastasis, and further studies should increase this awareness to remedy the deficiency. Third, the time to monitor and evaluate the efficacy of in vivo experiments is often only about 8 weeks. Should we extend the time to assess recurrence and metastasis more comprehensively? Fourth, existing evaluation methods are often performed after the execution. Real-time high-precision imaging systems like fBGn should be introduced into multifunctional scaffolds for non-invasive and efficient assessment. Fifth, as a solid tumor in deep tissues, osteosarcoma requires penetration depth when treated with PPT, so a larger model like a canine should be considered to better simulate the process of light penetration into deep human tissues for further evaluation instead of the existing mice model. Sixth, drug resistance is a significant dilemma in the existing clinical treatment of osteosarcoma. However, existing studies of multifunctional scaffolds focus only on the controlled release and the anti-tumor effect of chemotherapy, with little attention to drug resistance. Drug-resistance animal models should be established for in-depth studies in the future. Seventh, the mechanical strength of many existing scaffolds can reach a level close to that of cancelous bone. However, reaching the strength of cortical bone is difficult, thus limiting their application for cortical bone defects. Eighth, widespread clinical application often requires cost and technical accessibility. Therefore, the design of scaffolds with a balance of efficacy and affordability should always be pursued by researchers. In addition, the fabrication process should be manageable. Moreover, the successful clinical translation of 3D multifunctional bioceramic scaffolds also requires further development and popularization of 3D printing technology in various fields of life and further popularizing the concept of personalized precision medicine.

If researchers can notice the above-mentioned problems in further studies, pay attention to them, and address them, then the actual clinical application of 3D-printed multifunctional bioceramic scaffolds to improve the treatment and prognosis of OS is just around the corner.

Acknowledgements

The authors would like to acknowledge that Figures 1 and 2 was created with BioRender.com.

Author Contributions

Conceptualization: Xingran Liu, Yihao Liu, Lei Qiang. *Investigation*: Xingran Liu, Yihao Liu, Lei Qiang, Ren Ya, Yixuan Lin, Han Li, Qiuhan Chen, Shuxin Gao. *Visualization*: Xingran Liu, Yihao Liu, Lei Qiang. *Funding acqusition*: Xingran Liu, Yihao Liu, Lei Qiang, Xue Yang, Changru Zhang, Minjie Fan, Pengfei Zheng, Shuai Li, Jinwu Wang. *Writing – original draft*: Xingran Liu, Yihao Liu, Lei Qiang. *Writing – review & editing*: Xingran Liu, Yihao Liu, Lei Qiang, Yixuan Lin, Pengfei Zheng, Shuai Li, Jinwu Wang.

Declaration of conflicting interests

The author(s) declared no potential conflicts of interest with respect to the research, authorship, and/or publication of this article.

Funding

The author(s) disclosed receipt of the following financial support for the research, authorship, and/or publication of this article: The study was supported by the National Key R&D Program of China (2018YFA0703000), 2022 Lingang laboratory "Seeking Outstanding Youth Program" open project (LG-QS-202206-04), Shanghai Jiao Tong University School of Medicine 15th College Students' Innovative Training Program (1521Y037), Projects funded by the China Postdoctoral Science Foundation (2020TQ0195/2021M702165/2022M722121), Translation Medicine National Key Science and Technology Infrastructure (Shanghai) Open Project (TMSK-2020-118), Jiangsu Provincial Key Research and Development Program (CN) (BE2019608), and Jiangsu Health Commission Medical Research Program (2020158).

ORCID iDs

Shuxin Gao https://orcid.org/0000-0002-2883-7836
Pengfei Zheng https://orcid.org/0000-0002-8647-4818
Jinwu Wang https://orcid.org/0000-0003-1411-057X

References

1. Jafari F, Javdansirat S, Sanaie S, et al. Osteosarcoma: A comprehensive review of management and treatment strategies. *Ann Diagn Pathol* 2020; 49: 151654.
2. Eaton BR, Schwarz R, Vatner R, et al. Osteosarcoma. *Pediatr Blood Cancer* 2021; 68 Suppl 2: e28352.
3. Takenaka S, Tamiya H, Wakamatsu T, et al. Impact of surgical resection and reasons for poor prognosis of pelvic osteosarcoma based on the Bone Tumor Registry in Japan. *Cancers* 2021; 13: 3320.
4. Jing Z, Ni R, Wang J, et al. Practical strategy to construct anti-osteosarcoma bone substitutes by loading cisplatin into 3D-printed titanium alloy implants using a thermosensitive hydrogel. *Bioact Mater* 2021; 6: 4542–4557.
5. Zhang G, Wu Z, Yang Y, et al. A multifunctional antibacterial coating on bone implants for osteosarcoma therapy and enhanced osteointegration. *Chem Eng J* 2022; 428: 131155.
6. Bigham A, Foroughi F, Rezvani Ghomi E, et al. The journey of multifunctional bone scaffolds fabricated from traditional toward modern techniques. *Bio-Design Manuf* 2020; 3: 281–306.
7. Feng C, Zhang K, He R, et al. Additive manufacturing of hydroxyapatite bioceramic scaffolds: Dispersion, digital light processing, sintering, mechanical properties, and biocompatibility. *J Adv Ceram* 2020; 9: 360–373.
8. Wang C, Huang W, Zhou Y, et al. 3D printing of bone tissue engineering scaffolds. *Bioact Mater* 2020; 5: 82–91.
9. Bose S and Tarafder S. Calcium phosphate ceramic systems in growth factor and drug delivery for bone tissue engineering: a review. *Acta Biomater* 2012; 8: 1401–1421.
10. Zhao C, Shen A, Zhang L, et al. Borocarbonitrides nanosheets engineered 3D-printed scaffolds for integrated strategy of osteosarcoma therapy and bone regeneration. *Chem Eng J* 2020; 401: 125989.
11. Wang C, Ye X, Zhao Y, et al. Cryogenic 3D printing of porous scaffolds for in situ delivery of 2D black phosphorus nanosheets, doxorubicin hydrochloride and osteogenic peptide for treating tumor resection-induced bone defects. *Biofabrication* 2020; 12: 035004.
12. Dang W, Jin Y, Yi K, et al. Hemin particles-functionalized 3D printed scaffolds for combined photothermal and chemotherapy of osteosarcoma. *Chem Eng J* 2021; 422: 129919.
13. Ma L, Feng X, Liang H, et al. A novel photothermally controlled multifunctional scaffold for clinical treatment of osteosarcoma and tissue regeneration. *Mater Today* 2020; 36: 48–62.
14. Xiang H, Yang Q, Gao Y, et al. Cocrystal strategy toward multifunctional 3D-Printing scaffolds enables NIR-Activated photonic osteosarcoma hyperthermia and enhanced bone defect regeneration. *Adv Funct Mater* 2020; 30: 1909938.
15. Ma H, Jiang C, Zhai D, et al. A bifunctional biomaterial with photothermal effect for tumor therapy and Bone Regeneration. *Adv Funct Mater* 2016; 26: 1197–1208.
16. Pan S, Yin J, Yu L, et al. 2D mxene-integrated 3D-Printing scaffolds for augmented osteosarcoma phototherapy and accelerated tissue reconstruction. *Adv Sci* 2020; 7: 1901511.
17. Ma H, Ma Z, Chen Q, et al. Bifunctional, copper-doped, mesoporous silica nanosphere-modified, bioceramic scaffolds for bone tumor therapy. *Front Chem* 2020; 8: 610232.
18. Shao H, Jing Z, Xia P, et al. 3D-printed magnesium-doped wollastonite/nano-hydroxyapatite bioceramic scaffolds with high strength and anti-tumor property. *Mater Des* 2023; 225: 111464.
19. He C, Dong C, Hu H, et al. Photosynthetic oxygen-self-generated 3D-printing microbial scaffold enhances osteosarcoma elimination and prompts bone regeneration. *Nano Today* 2021; 41: 101297.
20. Shuai C, Xu Y, Feng P, et al. Antibacterial polymer scaffold based on mesoporous bioactive glass loaded with in situ grown silver. *Chem Eng J* 2019; 374: 304–315.

21. Hu YP, Tian ZF, Zhu M, et al. Controllable preparation and in vitro bioactivity of bioglass microspheres via spray drying method. *J Inorg Mater* 2020; 35: 621–1276.
22. Mirabello L, Troisi RJ and Savage SA. International osteosarcoma incidence patterns in children and adolescents, middle ages and elderly persons. *Int J Cancer* 2009; 125: 229–234.
23. Brown HK, Schiavone K, Gouin F, et al. Biology of bone sarcomas and new therapeutic developments. *Calcif Tissue Int* 2018; 102: 174–195.
24. Mirabello L, Troisi RJ and Savage SA. Osteosarcoma incidence and survival rates from 1973 to 2004: data from the surveillance, epidemiology, and end results program. *Cancer* 2009; 115: 1531–1543.
25. Glass AG and Fraumeni JF Jr. Epidemiology of bone cancer in children. *J Natl Cancer Inst* 1970; 44: 187–199.
26. Beird HC, Bielack SS, Flanagan AM, et al. Osteosarcoma. *Nat Rev Dis Primers* 2022; 8: 77.
27. Isakoff MS, Bielack SS, Meltzer P, et al. Osteosarcoma: current treatment and a collaborative pathway to success. *J Clin Oncol* 2015; 33: 3029–3035.
28. Meltzer PS and Helman LJ. New horizons in the treatment of osteosarcoma. *New Engl J Med* 2021; 385: 2066–2076.
29. Zhou Y, Lu Q, Xu J, et al. The effect of pathological fractures on the prognosis of patients with osteosarcoma: a meta-analysis of 14 studies. *Oncotarget* 2017; 8: 73037–73049.
30. Klein MJ and Siegal GP. Osteosarcoma: anatomic and histologic variants. *Am J Clin Pathol* 2006; 125: 555–581.
31. Piperdi S, Austin-Page L, Geller D, et al. β-Catenin does not confer tumorigenicity when introduced into partially transformed human mesenchymal stem cells. *Sarcoma* 2012; 2012: 164803.
32. Bertoni F and Bacchini P. Classification of bone tumors. *Eur J Radiol* 1998; 27(Suppl 1): S74–S76.
33. Kager L, Zoubek A, Pötschger U, et al. Primary metastatic osteosarcoma: presentation and outcome of patients treated on Neoadjuvant Cooperative Osteosarcoma Study Group Protocols. *J Clin Oncol* 2003; 21: 2011–2018.
34. Rodrigues J, Sarmento B and Pereira CL. Osteosarcoma tumor microenvironment: the key for the successful development of biologically relevant 3D in vitro models. *In Models* 2022; 1: 5–27.
35. Lin Y-H, Jewell BE, Gingold J, et al. Osteosarcoma: Molecular Pathogenesis and iPSC modeling. *Trends Mol Med* 2017; 23: 737–755.
36. Abarrategi A, Tornin J, Martinez-Cruzado L, et al. Osteosarcoma: Cells-of-Origin, cancer stem cells, and targeted therapies. *Stem Cells Int* 2016; 2016: 3631764.
37. Endo-Munoz L, Evdokiou A and Saunders NA. The role of osteoclasts and tumour-associated macrophages in osteosarcoma metastasis. *Biochim Biophys Acta* 2012; 1826: 434–442.
38. Yao M, Zou Q, Zou W, et al. Bifunctional scaffolds of hydroxyapatite/poly(dopamine)/carboxymethyl chitosan with osteogenesis and anti-osteosarcoma effect. *Biomater Sci* 2021; 9: 3319–3333.
39. Gatenby RA and Gillies RJ. Why do cancers have high aerobic glycolysis? *Nat Rev Cancer* 2004; 4: 891–899.
40. Chen Q, Liang C, Sun X, et al. H_2O_2-responsive liposomal nanoprobe for photoacoustic inflammation imaging and tumor theranostics via in vivo chromogenic assay. *Proc Natl Acad Sci* 2017; 114: 5343–5348.
41. Nishikawa M, Tamada A, Kumai H, et al. Inhibition of experimental pulmonary metastasis by controlling biodistribution of catalase in mice. *Int J Cancer* 2002; 99: 474–479.
42. Reynolds TY, Rockwell S and Glazer PM. Genetic instability induced by the tumor microenvironment. *Cancer Res* 1996; 56: 5754–5757.
43. Goubran HA, Kotb RR, Stakiw J, et al. Regulation of tumor growth and metastasis: the role of tumor microenvironment. *Cancer Growth Metastasis* 2014; 7: 9–18.
44. Whiteside TL. The tumor microenvironment and its role in promoting tumor growth. *Oncogene* 2008; 27: 5904–5912.
45. Tang Z, Liu Y, He M, et al. Chemodynamic therapy: tumour microenvironment-mediated Fenton and Fenton-like reactions. *Angew Chem Int Ed* 2019; 58: 946–956.
46. Patel KD, Singh RK and Kim H-W. Carbon-based nanomaterials as an emerging platform for theranostics. *Mater Horiz* 2019; 6: 434–469.
47. Chen B-Q, Kankala RK, Zhang Y, et al. Gambogic acid augments black phosphorus quantum dots (BPQDs)-based synergistic chemo-photothermal therapy through downregulating heat shock protein expression. *Chem Eng J* 2020; 390: 124312.
48. Zakeri N, Rezaie HR, Javadpour J, et al. Cisplatin loaded polycaprolactone – zeolite nanocomposite scaffolds for bone cancer treatment. *J Sci Adv Mater Devices* 2022; 7: 100377.
49. Singh RK, Kurian AG, Patel KD, et al. Label-free fluorescent mesoporous bioglass for drug delivery, optical triple-mode imaging, and photothermal/photodynamic synergistic cancer therapy. *ACS Appl Bio Mater* 2020; 3: 2218–2229.
50. Brown JM and Wilson WR. Exploiting tumour hypoxia in cancer treatment. *Nat Rev Cancer* 2004; 4: 437–447.
51. Kimáková P, Solár P, Fecková B, et al. Photoactivated hypericin increases the expression of SOD-2 and makes MCF-7 cells resistant to photodynamic therapy. *Biomed Pharmacother* 2017; 85: 749–755.
52. Dong S, Chen Y, Yu L, et al. Magnetic hyperthermia–synergistic H_2O_2 self-sufficient catalytic suppression of osteosarcoma with enhanced bone-regeneration bioactivity by 3d-printing composite scaffolds. *Adv Funct Mater* 2020; 30: 1907071.
53. Hattinger CM, Patrizio MP, Fantoni L, et al. Drug resistance in osteosarcoma: emerging biomarkers, therapeutic targets and treatment strategies. *Cancers* 2021; 13: 2878.
54. Yao Z, Han L, Chen Y, et al. Hedgehog signalling in the tumourigenesis and metastasis of osteosarcoma, and its potential value in the clinical therapy of osteosarcoma. *Cell Death Dis* 2018; 9: 701.
55. Kansara M, Teng MW, Smyth MJ, et al. Translational biology of osteosarcoma. *Nat Rev Cancer* 2014; 14: 722–735.
56. Xu C, Wang M, Guo W, et al. Curcumin in osteosarcoma therapy: combining with immunotherapy, chemotherapeutics, bone tissue engineering materials and potential synergism with photodynamic therapy. *Front Oncol* 2021; 11: 672490.
57. Woodard JR, Hilldore AJ, Lan SK, et al. The mechanical properties and osteoconductivity of hydroxyapatite bone scaffolds with multi-scale porosity. *Biomaterials* 2007; 28: 45–54.

58. Butscher A, Bohner M, Hofmann S, et al. Structural and material approaches to bone tissue engineering in powder-based three-dimensional printing. *Acta Biomater* 2011; 7: 907–920.
59. Li X, Cui R, Sun L, et al. 3D-Printed biopolymers for tissue engineering application. *Int J Polym Sci* 2014; 2014: 1–13.
60. Lee J and Cho D-W. 3D printing technology over a drug delivery for tissue engineering. *Curr Pharm Des* 2015; 21: 1606–1617.
61. Ma H, Feng C, Chang J, et al. 3D-printed bioceramic scaffolds: from bone tissue engineering to tumor therapy. *Acta Biomater* 2018; 79: 37–59.
62. Yves-Christian H, Jan W, Wilhelm M, et al. Net shaped high performance oxide ceramic parts by selective laser melting. *Phys Procedia* 2010; 5: 587–594.
63. Pham DT and Gault RS. A comparison of rapid prototyping technologies. *Int J Mach Tools Manuf* 1998; 38: 1257–1287.
64. Tian T, Wu C and Chang J. Preparation and in vitro osteogenic, angiogenic and antibacterial properties of cuprorivaite (CaCuSi4O10, cup) bioceramics. *RSC Adv* 2016; 6: 45840–45849.
65. Cui J, Ma C, Li Z, et al. Polydopamine-functionalized polymer particles as templates for mineralization of hydroxyapatite: biomimetic and in vitro bioactivity. *RSC Adv* 2016; 6: 6747–6755.
66. Bohner M, Galea L and Doebelin N. Calcium phosphate bone graft substitutes: failures and hopes. *J Eur Ceram Soc* 2012; 32: 2663–2671.
67. Babilotte J, Martin B, Guduric V, et al. Development and characterization of a PLGA-HA composite material to fabricate 3D-printed scaffolds for bone tissue engineering. *Mater Sci Eng C* 2021; 118: 111334.
68. Tian L, Zhang Z, Tian B, et al. Study on antibacterial properties and cytocompatibility of EPL coated 3D printed PCL/HA composite scaffolds. *RSC Adv* 2020; 10: 4805–4816.
69. Tan W, Gao C, Feng P, et al. Dual-functional scaffolds of poly(L-lactic acid)/nanohydroxyapatite encapsulated with metformin: simultaneous enhancement of bone repair and bone tumor inhibition. *Mater Sci Eng C* 2021; 120: 111592.
70. Albanese A, Tang PS and Chan WC. The effect of nanoparticle size, shape, and surface chemistry on biological systems. *Annu Rev Biomed Eng* 2012; 14(1): 1–16.
71. Oberbek P, Bolek T, Chlanda A, et al. Characterization and influence of hydroxyapatite nanopowders on living cells. *Beilstein J Nanotechnol* 2018; 9: 3079–3094.
72. Zhou H and Lee J. Nanoscale hydroxyapatite particles for bone tissue engineering. *Acta Biomater* 2011; 7: 2769–2781.
73. Wu C and Chang J. Degradation, bioactivity, and cytocompatibility of diopside, akermanite, and bredigite ceramics. *J Biomed Mater Res Part B Appl Biomater* 2007; 83: 153–160.
74. Kokubo T. Bioactive glass ceramics: properties and applications. *Biomaterials* 1991; 12: 155–163.
75. Wu C and Chang J. Synthesis and apatite-formation ability of akermanite. *Mater Lett* 2004; 58: 2415–2417.
76. Sun H, Wu C, Dai K, et al. Proliferation and osteoblastic differentiation of human bone marrow-derived stromal cells on akermanite-bioactive ceramics. *Biomaterials* 2006; 27: 5651–5657.
77. Huang Y, Jin X, Zhang X, et al. In vitro and in vivo evaluation of akermanite bioceramics for bone regeneration. *Biomaterials* 2009; 30: 5041–5048.
78. Liu Q, Cen L, Yin S, et al. A comparative study of proliferation and osteogenic differentiation of adipose-derived stem cells on akermanite and beta-TCP ceramics. *Biomaterials* 2008; 29: 4792–4799.
79. Sahin YM, Orman Z and Yucel S. In vitro studies of α-TCP and β-TCP produced from Clinocardium ciliatum seashells. *J Aust Ceram Soc* 2020; 56: 477–488.
80. Gondim ALMF, Barbosa GAS, Dantas WRM, et al. Efeito da laserterapia na osteogênese em defeitos de calota craniana preenchidos com cimento de α-TCP e grânulos de β-TCP/HA: modelo animal. *Res Soc Dev* 2020; 9: e6889109061.
81. Eliaz N and Metoki N. Calcium phosphate bioceramics: a review of their history, structure, properties, coating technologies and biomedical applications. *Materials* 2017; 10: 334.
82. Hench LL. Bioceramics: from concept to clinic. *J Am Ceram Soc* 1991; 74: 1487–1510.
83. Kato K, Ochiai S, Yamamoto A, et al. Novel multilayer Ti foam with cortical bone strength and cytocompatibility. *Acta Biomater* 2013; 9: 5802–5809.
84. Dang W, Yi K, Ju E, et al. 3D printed bioceramic scaffolds as a universal therapeutic platform for synergistic therapy of osteosarcoma. *ACS Appl Mater Interfaces* 2021; 13: 18488–18499.
85. Wang X, Zhang L, Ke X, et al. 45S5 bioglass analogue reinforced akermanite ceramic favorable for additive manufacturing mechanically strong scaffolds. *RSC Adv* 2015; 5: 102727–102735.
86. Rainer A, Giannitelli SM, Abbruzzese F, et al. Fabrication of bioactive glass-ceramic foams mimicking human bone portions for regenerative medicine. *Acta Biomater* 2008; 4: 362–369.
87. Hench LL. Opening paper 2015- some comments on Bioglass: four eras of discovery and Development. *Biomed Glass* 2015; 1: 1–11.
88. Leach JK, Kaigler D, Wang Z, et al. Coating of VEGF-releasing scaffolds with bioactive glass for angiogenesis and bone regeneration. *Biomaterials* 2006; 27: 3249–3255.
89. Kokubo T and Takadama H. How useful is SBF in predicting in vivo bone bioactivity? *Biomaterials* 2006; 27: 2907–2915.
90. Rizwan M, Hamdi M and Basirun WJ. Bioglass® 45S5-based composites for bone tissue engineering and functional applications. *J Biomed Mater Res A* 2017; 105: 3197–3223.
91. Wang X, Li T, Ma H, et al. A 3D-printed scaffold with MoS2 nanosheets for tumor therapy and tissue regeneration. *NPG Asia Mater* 2017; 9: e376–e376.
92. Zhuang H, Lin R, Liu Y, et al. Three-dimensional-printed bioceramic scaffolds with osteogenic activity for simultaneous photo/magnetothermal therapy of bone tumors. *ACS Biomater Sci Eng* 2019; 5: 6725–6734.
93. Zhuang H, Qin C, Zhang M, et al. 3D-printed bioceramic scaffolds with Fe3S4microflowers for magnetothermal and chemodynamic therapy of bone tumor and regeneration of bone defects. *Biofabrication* 2021; 13: 20210813.
94. Dang W, Ma B, Li B, et al. 3D printing of metal-organic framework nanosheets-structured scaffolds with tumor therapy and bone construction. *Biofabrication* 2020; 12: 025005.
95. Zhang Y, Zhai D, Xu M, et al. 3D-printed bioceramic scaffolds with a Fe_3O_4/graphene oxide nanocomposite interface

for hyperthermia therapy of bone tumor cells. *J Mater Chem B* 2016; 4: 2874–2886.
96. Zhang X, Wei H, Dong C, et al. 3D printed hydrogel/bioceramics core/shell scaffold with NIR-II triggered drug release for chemo-photothermal therapy of bone tumors and enhanced bone repair. *Chem Eng J* 2023; 461: 141855.
97. Sarkar N and Bose S. Liposome-encapsulated curcumin-loaded 3D printed scaffold for bone tissue engineering. *ACS Appl Mater Interfaces* 2019; 11: 17184–17192.
98. Dang W, Ma B, Huan Z, et al. LaB6 surface chemistry-reinforced scaffolds for treating bone tumors and bone defects. *Appl Mater Today* 2019; 16: 42–55.
99. Dang W, Li T, Li B, et al. A bifunctional scaffold with CuFeSe2 nanocrystals for tumor therapy and bone reconstruction. *Biomaterials* 2018; 160: 92–106.
100. Liu Y, Li T, Ma H, et al. 3D-printed scaffolds with bioactive elements-induced photothermal effect for bone tumor therapy. *Acta Biomater* 2018; 73: 531–546.
101. Yang Q, Yin H, Xu T, et al. Engineering 2D mesoporous silica@mxene-integrated 3D-printing scaffolds for combinatory osteosarcoma therapy and NO-augmented bone regeneration. *Small* 2020; 16: e1906814.
102. Wang L, Yang Q, Huo M, et al. Engineering single-atomic iron-catalyst-integrated 3D-printed bioscaffolds for osteosarcoma destruction with antibacterial and bone defect regeneration bioactivity. *Adv Mater Weinheim* 2021; 33: e2100150.
103. Hench LL. The story of bioglass. *J Mater Sci Mater Med* 2006; 17: 967–978.
104. Yin J, Pan S, Guo X, et al. Nb(2)C MXene-Functionalized scaffolds enables osteosarcoma phototherapy and angiogenesis/osteogenesis of bone defects. *Nano-Micro Lett* 2021; 13: 30–18.
105. Yang Z, Yu S, Li D, et al. The effect of PLGA-based hydrogel scaffold for improving the drug maximum-tolerated dose for in situ osteosarcoma treatment. *Colloids Surf B Biointerfaces* 2018; 172: 387–394.
106. Farzin A, Etesami SA, Goodarzi A, et al. A facile way for development of three-dimensional localized drug delivery system for bone tissue engineering. *Mater Sci Eng C Mater Biol Appl* 2019; 105: 110032.
107. Kwiatkowski S, Knap B, Przystupski D, et al. Photodynamic therapy – mechanisms, photosensitizers and combinations. *Biomed Pharmacother* 2018; 106: 1098–1107.
108. Wang YY, Liu YC, Sun H, et al. Type I photodynamic therapy by organic–inorganic hybrid materials: from strategies to applications. *Coord Chem Rev* 2019; 395: 46–62.
109. Li M, Xia J, Tian R, et al. Near-infrared light-initiated molecular superoxide radical generator: rejuvenating photodynamic therapy against hypoxic tumors. *J Am Chem Soc* 2018; 140: 14851–14859.
110. Zhang X, Tian G, Yin W, et al. Controllable generation of nitric oxide by near-infrared-sensitized upconversion nanoparticles for tumor therapy. *Adv Funct Mater* 2015; 25: 3049–3056.
111. Xu W, Tamarov K, Fan L, et al. Scalable synthesis of biodegradable black mesoporous silicon nanoparticles for highly efficient photothermal therapy. *ACS Appl Mater Interfaces* 2018; 10: 23529–23538.
112. Zhou B, Zhao J, Qiao Y, et al. Simultaneous multimodal imaging and photothermal therapy via renal-clearable manganese-doped copper sulfide nanodots. *Appl Mater Today* 2018; 13: 285–297.
113. Liu Y, Bhattarai P, Dai Z, et al. Photothermal therapy and photoacoustic imaging via nanotheranostics in fighting cancer. *Chem Soc Rev* 2019; 48: 2053–2108.
114. Kumar CS and Mohammad F. Magnetic nanomaterials for hyperthermia-based therapy and controlled drug delivery. *Adv Drug Deliv Rev* 2011; 63: 789–808.
115. Jaque D, Martínez Maestro L, del Rosal B, et al. Nanoparticles for photothermal therapies. *Nanoscale* 2014; 6: 9494–9530.
116. Ma HN, Jin M, Zhu T-T, et al. Effect of dietary arachidonic acid levels on growth performance, fatty acid profiles and lipid metabolism of juvenile yellow catfish (Pelteobagrus fulvidraco). *Aquaculture* 2018; 486: 31–41.
117. Ma H, Luo J, Sun Z, et al. 3D printing of biomaterials with mussel-inspired nanostructures for tumor therapy and tissue regeneration. *Biomaterials* 2016; 111: 138–148.
118. Deng X, Liang H, Yang W, et al. Polarization and function of tumor-associated macrophages mediate graphene oxide-induced photothermal cancer therapy. *J Photochem Photobiol B* 2020; 208: 111913.
119. Ma H, Li T, Huan Z, et al. 3D printing of high-strength bioscaffolds for the synergistic treatment of bone cancer. *NPG Asia Mater* 2018; 10: 31–44.
120. Zhu L, Gao M, Peh CKN, et al. Solar-driven photothermal nanostructured materials designs and prerequisites for evaporation and catalysis applications. *Mater Horiz* 2018; 5: 323–343.
121. Miao H, Shen R, Zhang W, et al. Near-Infrared light triggered silk fibroin scaffold for photothermal therapy and tissue repair of bone tumors. *Adv Funct Mater* 2021; 31: 2007188.
122. Xu D, Li Z, Li L, et al. Insights into the photothermal conversion of 2D mxene nanomaterials: synthesis, mechanism, and Applications. *Adv Funct Mater* 2020; 30: 2000712.
123. Zou Q, Abbas M, Zhao L, et al. Biological Photothermal nanodots based on self-assembly of peptide-porphyrin conjugates for antitumor therapy. *J Am Chem Soc* 2017; 139: 1921–1927.
124. Gao M, Zhu L, Peh CK, et al. Solar absorber material and system designs for photothermal water vaporization towards clean water and energy production. *Energy Environ Sci* 2019; 12: 841–864.
125. Wang J, Li Y, Deng L, et al. High-performance photothermal conversion of narrow-bandgap Ti2 O3 nanoparticles. *Adv Mater* 2017; 29: 20161111.
126. Zijlstra P, Paulo PMR and Orrit M. Optical detection of single non-absorbing molecules using the surface plasmon resonance of a gold nanorod. *Nat Nanotechnol* 2012; 7: 379–382.
127. Wang C and Astruc D. Nanogold plasmonic photocatalysis for organic synthesis and clean energy conversion. *Chem Soc Rev* 2014; 43: 7188–7216.
128. Liu X, Cao J, Li H, et al. Mussel-inspired polydopamine: a biocompatible and ultrastable coating for nanoparticles in vivo. *ACS Nano* 2013; 7: 9384–9395.
129. Liu Y, Ai K, Liu J, et al. Dopamine-melanin colloidal nanospheres: an efficient near-infrared photothermal therapeutic agent for in vivo cancer therapy. *Adv Mater* 2013; 25: 1353–1359.

130. Cheng W, Zeng X, Chen H, et al. Versatile polydopamine platforms: synthesis and promising applications for surface modification and advanced nanomedicine. *ACS Nano* 2019; 13: 8537–8565.
131. Soenen SJ, Rivera-Gil P, Montenegro JM, et al. Cellular toxicity of inorganic nanoparticles: common aspects and guidelines for improved nanotoxicity evaluation. *Nano Today* 2011; 6: 446–465.
132. Kostarelos K. The long and short of carbon nanotube toxicity. *Nat Biotechnol* 2008; 26: 774–776.
133. Song Q, Jiao Y, Wang Z, et al. Tuning the energy gap by supramolecular approaches: towards near-infrared organic assemblies and Materials. *Small* 2016; 12: 24–31.
134. Yang L, Guo X, Jin Z, et al. Emergence of melanin-inspired supercapacitors. *Nano Today* 2021; 37: 101075.
135. Sheng Z, Hu D, Zheng M, et al. Smart human serum albumin-indocyanine green nanoparticles generated by programmed assembly for dual-modal imaging-guided cancer synergistic phototherapy. *ACS Nano* 2014; 8: 12310–12322.
136. Jiang B, Zhang L, Zhu Y, et al. Water-soluble hyaluronic acid-hybridized polyaniline nanoparticles for effectively targeted photothermal therapy. *J Mater Chem B* 2015; 3: 3767–3776.
137. Ulasevich S, Ryzhkov NV, Andreeva DV, et al. Light-to-heat photothermal dynamic properties of polypyrrole-based coating for regenerative therapy and lab-on-a-chip applications. *Adv Mater Interfaces* 2020; 7: 2000980.
138. Geng H, Zhu L, Yi Y, et al. Superexchange induced charge transport in organic donor–acceptor cocrystals and copolymers: a theoretical perspective. *Chem Mater* 2019; 31: 6424–6434.
139. Wang Y, Zhu W, Du W, et al. Cocrystals strategy towards materials for near-infrared photothermal conversion and imaging. *Angew Chem Int Ed Engl* 2018; 57: 3963–3967.
140. Shinada NK, de Brevern AG and Schmidtke P. Halogens in protein-ligand binding mechanism: a structural perspective. *J Med Chem* 2019; 62: 9341–9356.
141. Zhang R, Rejeeth C, Xu W, et al. Label-free electrochemical sensor for CD44 by ligand-protein interaction. *Anal Chem* 2019; 91: 7078–7085.
142. Gao P, Xiao Y, YuliangWang, et al. Biomedical applications of 2D monoelemental materials formed by group VA and VIA: a concise review. *J. Nanobiotechnol* 2021; 19: 96.
143. Yang K, Gong H, Shi X, et al. In vivo biodistribution and toxicology of functionalized nano-graphene oxide in mice after oral and intraperitoneal administration. *Biomaterials* 2013; 34: 2787–2795.
144. Wang Y, Wang H, Liu D, et al. Graphene oxide covalently grafted upconversion nanoparticles for combined NIR mediated imaging and photothermal/photodynamic cancer therapy. *Biomaterials* 2013; 34: 7715–7724.
145. Shi X, Gong H, Li Y, et al. Graphene-based magnetic plasmonic nanocomposite for dual bioimaging and photothermal therapy. *Biomaterials* 2013; 34: 4786–4793.
146. Lee WC, Lim CH, Shi H, et al. Origin of enhanced stem cell growth and differentiation on graphene and graphene oxide. *ACS Nano* 2011; 5: 7334–7341.
147. Zhang Y, Nayak TR, Hong H, et al. Graphene: a versatile nanoplatform for biomedical applications. *Nanoscale* 2012; 4: 3833–3842.
148. Chong Y, Ma Y, Shen H, et al. The in vitro and in vivo toxicity of graphene quantum dots. *Biomaterials* 2014; 35: 5041–5048.
149. Park EJ, Lee GH, Han BS, et al. Toxic response of graphene nanoplatelets in vivo and in vitro. *Arch Toxicol* 2015; 89: 1557–1568.
150. Sasidharan A, Panchakarla LS, Sadanandan AR, et al. Hemocompatibility and macrophage response of pristine and functionalized graphene. *Small* 2012; 8: 1251–1263.
151. Robinson JT, Tabakman SM, Liang Y, et al. Ultrasmall reduced graphene oxide with high near-infrared absorbance for photothermal therapy. *J Am Chem Soc* 2011; 133: 6825–6831.
152. Huang P, Wang S, Wang X, et al. Surface functionalization of chemically reduced graphene oxide for targeted photodynamic therapy. *J Biomed Nanotechnol* 2015; 11: 117–125.
153. Huang Z, Xu J, Chen J, et al. Photoacoustic stimulation promotes the osteogenic differentiation of bone mesenchymal stem cells to enhance the repair of bone defect. *Sci Rep* 2017; 7: 15842.
154. Kim J, Park S, Kim YJ, et al. Monolayer graphene-directed growth and neuronal differentiation of mesenchymal stem cells. *J Biomed Nanotechnol* 2015; 11: 2024–2033.
155. Li D, Nie W, Chen L, et al. Self-assembled hydroxyapatite-graphene scaffold for photothermal cancer therapy and Bone Regeneration. *J Biomed Nanotechnol* 2018; 14: 2003–2017.
156. kumar N, Moses K, Pramoda K, et al. Borocarbonitrides, bxcynz. *J Mater Chem A* 2013; 1: 5806–5821.
157. Hoppe A, Güldal NS and Boccaccini AR. A review of the biological response to ionic dissolution products from bioactive glasses and glass-ceramics. *Biomaterials* 2011; 32: 2757–2774.
158. Dollwet HH and Sorenson JR. Roles of copper in bone maintenance and healing. *Biol Trace Elem Res* 1988; 18: 39–48.
159. Shi M, Chen Z, Farnaghi S, et al. Copper-doped mesoporous silica nanospheres, a promising immunomodulatory agent for inducing osteogenesis. *Acta Biomater* 2016; 30: 334–344.
160. Manzeli S, Ovchinnikov D, Pasquier D, et al. 2D transition metal dichalcogenides. *Nat Rev Mater* 2017; 2: 1–15.
161. Xu S, Zheng H, Ma R, et al. Vacancies on 2D transition metal dichalcogenides elicit ferroptotic cell death. *Nat Commun* 2020; 11: 3484.
162. Li B, Wang X, Chen L, et al. Ultrathin Cu-TCPP MOF nanosheets: a new theragnostic nanoplatform with magnetic resonance/near-infrared thermal imaging for synergistic phototherapy of cancers. *Theranostics* 2018; 8: 4086–4096.
163. Sun J, Pang K, Liu TF, et al. Near-infrared photothermal performance of a metal-organic framework-based composite. *Dalton Trans* 2021; 50: 17499–17505.
164. Chu Y, Hou J, Boyer C, et al. Biomimetic synthesis of coordination network materials: recent advances in MOFs and MPNs. *Appl Mater Today* 2018; 10: 93–105.
165. Zhang Y, Wang L, Liu L, et al. Engineering metal-organic frameworks for photoacoustic imaging-guided chemo-/photothermal combinational tumor therapy. *ACS Appl Mater Interfaces* 2018; 10: 41035–41045.

166. Yang J, Xiong L, Li M, et al. Preparation and characterization of tadpole- and sphere-shaped hemin nanoparticles for enhanced solubility. *Nanoscale Res Lett* 2019; 14: 47.
167. Zou HL, Li BL, Luo HQ, et al. A novel electrochemical biosensor based on hemin functionalized graphene oxide sheets for simultaneous determination of ascorbic acid, dopamine and uric acid. *Sens Actuators B* 2015; 207: 535–541.
168. Song C, Wang Z, Yin Z, et al. Principles and applications of photothermal catalysis. *Chem Catal* 2022; 2: 52–83.
169. Pan Y, Huang K, Li Y, et al. Mesoporous porphyrinic metal-organic framework nanoparticles/3D nanofibrous scaffold as a versatile platform for bone tumor therapy. *Mater Today Chem* 2022; 24: 100829.
170. Lu HT, Huang GY, Chang WJ, et al. Modification of chitosan nanofibers with CuS and fucoidan for antibacterial and bone tissue engineering applications. *Carbohydr Polym* 2022; 281: 119035.
171. Argueta-Figueroa L, Martínez-Alvarez O, Santos-Cruz J, et al. Nanomaterials made of non-toxic metallic sulfides: A systematic review of their potential biomedical applications. *Mater Sci Eng C Mater Biol Appl* 2017; 76: 1305–1315.
172. Zhang S, Sun C, Zeng J, et al. Ambient aqueous synthesis of ultrasmall pegylated $Cu_{2-x}Se$ nanoparticles as a multifunctional theranostic agent for multimodal imaging guided photothermal therapy of cancer. *Adv Mater* 2016; 28: 8927–8936.
173. Chou SS, Kaehr B, Kim J, et al. Chemically exfoliated MoS2 as near-infrared photothermal agents. *Angew Chem Int Ed Engl* 2013; 52: 4160–4164.
174. Wu C, Zhou Y, Fan W, et al. Hypoxia-mimicking mesoporous bioactive glass scaffolds with controllable cobalt ion release for bone tissue engineering. *Biomaterials* 2012; 33: 2076–2085.
175. Huang K, Li C, Li H, et al. Photocatalytic applications of two-dimensional Ti3C2 MXenes: a review. *ACS Appl Nano Mater* 2020; 3: 9581–9603.
176. Li R, Zhang L, Shi L, et al. MXene Ti3C2: an effective 2D light-to-heat conversion material. *ACS Nano* 2017; 11: 3752–3759.
177. Mi X, Su Z, Fu Y, et al. 3D printing of Ti3C2-mxene-incorporated composite scaffolds for accelerated bone regeneration. *Biomed Mater* 2022; 17: 20220401.
178. Lin H, Gao S, Dai C, et al. A Two-Dimensional biodegradable niobium carbide (mxene) for photothermal tumor eradication in NIR-I and NIR-II biowindows. *J Am Chem Soc* 2017; 139: 16235–16247.
179. Han X, Jing X, Yang D, et al. Therapeutic mesopore construction on 2D Nb2C mxenes for targeted and enhanced chemo-photothermal cancer therapy in NIR-II biowindow. *Theranostics* 2018; 8: 4491–4508.
180. Liao J, Shi K, Jia Y, et al. Gold nanorods and nanohydroxyapatite hybrid hydrogel for preventing bone tumor recurrence via postoperative photothermal therapy and bone regeneration promotion. *Bioact Mater* 2021; 6: 2221–2230.
181. Chen C-J and Chen D-H. Preparation of LaB6 nanoparticles as a novel and effective near-infrared photothermal conversion material. *Chem Eng J* 2012; 180: 337–342.
182. Weekes DM, Cawthray JF, Rieder M, et al. La(iii) biodistribution profiles from intravenous and oral dosing of two lanthanum complexes, la(dpp)3 and La(XT), and evaluation as treatments for bone resorption disorders. *Metallomics* 2017; 9: 902–909.
183. Zhang K, Feng Y, Wang F, et al. Two dimensional hexagonal boron nitride (2D-hbn): synthesis, properties and applications. *J Mater Chem C* 2017; 5: 11992–12022.
184. Qiu M, Ren WX, Jeong T, et al. Omnipotent phosphorene: a next-generation, two-dimensional nanoplatform for multidisciplinary biomedical applications. *Chem Soc Rev* 2018; 47: 5588–5601.
185. Zhang Y, Xia W, Wu Y, et al. Prediction of mxene based 2D tunable band gap semiconductors: GW quasiparticle calculations. *Nanoscale* 2019; 11: 3993–4000.
186. Zhou Y, Zhang M, Guo Z, et al. Recent advances in black phosphorus-based photonics, electronics, sensors and energy devices. *Mater Horiz* 2017; 4: 997–1019.
187. Lei W, Liu G, Zhang J, et al. Black phosphorus nanostructures: recent advances in hybridization, doping and functionalization. *Chem Soc Rev* 2017; 46: 3492–3509.
188. Fei R and Yang L. Strain-engineering the anisotropic electrical conductance of few-layer black phosphorus. *Nano Lett* 2014; 14: 2884–2889.
189. Tao W, Zhu X, Yu X, et al. Black phosphorus nanosheets as a robust delivery platform for cancer theranostics. *Adv Mater* 2017; 29: 20161031.
190. Yang B, Yin J, Chen Y, et al. 2D-black-phosphorus-reinforced 3D-printed scaffolds: a stepwise countermeasure for osteosarcoma. *Adv Mater* 2018; 30: 20180115.
191. Liu C, Yao W, Tian M, et al. Mussel-inspired degradable antibacterial polydopamine/silica nanoparticle for rapid hemostasis. *Biomaterials* 2018; 179: 83–95.
192. Lee JH, Jang JT, Choi JS, et al. Exchange-coupled magnetic nanoparticles for efficient heat induction. *Nat Nanotechnol* 2011; 6: 418–422.
193. Hilger I and Kaiser WA. Iron oxide-based nanostructures for MRI and magnetic hyperthermia. *Nanomedicine* 2012; 7: 1443–1459.
194. Guardia P, Di Corato R, Lartigue L, et al. Water-soluble iron oxide nanocubes with high values of specific absorption rate for cancer cell hyperthermia treatment. *ACS Nano* 2012; 6: 3080–3091.
195. Blanco-Andujar C, Walter A, Cotin G, et al. Design of iron oxide-based nanoparticles for MRI and magnetic hyperthermia. *Nanomedicine* 2016; 11: 1889–1910.
196. Nikazar S, Barani M, Rahdar A, et al. Photo- and magnetothermally responsive nanomaterials for therapy, controlled drug delivery and imaging applications. *ChemistrySelect* 2020; 5: 12590–12609.
197. Li K, Yan T, Xue Y, et al. Intrinsically ferromagnetic Fe-doped TiO2 coatings on titanium for accelerating osteoblast response in vitro. *J Mater Chem B* 2018; 6: 5756–5767.
198. Kang K, Kim H, Choi E, et al. Electro-magnetic interference shielding effect of electrospun carbon nanofiber web containing BaTiO3 and Fe3O4 nanoparticles. *J Nanosci Nanotechnol* 2017; 17: 7689–7694.
199. Wang X, Zhong X, Liu Z, et al. Recent progress of chemodynamic therapy-induced combination cancer therapy. *Nano Today* 2020; 35: 100946.
200. Wahajuddin and Arora S. Superparamagnetic iron oxide nanoparticles: magnetic nanoplatforms as drug carriers. *Int J Nanomedicine* 2012; 7: 3445–3471.

201. Kesse X, Adam A, Begin-Colin S, et al. Elaboration of superparamagnetic and bioactive multicore-shell nanoparticles (γ-Fe(2)O(3)@sio(2)-cao): A promising material for bone cancer treatment. *ACS Appl Mater Interfaces* 2020; 12: 47820–47830.
202. Bigham A, Aghajanian AH, Allahdaneh S, et al. Multifunctional mesoporous magnetic Mg2SiO4–CuFe2O4 core-shell nanocomposite for simultaneous bone cancer therapy and regeneration. *Ceram Int* 2019; 45: 19481–19488.
203. Heck RK Jr., Peabody TD and Simon MA. Staging of primary malignancies of bone. *CA Cancer J Clin* 2006; 56: 366–375.
204. Muller PY and Milton MN. The determination and interpretation of the therapeutic index in drug development. *Nat Rev Drug Discov* 2012; 11: 751–761.
205. Sooriyaarachchi M, George GN, Pickering IJ, et al. Tuning the metabolism of the anticancer drug cisplatin with chemoprotective agents to improve its safety and efficacy. *Metallomics* 2016; 8: 1170–1176.
206. Son JS, Appleford M, Ong JL, et al. Porous hydroxyapatite scaffold with three-dimensional localized drug delivery system using biodegradable microspheres. *J Control Release* 2011; 153: 133–140.
207. Wang Z, Wang Z, Lu WW, et al. Novel biomaterial strategies for controlled growth factor delivery for biomedical applications. *NPG Asia Mater* 2017; 9: e435–e435.
208. Alenezi A, Chrcanovic B and Wennerberg A. Effects of local drug and chemical compound delivery on bone regeneration around dental implants in animal models: a systematic review and meta-analysis. *Int J Oral Maxillofac Implants* 2018; 33: e1–e18.
209. Chu X, Zhang L, Li Y, et al. NIR responsive doxorubicin-Loaded Hollow copper Ferrite @ polydopamine for synergistic chemodynamic/photothermal/chemo-therapy. *Small* 2023; 19: e2205414.
210. He M, Zhu C, Sun D, et al. Layer-by-layer assembled black phosphorus/chitosan composite coating for multi-functional PEEK bone scaffold. *Compos B Eng* 2022; 246: 110266.
211. Li Y, Hou H, Zhang P, et al. Co-delivery of doxorubicin and paclitaxel by reduction/pH dual responsive nanocarriers for osteosarcoma therapy. *Drug Deliv* 2020; 27: 1044–1053.
212. Wang Z, Zhang K, Zhu Y, et al. Curcumin inhibits hypoxia-induced proliferation and invasion of MG-63 osteosarcoma cells via downregulating Notch1. *Mol Med Rep* 2017; 15: 1747–1752.
213. Chen P, Wang H, Yang F, et al. Curcumin promotes osteosarcoma cell death by activating miR-125a/ERRα signal pathway. *J Cell Biochem* 2017; 118: 74–81.
214. Sarkar N and Bose S. Controlled delivery of curcumin and vitamin K2 from hydroxyapatite-coated titanium implant for enhanced in vitro chemoprevention, osteogenesis, and in vivo osseointegration. *ACS Appl Mater Interfaces* 2020; 12: 13644–13656.
215. Smieszek A, Tomaszewski KA, Kornicka K, et al. Metformin promotes osteogenic differentiation of adipose-derived stromal cells and exerts Pro-Osteogenic effect stimulating bone regeneration. *J Clin Med* 2018; 7: 482.
216. Meng Z, Liu Y, Xu K, et al. Biomimetic polydopamine-modified silk fibroin/curcumin nanofibrous scaffolds for Chemo-photothermal therapy of bone tumor. *ACS Omega* 2021; 6: 22213–22223.
217. Hu J, Wu W, Qin Y, et al. Fabrication of Glyco-metal-organic frameworks for targeted interventional photodynamic/chemotherapy for hepatocellular carcinoma through percutaneous transperitoneal puncture. *Adv Funct Mater* 2020; 30: 1910084.
218. Dougherty TJ, Gomer CJ, Henderson BW, et al. Photodynamic therapy. *J Natl Cancer Inst* 1998; 90: 889–905.
219. Mao D, Hu F, Yi Z, et al. AIEgen-coupled upconversion nanoparticles eradicate solid tumors through dual-mode ROS activation. *Sci Adv* 2020; 6: eabb2712.
220. Kamkaew A, Lim SH, Lee HB, et al. BODIPY dyes in photodynamic therapy. *Chem Soc Rev* 2013; 42: 77–88.
221. Plaetzer K, Krammer B, Berlanda J, et al. Photophysics and photochemistry of photodynamic therapy: fundamental aspects. *Lasers Med Sci* 2009; 24: 259–268.
222. Hong G, Diao S, Chang J, et al. Through-skull fluorescence imaging of the brain in a new near-infrared window. *Nat Photonics* 2014; 8: 723–730.
223. Zhou T-J, Xing L, Fan Y-T, et al. Light triggered oxygen-affording engines for repeated hypoxia-resistant photodynamic therapy. *J Control Release* 2019; 307: 44–54.
224. Broekgaarden M, Weijer R, van Gulik TM, et al. Tumor cell survival pathways activated by photodynamic therapy: a molecular basis for pharmacological inhibition strategies. *Cancer Metastasis Rev* 2015; 34: 643–690.
225. Vaupel P and Mayer A. Hypoxia in cancer: significance and impact on clinical outcome. *Cancer Metastasis Rev* 2007; 26: 225–239.
226. Rankin EB and Giaccia AJ. Hypoxic control of metastasis. *Science* 2016; 352: 175–180.
227. Sharma SK, Chiang LY and Hamblin MR. Photodynamic therapy with fullerenes in vivo: reality or a dream? *Nanomed* 2011; 6: 1813–1825.
228. Ikeda A, Akiyama M, Ogawa T, et al. Photodynamic activity of liposomal photosensitizers via energy transfer from antenna molecules to [60]fullerene. *ACS Med Chem Lett* 2010; 1: 115–119.
229. Guo T, Wu Y, Lin Y, et al. Black phosphorus quantum dots with renal clearance property for efficient photodynamic therapy. *Small* 2018; 14: 1702815.
230. Li Q, Hong L, Li H, et al. Graphene oxide-fullerene C60 (GO-C60) hybrid for photodynamic and photothermal therapy triggered by near-infrared light. *Biosens Bioelectron* 2017; 89: 477–482.
231. Lu Y, Li L, Li M, et al. Zero-dimensional carbon dots enhance bone regeneration, osteosarcoma ablation, and clinical bacterial eradication. *Bioconjug Chem* 2018; 29: 2982–2993.
232. Cha C, Shin SR, Annabi N, et al. Carbon-based nanomaterials: multifunctional materials for biomedical engineering. *ACS Nano* 2013; 7: 2891–2897.
233. Kim J, Cho HR, Jeon H, et al. Continuous O2-evolving MnFe2O4 nanoparticle-anchored mesoporous silica nanoparticles for efficient photodynamic therapy in hypoxic cancer. *J Am Chem Soc* 2017; 139: 10992–10995.
234. Li M, Huo L, Zeng J, et al. Surface engineered iron oxide nanozyme for synergistic chemodynamic/photodynamic

therapy with glutathione depletion and hypoxia relief. *Chem Eng J* 2022; 440: 135966.
235. Zheng D, Li B, Xu L, et al. Normalizing tumor microenvironment based on photosynthetic abiotic/biotic nanoparticles. *ACS Nano* 2018; 12: 6218–6227.
236. Lee C, Lim K, Kim SS, et al. Chlorella-gold nanorods hydrogels generating photosynthesis-derived oxygen and mild heat for the treatment of hypoxic breast cancer. *J Control Release* 2019; 294: 77–90.
237. Liu W-L, Liu T, Zou M-Z, et al. Aggressive Man-Made red blood cells for hypoxia-resistant photodynamic therapy. *Adv Mater Weinheim* 2018; 30: e1802006.
238. Wang Y, Huo J, Li S, et al. Self-rectifiable and hypoxia-assisted chemo-photodynamic nanoinhibitor for synergistic cancer therapy. *ACS Appl Mater Interfaces* 2022; 14: 10092–10101.
239. Szatrowski TP and Nathan CF. Production of large amounts of hydrogen peroxide by human tumor cells1. *Cancer Res* 1991; 51: 794–798.
240. Wilhelm S, Tavares AJ, Dai Q, et al. Analysis of nanoparticle delivery to tumours. *Nat Rev Mater* 2016; 1: 16014.
241. Jia X, Zhang Y, Zou Y, et al. Dual intratumoral redox/enzyme-responsive NO-releasing nanomedicine for the specific, high-efficacy, and low-toxic cancer therapy. *Adv Mater* 2018; 30: e1704490.
242. Li S, Liu R, Jiang X, et al. Near-infrared light-triggered sulfur dioxide gas therapy of cancer. *ACS Nano* 2019; 13: 2103–2113.
243. Foster JC and Matson JB. Functionalization of methacrylate polymers with thiooximes: A robust postpolymerization modification reaction and a method for the preparation of H2S-releasing polymers. *Macromolecules* 2014; 47: 5089–5095.
244. Yang T, Jin Z, Wang Z, et al. Intratumoral high-payload delivery and acid-responsive release of H2 for efficient cancer therapy using the ammonia borane-loaded mesoporous silica nanomedicine. *Appl Mater Today* 2018; 11: 136–143.
245. Chaves-Ferreira M, Albuquerque IS, Matak-Vinkovic D, et al. Spontaneous CO release from Ru^{ii}(CO) 2-protein complexes in aqueous solution, cells, and mice. *Angew Chem Int Ed Engl* 2015; 127: 1188–1191.
246. Guo R, Tian Y, Wang Y, et al. Near-infrared laser-triggered nitric oxide nanogenerators for the reversal of multidrug resistance in cancer. *Adv Funct Mater* 2017; 27: 1606398.
247. Ridnour LA, Thomas DD, Donzelli S, et al. The biphasic nature of nitric oxide responses in tumor biology. *Antioxid Redox Signal* 2006; 8: 1329–1337. DOI: 10.1089/ars.2006.8.1329
248. Xu W, Liu LZ, Loizidou M, et al. The role of nitric oxide in cancer. *Cell Res* 2002; 12: 311–320.
249. Bogdan C. Nitric oxide and the immune response. *Nat Immunol* 2001; 2: 907–916.
250. Chachlaki K, Garthwaite J and Prevot V. The gentle art of saying NO: how nitric oxide gets things done in the hypothalamus. *Nat Rev Endocrinol* 2017; 13: 521–535.
251. Roberts DD, Isenberg JS, Ridnour LA, et al. Nitric oxide and its gatekeeper thrombospondin-1 in tumor angiogenesis. *Clin Cancer Res* 2007; 13: 795–798.
252. Kargozar S, Singh RK, Kim H-W, et al. "Hard" ceramics for "Soft" tissue engineering: Paradox or opportunity? *Acta Biomater* 2020; 115: 1–28.
253. Zhao S, Li L, Wang H, et al. Wound dressings composed of copper-doped borate bioactive glass microfibers stimulate angiogenesis and heal full-thickness skin defects in a rodent model. *Biomaterials* 2015; 53: 379–391.
254. Lv F, Wang J, Xu P, et al. A conducive bioceramic/polymer composite biomaterial for diabetic wound healing. *Acta Biomater* 2017; 60: 128–143.
255. Martinelli V, Bosi S, Peña B, et al. 3D carbon-nanotube-based composites for cardiac tissue engineering. *ACS Appl Biol Mater* 2018; 1: 1530–1537.
256. Park J, Kim YS, Ryu S, et al. Graphene potentiates the myocardial repair efficacy of mesenchymal stem cells by stimulating the expression of angiogenic growth factors and gap junction protein. *Adv Funct Mater* 2015; 25: 2590–2600.
257. Lin Y, Brown RF, Jung SB, et al. Angiogenic effects of borate glass microfibers in a rodent model. *J Biomed Mater Res A* 2014; 102: 4491–4499.
258. Wang X, Gao L, Han Y, et al. Silicon-enhanced adipogenesis and angiogenesis for vascularized adipose tissue engineering. *Adv Sci* 2018; 5: 1800776.
259. Serra M, Hattinger CM, Pasello M, et al. Impact of ABC transporters in osteosarcoma and Ewing's sarcoma: which are involved in chemoresistance and which are not? *Cells* 2021; 10: 2461.
260. Girardi E, César-Razquin A, Lindinger S, et al. A widespread role for SLC transmembrane transporters in resistance to cytotoxic drugs. *Nat Chem Biol* 2020; 16: 469–478.
261. Keyvani-Ghamsari S, Khorsandi K and Gul A. Curcumin effect on cancer cells' multidrug resistance: an update. *Phytother Res* 2020; 34: 2534–2556.
262. Shang D, Wu J, Guo L, et al. Metformin increases sensitivity of osteosarcoma stem cells to cisplatin by inhibiting expression of PKM2. *Int J Oncol* 2017; 50: 1848–1856.
263. Chung M-F, Liu H-Y, Lin K-J, et al. A pH-responsive carrier system that generates NO bubbles to trigger drug release and reverse P-Glycoprotein-Mediated multidrug resistance. *Angew Chem Int Ed* 2015; 54: 9890–9893.
264. Wang X, Gong Q, Song C, et al. Berberine-photodynamic therapy sensitizes melanoma cells to cisplatin-induced apoptosis through ROS-mediated P38 MAPK pathways. *Toxicol Appl Pharmacol* 2021; 418: 115484.
265. Han X, Yang S, Mo H, et al. Targeting of CXCR1 on osteosarcoma circulating tumor cells and precise treatment via cisplatin nanodelivery. *Adv Funct Mater* 2019; 29: 1902246.
266. Song H, Ji Y, Zhu Y, et al. One-pot synthesized nanoheterostructure with dual-modal catalytic ROS generation ability for high-metastatic orthotopic osteosarcoma therapy. *Carbon N Y* 2023; 204: 196–210.
267. Chen Q, He Y, Wang Y, et al. Penetrable nanoplatform for "Cold" tumor immune microenvironment reeducation. *Adv Sci* 2020; 7: 2000411.
268. Feng B, Zhou F, Hou B, et al. Binary cooperative prodrug nanoparticles improve immunotherapy by synergistically modulating immune tumor microenvironment. *Adv Mater Weinheim* 2018; 30: e1803001.
269. Lu Y, Liu X, Hattori R, et al. Ultra-low impedance graphene microelectrodes with high optical transparency for simultaneous deep 2-photon imaging in transgenic mice. *Adv Funct Mater* 2018; 28: 1800002.
270. Chen Q, Xu L, Liang C, et al. Photothermal therapy with immune-adjuvant nanoparticles together with checkpoint

blockade for effective cancer immunotherapy. *Nat Commun* 2016; 7: 13193.
271. Zhu D, Chen H, Huang C, et al. H2O2 self-producing single-atom nanozyme hydrogels as light-controlled oxidative stress amplifier for enhanced synergistic therapy by transforming "Cold" tumors. *Adv Funct Mater* 2022; 32: 2110268.
272. Wang C, Xu L, Liang C, et al. Immunological responses triggered by photothermal therapy with carbon nanotubes in combination with Anti-CTLA-4 therapy to inhibit cancer metastasis. *Adv Mater Weinheim* 2014; 26: 8154–8162.
273. Hu XK, Rao SS, Tan YJ, et al. Fructose-coated angstrom silver inhibits osteosarcoma growth and metastasis via promoting ROS-dependent apoptosis through the alteration of glucose metabolism by inhibiting PDK. *Theranostics* 2020; 10: 7710–7729.
274. Li D, Zhang C, Tai X, et al. 1064 nm activatable semiconducting polymer-based nanoplatform for NIR-II fluorescence/NIR-II photoacoustic imaging guided photothermal therapy of orthotopic osteosarcoma. *Chem Eng J* 2022; 445: 136836.
275. Chen H, Wang GD, Tang W, et al. Gd-encapsulated carbonaceous dots with efficient renal clearance for magnetic resonance imaging. *Adv Mater Weinheim* 2014; 26: 6761–6766.
276. Zhang J, Ye Y, Chen Y, et al. Gd3N@C84(OH)x: a new egg-shaped metallofullerene magnetic resonance imaging contrast agent. *J Am Chem Soc* 2014; 136: 2630–2636.